Development of Solution-Processed Stable Silver Nanowire Networks for Transparent Electrodes

by

Woo Hyun Chae

B.S. and M.S. in Materials Science and Engineering
Northwestern University (2017)

Submitted to the Department of Materials Science and Engineering
in partial fulfillment of the requirements for the degree of

Doctor of Philosophy in Materials Science and Engineering

at the

MASSACHUSETTS INSTITUTE OF TECHNOLOGY

June 2022

Author .....
Department of Materials Science and Engineering
May 13, 2022

Certified by .....
Jeffrey C. Grossman
Professor of Materials Science and Engineering
Head of the Department of Materials Science and Engineering
Thesis Supervisor

Accepted by .....
Frances M. Ross
Chair, Departmental Committee on Graduate Studies

Development of Solution-Processed Stable Silver Nanowire Networks for Transparent Electrodes

by

Woo Hyun Chae

Submitted to the Department of Materials Science and Engineering
on May 13, 2022, in partial fulfillment of the
requirements for the degree of
Doctor of Philosophy in Materials Science and Engineering

Abstract

The continued use of indium tin oxide (ITO) as a transparent electrode for next generation optoelectronic devices will face severe challenges, including the scarcity of raw materials, high cost of processing, and lack of mechanical flexibility. Emerging transparent electrodes composed of solution-synthesized silver nanowire (AgNW) networks are highly appealing alternatives, but their poor stability prevents market adoption. Thus, there is a need to develop scalable and commercially viable processes for fabricating stable AgNW-based transparent electrodes.

This thesis seeks to overcome the failure modes of AgNWs by developing fully solution-based fabrication processes for nanocomposite transparent electrodes incorporating AgNWs and Graphene Oxide (GO) or Reduced Graphene Oxide (RGO). In particular, electrophoretic deposition and layer-by-layer deposition were actively explored as processing techniques to achieve AgNW networks protected by thin films of GO or RGO. A first process is developed to fabricate a transferrable AgNW network protected by GO on both sides, leading to exceptional chemical stability. A use case is demonstrated where the transparent electrode is integrated as a back-contact for a semitransparent organic solar cell, leading to a longer device lifetime. A second process is developed towards forming a conformal coating on AgNWs based on nanosized RGO, leading to enhanced all-around stability. A flexible transparent film heater was thus made, demonstrating its exceptional stability under harsh conditions.

It is expected that the processing knowledge and structure-property relationships uncovered in this work can be extended to the integration of other emerging low dimensional materials compatible with solution-based processing, and help bridge the gap between proof-of-concept demonstrations and industrial production of functional nanocomposite materials.

Thesis Supervisor: Jeffrey C. Grossman
Title: Professor of Materials Science and Engineering
Head of the Department of Materials Science and Engineering

Acknowledgments

One of the most important lessons I have learned throughout my time as a graduate student is that one should never take anything for granted. This applies to scientific research but also life in general. No one gets to a certain point in their life solely due to their efforts. One's life is hugely dependent on chance and generous support from others. While the former is difficult to fathom, the latter is apparent and deserves proper appreciation. Therefore, I would like to dedicate this page to acknowledge some of the generosity shown to me, which has been indispensable in completing this thesis.

First and foremost, I would like to thank my advisor, Prof. Jeffrey C. Grossman, for his mentorship. He has been an invaluable help in formulating the core scientific problems, guiding me through the problem-solving process, and teaching me to communicate the core scientific learnings effectively. In addition, by serving as a teaching assistant for his *Introduction to Solid State Chemistry* class, I learned what it means to convey and explain science at the most fundamental level. This experience taught me the importance of thinking in a first-principles oriented mode.

Secondly, I would like to thank my thesis committee, including Prof. Juejun Hu and Prof. Rafael Jaramillo, for their valuable time and advice in improving this thesis. Meetings with them have always resulted in constructive ways to improve the quality of my work and motivated me to examine my results from different perspectives. I have no doubt that this greatly added to the objectivity of this thesis.

Thirdly, I would like to thank all past and present members of the Grossman Group. A special thanks to Dr. Thomas Sannicolo, Jatin Patil, Adam Trebach, Ki-Jana Carter, and Ava Waitz, who were deeply involved in my research projects, and whose help were necessary for completing many key aspects of my thesis. I thank all the members of the Grossman group I met during my time at MIT for all the insightful discussions and for the fun we had at the foosball table. My heart goes out to: Laura von Bosau, Dr. Nicola Ferralis, Prof. Grace Han, Prof. Anthony Straub, Dr. Brendan Smith, Dr. Yun Liu, Dr. Owen Morris, Prof. Yanming Wang, Prof.

David Bergsman, Prof. Beza Getachew, Prof. Cuiying Jian, Dr. Stephen Frayne, Prof. Xining Zang, Dr. Arthur France-Lanord, Dr. Zhengmao Lu, Dr. Taishan Zhu, Dr. Tian Xie, Dr. Tae Won Nam, Dr. Dillon Yost, Cedric Viry, Xiang Zhang, Emily Crabb, Asmita Jana, Sheng Gong, among many others.

Last but not least, this work would have never even begun if it were not for the sacrifice and support of my family. I wish to thank my parents for their unconditional love and support. They are the foundation of who I am today. Finally, I wish to express my deepest gratitude to my wife Dr. EunAe Lee, for her unwavering support, resilience, and patience. Thank you for always being by my side.

Contents

List of Figures

List of Tables

Chapter 1

Introduction

1.1 Overview of Transparent Electrodes (TE)

Modern consumer products such as smartphones, tablets, laptops, smart TVs as well as various flexible thin film solar modules, to name a few, all utilize a layer that is transparent to visible light yet electrically conductive. The need of such device layer stems from the dual requirements that: (1) it should act as an efficient carrier collector with minimal electrical resistance that closes the device circuit and (2) light within the visible range should be either emitted from (power-to-light conversion) or enter into (light-to-power conversion) the underlying device layers (Figure 1-1). These layers are called Transparent Electrodes (TE), or Transparent Conductive Films (TCF) and are critical components of various electronic and optoelectronic devices such as solar cells, light emitting devices, touch screens, and transparent heaters.

In order to quantify and compare the performances of different TE, Figures of Merit (FoM) relevant to TE materials have been introduced. The dual requirement of having high optical transmittance and conductivity for TE led to an early definition of the FoM given in 1972 by Fraser and Cook [1] to be simply the ratio of the transmittance to the sheet resistance T/R_{sh}. Here, T is the transmittance at the wavelength of 550 nm and R_{sh} is the sheet resistance in Ω/sq, respectively. However, this simple definition of the FoM under-emphasizes transmittance. For example, based on this definition, the highest FoM for a given film conductivity results in

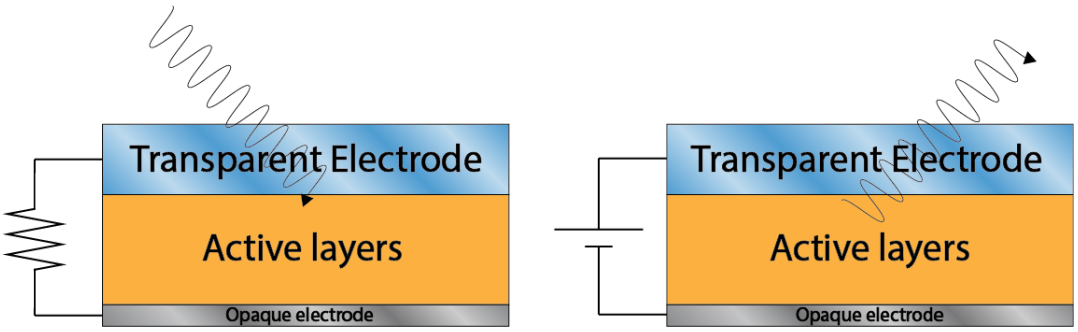

Figure 1-1: Schematic showing generic functions of a transparent electrode in opto-electronic devices in the case of (left) light-to-power conversion and (right) power-to-light conversion. The thickness of each layer are not to scale

only a 37% transmittance, which is undesirable for most practical applications. To address this issue, a modified FoM with exponent of ten for the transmittance term was introduced in 1976 by Haacke [2]. The following classical definition of the FoM by Haacke remains the most commonly used today by TE researchers.

$$FoM = \frac{T^{10}}{R_{sh}} \tag{1.1}$$

Later, a more fundamental definition of FoM was introduced and used by researchers by rearranging the following relation derived from optical considerations. [3]

$$T = \left(1 + \frac{188.5}{R_{sh}} \frac{\sigma_{OP}}{\sigma_{DC}}\right)^{-2} \tag{1.2}$$

Here, σ_{OP} and σ_{DC} are optical and DC conductivity, respectively. FoM can then be defined as the DC-to-Optical conductivity ratio σ_{DC}/σ_{OP} since high values of the conductivity ratio will lead to thin films with high T and low R_{sh}. It should be noted that defining FoM this way is best suited for bulk-like thin films where the DC conductivity is invariant with material thickness. However, deviation from bulk-like behavior has been observed for very thin (or highly transparent) TE materials based on percolating nanostructures such as metal nanowires (MNW), Carbon Nanotubes (CNT) and Graphene. [4] Developing definitions of the FoM that are materials or application-specific is still an area of ongoing research. [5]

1.1.1 Properties of Indium Tin Oxide (ITO)

Currently, the most widely used and commercially successful material for TE is a thin film of sputtered Indium Tin Oxide (Sn-doped In_2O_3 , ITO), due to its superior optical transmittance (90% at 550 nm) and low sheet resistance (<20 Ω/sq). [6] ITO is one of the materials among the class of Transparent Conductive Oxides (TCO). As wide band gap metal oxides with band gaps > 3 eV, TCOs are transparent to visible light. At the same time, they exhibit high electrical conductivity since they are degenerately doped by a secondary metal, which leads to high carrier concentration corresponding to a Fermi level well inside the conduction band (for n-type TCO such as ITO). [7] (Figure 1-2a)

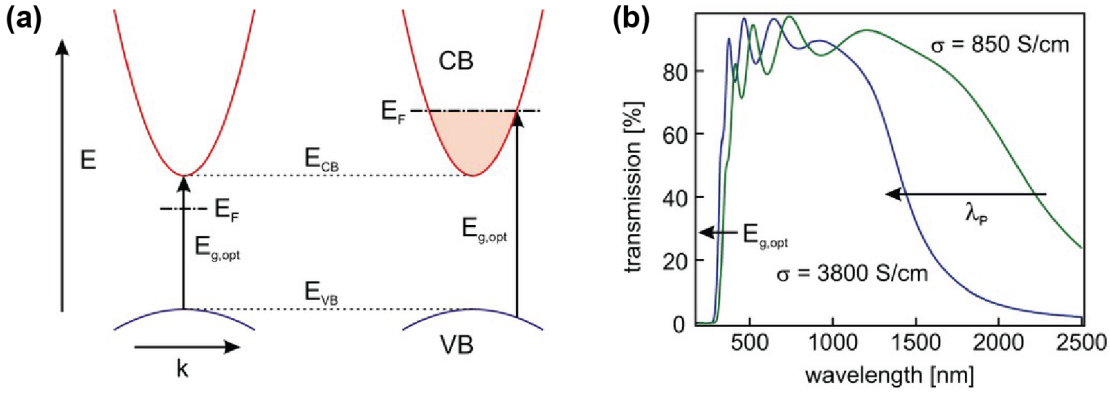

Figure 1-2: (a) Band structure illustration for undoped and n-type doped TCO (b) UV-vis transmission spectra of ITO with different conductivities. Reproduced from Ref [7] with permission.

The electronic behavior within ITO can be modeled as that of a dilute metal which leads to their optical properties near short and long wavelengths. For films with nearly free electrons, all light with frequency (wavelength) below (longer) than the plasma frequency (wavelength) is reflected. The plasma frequency ω_p is given by

$$\omega_p = \left(\frac{nq^2}{\epsilon_0 m_e}\right)^{1/2} \tag{1.3}$$

Here, n is the carrier density, q is the elementary charge, ϵ_0 is the vacuum permittivity, and m_e is the effective mass of electrons. For example in metals, the plasma

energy $\hbar\omega_p$ is around 5 eV, so they reflect all light below this energy which results in their typical visibly reflective surface. In ITO, with electron concentrations 1-2 orders of magnitude lower than typical metals, $\hbar\omega_p$ is around 1 eV in the case of high doping, but the actual reflection edge depends on the doping level. Hence, ITO does not transmit light in the infrared (IR) regime. This effect is clearly illustrated in Figure 1-2b, where increasing doping level (and hence conductivity) in ITO caused reduction in the plasma wavelength λ_p and caused more reflection in the near IR region. Near short wavelengths, degenerate doping causes blueshift in the absorption edge. (Figure 1-2b) This is due to the effective increase in the optical gap (defined as the lowest electronic transition accessible by absorption of a single photon) due to the high density of electrons in the conduction band. (Figure 1-2a) This effect is known as the *Burstein-Moss shift*, and is more apparent for degenerately doped ITO with a high conductivity. In intermediate visible wavelengths, neither absorption nor reflection occurs, making ITO visibly transparent.

1.1.2 Limitations of Indium Tin Oxide (ITO)

As discussed previously, ITO currently represents the industry standard material for TE applications. However, there are several limitations which inspired researchers to search for alternatives. First, ITO is intrinsically brittle due to its ceramic nature, and undergoes irreversible crack formation upon repeated bending cycles. [8] This is apparent in Figure 1-3 which shows that the ITO thin film resistance increases rapidly upon few tens of bending cycles while that of silver nanowire (AgNW) networks remains largely unchanged. [9,10] The mechanical brittleness of ITO and other TCOs in general calls for more flexible TE materials in order to be used in emerging flexible devices.

The second limitation associated with the continued use of ITO is the cost. This includes both the cost of thin film fabrication as well as the cost of the raw material, indium. The fabrication of ITO relies on a range of sputtering techniques that require high vacuum levels, and adds significant overhead to device fabrication processes that can otherwise be carried out by all solution-based processes. These include processes

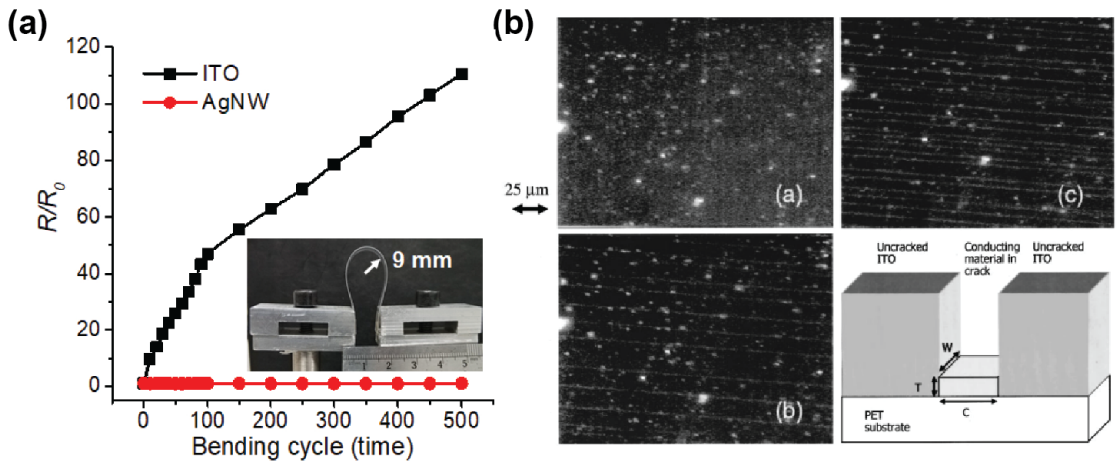

Figure 1-3: (a) Comparison of ITO and AgNW under tensile loading cycles where samples are bent up to a radius of curvature of 9 mm, and returned to the initial position, reproduced from Ref [9] with permission. (b) Optical micrographs of 105 nm sample of ITO coated PET at a-2%, b-2.5%, and c-3% strain, and a schematic diagram showing bridging material at the PET substrate which results in an increasing but finite resistance with increasing strain, reproduced from Ref [8] with permission.

to fabricate fully printable organic and perovskite based solar cells, for instance. [11–13] In addition, raw indium is not only subject to severe price fluctuations but also faces a sustainability crisis. Indium has been designated as one of the 'endangered elements' by the American Chemical Society. [14] This is largely because indium is only produced in a handful of countries, and is a small byproduct of Zinc, itself a critical element. This fact coupled with continuously rising demand for LCD, touch screens, and solar cell devices make continued ITO use unsustainable in the long run.

Yet another limitation of ITO as a TE material, although one that receives less attention than the others, is its reflectivity towards near-IR light. As mentioned in the previous section, increasing the doping level to enhance the conductivity of ITO leads to a decreasing plasmon wavelength, which leads to reflection of light in the near IR and IR regions. In applications that requires harnessing near-IR light such as transaprent PV [15], the use of ITO could therefore severely limit device efficiency.

1.1.3 Emerging materials to substitute ITO

As mentioned, the use of ITO will be faced by numerous challenges in the coming years due to the shortage of raw materials such as indium, incompatibility with large-scale manufacturing methods, and its inability to be used in a multitude of flexible devices. Over the past decade, there have been continual efforts to develop alternatives to ITO by utilizing metallic nanowire (MNW) networks or carbon nanomaterials including carbon nanotubes (CNT), graphene, and reduced graphene oxide (RGO). Various studies have identified each materials' innate advantages and disadvantages.

Carbon nanomaterials including CNT and graphene have recently received attention as TE materials due to their good electrical mobility and conductivity, high transparency, chemical inertness and mechanical robustness. Although CNT films are inexpensive and can be fabricated over large areas, their performance lags behind that of ITO due to the challenging purification process and high junction resistances between nanotubes. For instance, to achieve a sheet resistance as low as 10 Ω/sq, the thickness of the CNT film must be higher than 100 nm, which severely limits its transparency. [16] Also, the sheet resistance of CVD-graphene is thickness dependent and generally high (from 300 Ω/sq to $>$1000 Ω/sq) due to grain boundaries. Additionally, the difficulty in processing large-area high quality graphene remains a challenging issue. [17]

Metal nanowires (MNW) such as silver nanowires (AgNW) and copper nanowires (CuNW) are promising for next-generation transparent electrodes because of their ease of synthesis, and compatibility with scalable coating methods. Even the earliest reports on MNW TE have shown that their performances rival that of ITO, with sheet resistances as low as 16 Ω/sq at a transparency of 86%. [18] The random network of MNWs conduct by the wires acting as an electrical percolation network, while the empty spaces between wires allow light to transmit through ensuring good transparency across a wide frequency range. Some of the major challenges of MNWs include their lack of long-term stability, surface roughness and optical haze that could be detrimental to some device applications.

1.2 Silver nanowire (AgNW) networks: Promise and Challenges

Despite significant efforts to develop alternatives to ITO, it is difficult for a single class of materials to simultaneously meet the requirements for an ideal TE, including high transparency (>90%), low resistance (<10 Ω/sq), flexibility, stretchability, prolonged stability, and ability to be fabricated by non-vacuum, low temperature process. Therefore, it is of technological interest to design and fabricate hybrid transparent electrodes incorporating two or more types of materials to highlight advantages of each while complementing each materials' shortcomings. In this regard, AgNWs are especially attractive as a main conductive component of hybrid transparent electrodes because they already possess a clear advantage over other types of materials in terms of conductivity, transparency, and flexibility. The most significant factor preventing widespread application of AgNW as TE is its lack of stability. Therefore, combining AgNW with other nanomaterials in different ways to overcome the stability issue is an intriguing avenue of research. In this section, the main features of transparent AgNW networks are discussed, such as their synthesis, electrical/optical properties. Their failure modes leading to their poor stability will be discussed in depth in Chapter 2.

1.2.1 Synthesis of AgNW networks

The solution synthesis protocol and mechanism of various MNWs, including silver, copper, and gold nanowires are well-reported in the literature. Silver nanowires (AgNW) are the most heavily studied and widely applied. The advantage of AgNW over other types of MNW originates from the exceptional attributes of bulk silver which has the highest conductivity at room temperature, as well as the ease and reproducibility of AgNW synthesis.

The synthesis route of AgNW first developed by Younan Xia's group [20, 21], employing $AgNO_3$ ion reduction by ethylene glycol (EG), is the most widely used method among others. Known as 'polyol synthesis', this method presents a simple route of

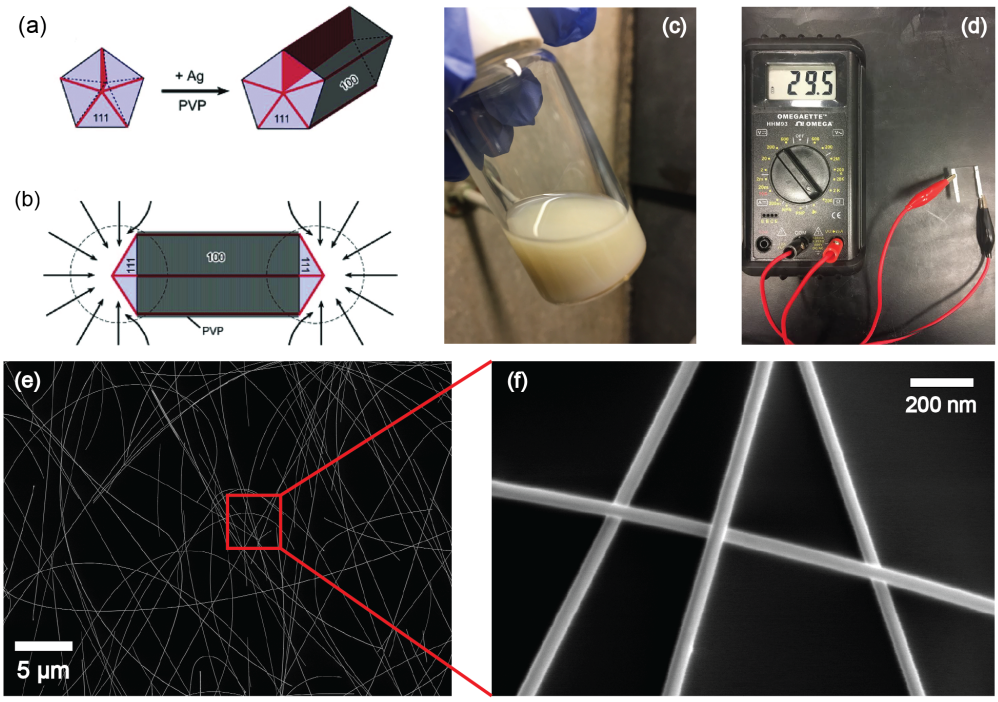

Figure 1-4: (a, b) Schematic illustration of the growth of AgNWs with pentagonal cross sections [19] (c) Synthesized AgNW dispersion in isopropanol (d) Multimeter reading showing the resistance of AgNW network coated on glass (e) low-mag and (f) high-mag SEM image of AgNW networks.

synthesis where EG (polyol) reduces the Ag precursor ($AgNO_3$) in the presence of a capping agent (polyvinylpyrrolidone, PVP). It has been proposed through subsequent studies that AgNW synthesis is composed of three different steps, nucleation, evolution of nuclei into seeds, and anisotropic growth into nanowires. Initially, $AgNO_3$ solution in EG is slowly added dropwise to another EG solution containing PVP, while the entire solution is being heated. The controlled reaction leads to the formation of thermodynamically stable multiply twinned Ag seeds (Figure1-4a), which serves an important role in subsequent growth of the wires. Thus, the process is a self-seeding process. [21] The multiply twinned Ag nanoparticles are the result of surface energy minimization, [22] and are terminated by {111} facets. At the same time, {111} facets are adjoined together by twin boundaries, which become active sites for attracting Ag ions to diffuse from the solution to the nanoparticles. Due to Ag atom attachment to {111} facets, side surfaces of {100} facets form, which is subsequently passivated by

PVP molecules' preferential attachment to the {100} facets rather than to the {111} facet. [23] This process results in initial nanorod formation by uniaxial elongation of the initial multiply twinned nanoparticles.

After the formation of pentagonal Ag nanorods, it can readily grow into a long nanowire by the dual role of PVP molecules to enable anisotropic growth by tight passivation of the {100} side surface and capping of the wires to prevent their aggregation. This mechanism is illustrated in Figure 1-4b. High aspect ratio AgNW have been synthesized on the basis of polyol synthesis, achieving wire lengths of over 300 μm with diameters less than 150 nm. [24]

After the synthesis of AgNWs, the resulting solids can be purified by repeated centrifugation steps and be diluted in isopropyl alcohol (IPA) or methanol. (Figure 1-4c) This AgNW solution is the basis for further fabrication into AgNW networks. AgNW networks where the AgNWs randomly dispersed on the substrate are easily obtainable through solution-phase deposition techniques including drop casting [25, 26], spin coating [27], blade coating [28], rod coating [29], and spray coating [30, 31]. (Figure 1-4d) These methods can be carried out under low temperature and non-vacuum conditions. However, drop casting results in a characteristic 'coffee stain' which leads to inhomogeneity in the final film. Spin coating is limited in scale, tends to result in edge effects and forms radially non-uniform films due to the centrifugal force. Spray coating is by far more scalable and produces homogeneous and reproducible AgNW networks, assuming that the nanowire solution concentration is well-optimized and possible ultrasonic nozzle clogging issues can be avoided. [32]

1.2.2 Electrical and optical properties of AgNW networks

The electrical and optical properties of AgNW network-based TE are closely related to the properties of individual nanowires. In general, as the diameter D_{NW} of the MNW is reduced to length scales comparable with the mean free path Λ (34 nm for bulk Ag [33]) of electrons in the bulk material, the resistivity is expected to increase due to surface scattering as shown by Bid et al. [33] This behavior was experimentally demonstrated and described by the following equation:

$$\rho_{NW}^{Ag} = \rho_{bulk}^{Ag}\left(1 + \frac{\Lambda}{2D_{NW}}\right) \tag{1.4}$$

where ρ_{NW}^{Ag} is the resistivity of AgNW, and ρ_{bulk}^{Ag} is the resistivity of bulk Ag. In practice, the diameter of the AgNWs used for TE ranges between 50 nm to 100 nm, and the resistivity of such AgNWs is around $\rho = 2.78 \sim 2.92$ $\mu\Omega$-cm at room temperature. [33] Compared to the resistivity of bulk Ag at room temperature ($\rho =$ 1.6 $\mu\Omega$-cm), the increase in resistivity due to narrowing of the wires is small enough such that they can still be used as highly conductive TE.

It should be noted that the overall electrical conductivity of the MNW network is dictated by the 1-dimensional percolating nature of nanowires that form a kind of 'electronic highway', as can be seen in Figure 1-4e and f. Thus, the areal density of AgNWs, defined as areal mass density (*amd*) or areal number density, is a critical factor that governs the sheet resistance of the entire film as networks with more wires per given area have more percolating pathways. Empirically, the sheet resistance R_{sh} can be expressed as the following:

$$R_{sh} \propto (n - n_c)^{-t} \tag{1.5}$$

where n_c is the critical areal density of AgNWs, below which conduction does not occur, and t is the percolation exponent. Figure 1-5a illustrates this relationship between AgNW *amd* and network resistance. In addition to the density of AgNWs, when considering the macroscopic electrical properties of AgNW networks, the resistance between nanowires (junction resistance) plays a critical role since it can be orders of magnitude larger than the intrinsic resistance of a single AgNW. As deposited AgNW networks often have high and non-optimized resistance because of poor electrical contact between nanowires, caused by a less intimate physical distance between wires or due to the presence of PVP capping layers which inhibit efficient charge transport across wires. Various strategies to overcome this have been implemented, including thermal annealing [34], chemical treatment [35], and light-induced nanowelding [36], among many others. The general principle of such post-treatment is based on caus-

ing sintering to occur between nanowires to create an intimate inter-wire electrical contact. A well-optimized post-treatment results in excellent sheet resistance on the order of ∼10 Ω/sq with transmittance over 90% (Figure 1-5b).

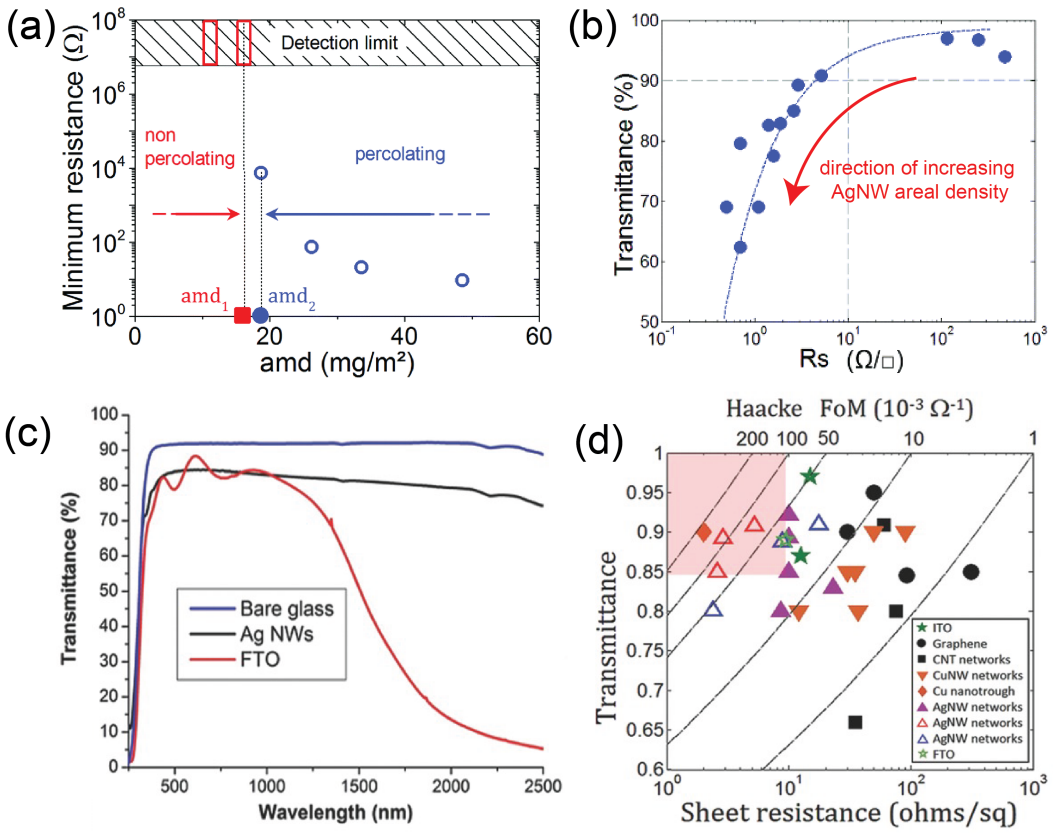

Figure 1-5: (a) Minimum resistances of AgNW (diameter 117 nm) networks obtained by thermal annealing plotted against areal mass density, where the critical density n_c of AgNWs lie between the first percolating (blue) sample and the last non-percolating (red) sample (b) Transmittance values at 550 nm versus sheet resistance for the same annealed AgNW networks where each point corresponds to different network densities [27] (c) Transmittance spectra for AgNW, FTO, and bare glass substrate (b) Transmittance versus sheet resistance for various TE, along with iso-FoM lines [37]

The optical properties of AgNW networks are apparent from their transmission spectra, which shows distinctive differences from that of TCOs. Since the transparency of AgNW networks originate from their large areal fraction of empty spaces, they have an enlarged wavelength range for which the transmittance is high. For instance, Figure 1-5c shows the transmittance spectra of a typical AgNW network and that of FTO. In the near infrared (NIR) range, the transmittance of FTO starts to

fall off, due to reasons explained in Section 1.1.1. In contrast, AgNW networks retain their high transmittance even in the NIR range. This is a competitive advantage of MNW based TE over TCO based TEs for certain applications such as transparent PVs. [15]

There is a trade-off relationship between sheet resistance of a AgNW network and its optical transmission with increasing or decreasing network density. (Figure 1-5b) As the density of a network increases, the sheet resistance decreases, converging to the bulk thin film limit, while the optical transmission decreases because of increased shading from the AgNWs. This inverse relationship between effective film thickness and film transparency generally holds across all materials used for TE applications. Therefore, the more a TE can overcome this trade-off, the higher the FoM value will be, corresponding to a movement to the upper-left corner in the map shown in Figure 1-5d. It is clearly seen here that the best AgNW networks (points corresponding to Ag117 and Ag138) demonstrate a FoM on par or better than ITO or other emerging materials.

1.3 Thesis Overview

This thesis focuses on developing new scalable solution-based processes to overcome the critical failure modes of AgNW-based TE, with an emphasis on utilizing Graphene Oxide (GO) and Reduced Graphene Oxide (RGO). The thesis is arranged as follows:

In Chapter 2, I summarize the critical failure modes of MNWs, previously reported strategies to stabilize MNWs, and motivate the use of GO and RGO as a protective coating material for AgNW networks. Perspective is given on how to frame the requirements of MNW-encapsulant hybrids with reference to their target applications, namely: solar cells, transparent film heaters, sensors, and displays.

In Chapter 3, I demonstrate a scalable and economically viable process using electrophoretic deposition (EPD) to fabricate long-term stable hybrid transparent conductive films with a sandwich-like structure, where a conductive AgNW mesh is covered by GO films on both sides. One side is protected by a EPD-assembled

GO while the other side is covered by a ultrathin GO layer coated by solution dip treatment. The film was applied to the top electrode of a semitransparent organic solar cell with longer storage life relative to unprotected devices.

In Chapter 4, I developed an innovative process to conformally encapsulate silver nanowire (AgNW)-based transparent conductive films with nanosized GO followed by chemical reduction. This resulted in a significant improvement of all-round stability, including thermal, electrothermal, chemical, and mechanical stability. This was accomplished all while avoiding the expensive vacuum-based coating process typically required to achieve a similar level of stability, which opens up possibilities for scalable and continuous Roll-to-Roll manufacturing. Thus fabricated TE was successfully demonstrated as a transparent film heater.

In Chapter 5, I summarize of the important scientific results and contributions from the work and include future perspectives.

Chapter 2

Failure Modes of Metal Nanowire Networks (MNW) and Mitigation Strategies

This chapter is reproduced in part with permission from ref. [38]

J. J. Patil*, **W. H. Chae***, A. Trebach, K. Carter, E. Lee, T. Sannicolo, and J. C. Grossman. Failing Forward: Stability of Transparent Electrodes Based on Metal Nanowire Networks. *Advanced Materials*, **33**(5), 2004356 (2021) *Equal Contribution

As discussed in Chapter 1, AgNW-based TE offers favorable characteristics over ITO. However, the most significant factor that prevents widespread use of AgNW-based TE is its instability. It should be noted that these instabilities are not unique to AgNWs, but to any MNW, albeit with varying degrees depending on composition. Hence, in this chapter, we discuss the most critical failure modes experienced by MNWs and current approaches to stabilize them.

2.1 Failure modes of AgNW networks

Despite the favorable performance of AgNW-based TE, the poor stability of MNW networks including AgNWs is a significant barrier that prevents their widespread

adoption. The instability of MNWs in general can be attributed to multiple degradation mechanisms that occur during normal operation or storage. Such mechanisms can be chemically, thermally, electro-thermally or mechanically activated, which dominate to varying degrees depending on the application. For instance, thermally activated degradation can often be neglected when integrating MNW networks into photovoltaics and displays, while it must be considered in TFHs (transparent film heaters), as will be discussed below. On the other hand, chemical aging is likely to happen regardless of the target application.

2.1.1 Chemically induced failure

The chemical stability of an AgNW network is represented by its capacity to maintain its initial conductivity over an extended period in various environments, without undergoing chemical changes that reduce conductivity. Even in atmospheric conditions, AgNWs are expected to lose conductivity in the long term as a result of some chemical instability. This is due to the huge impact of atmospheric corrosion on the AgNW owing to its high surface-to-volume ratio.

Unlike many metals, dry Ag does not form a significant surface oxide. Ag_2O is stable only in a region of high pH and in the presence of strong oxidizers. [39, 40] Instead, it is agreed among experimental and theoretical studies that the most abundant product of atmospheric corrosion of Ag is Ag_2S, also known as acanthite, a semiconductor with a monoclinic crystal structure. [41–43] Many studies suggest that sulfidation occurs by reaction of Ag with hydrogen sulfide (H_2S) in the atmosphere. [43] Despite the low concentrations of these gases in air, on the order of parts per billion, the presence of water, O_2 and NO_2 can accelerate the reaction process. The following reactions have been proposed by multiple studies [40–42]

$$2Ag + H_2S \rightarrow Ag_2S + H_2 \tag{2.1}$$

$$2Ag + H_2S + \frac{1}{2}O_2 \rightarrow Ag_2S + H_2O \tag{2.2}$$

$$2Ag + H_2S + 2NO_2 \rightarrow Ag_2S + 2HNO_2 \tag{2.3}$$

when H_2S is not abundant, atmospheric carbonyl sulfide (OCS) gas can also become the source of AgNW sulfidation by the following reaction. [41, 43, 44]

$$OCS + H_2O \rightarrow H_2S + CO_2 \tag{2.4}$$

Rather than forming a conformal film, Ag_2S has been observed to grow as discontinuous nodules or nanoparticle-like features on the surfaces of both bulk Ag and AgNWs (Figure 2-1a-d). In the case of AgNWs, it was reported that the formation of Ag_2S nanoparticles cause the nanowires to become discontinuous after 6 months.[32] Nevertheless, such degradation rates are sensitive to experimental conditions, such as humidity and temperature, and the initial defect concentration of the synthesized AgNW that serve as nucleation sites of sulfide particles. This makes it difficult to compare between different degradation studies. Regardless of such discrepancies, there is no question that the sulfidation of AgNW is a serious problem, particularly for TFHs with relatively high operating temperatures. [42, 44, 45]

Another route for the chemical degradation of AgNWs is dissolution by Ag oxidation. Ag has poor oxidation stability in acidic conditions, as indicated by its Pourbaix diagram. [39] This leads to implications for the long-term chemical stability for AgNWs in applications involving AgNWs interfaced with materials and device layers that are acidic in character. For instance, AgNW was observed to degrade when in contact with acidic and hygroscopic poly(3,4-ethylenedioxythiophene) polystyrene sulfonate (PEDOT:PSS), a widely used conductive polymer charge transport layer in organic PV devices. [46–48] Chen et al. [47] showed that AgNW networks coated with as-received PEDOT:PSS ("PH1000" from Heraeus) on and stored in ambient conditions for 108 h, underwent a 30% increase in sheet resistance (R_{sh}) as opposed to a 19% increase for bare AgNW networks.

2.1.2 Thermally and Electro-thermally induced failure

In general, thermal and electrical stresses, or the combined effects thereof (henceforth termed electrothermal stresses) cause atomic surface diffusion, which leads to mor-

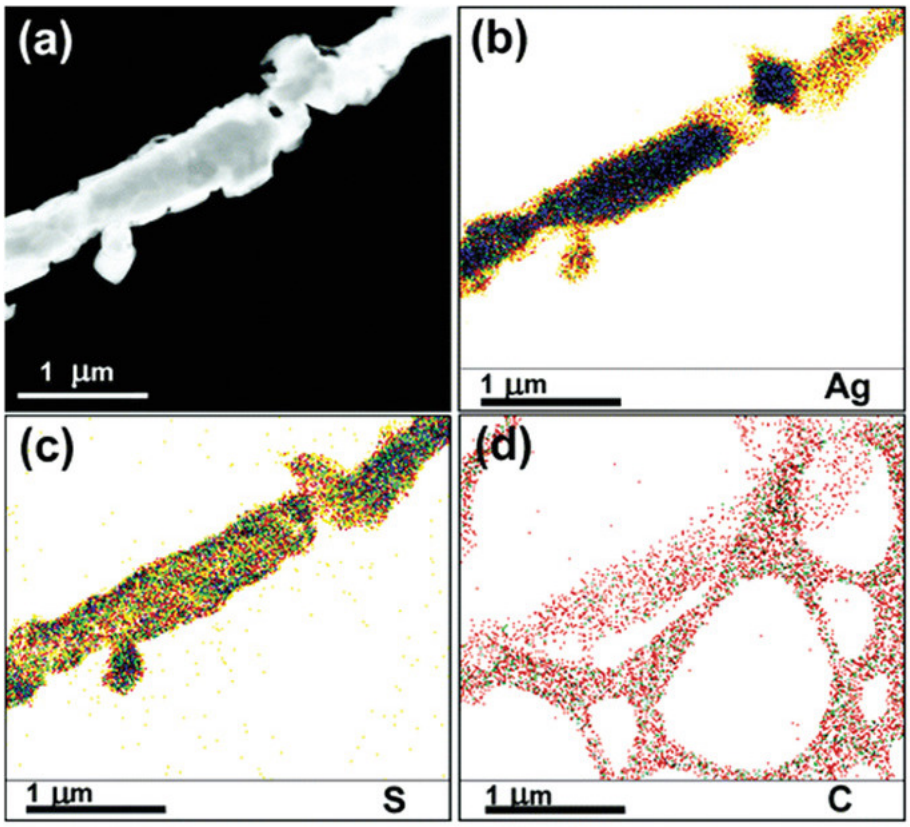

Figure 2-1: (a) TEM image of a sulfidized AgNW. b–d) TEM–EDS (energy-dispersive X-ray spectroscopy) mapping of the sulfidized AgNW presented in (a): (b) silver map, (c) sulfur map, (d) carbon map. [41]

phological evolution of the MNWs. This phenomenon causes the MNWs to form voids and disconnect—which results in current no longer passing through them. This can cause current to be redirected to nearby MNWs, which contributes to network-scale failure of multiple nanowires. We define the *thermal stability* as the MNW network's ability to withstand high temperatures applied from external sources, and distinguish it from *electrothermal stability*, which is primarily due to Joule-heating from current flow.

Under high temperature, nanowires undergo spheroidization through a process known as Plateau-Rayleigh instability. This instability is caused by the minimization of surface energy of a cylinder to a set of disconnected spheres, which is due to the lower surface-to-volume ratio of spheres compared to a cylinder (length L, radius R_0) with $L > \frac{9}{2}R_0$. In the presence of thermal fluctuations, surface diffusion can

create surface perturbations on the wire segments that can be modelled as a sine function. (Figure 2-2a) It can be shown that for a cylinder with initial radius R_0 and a sinusoidal perturbation $R = R_{cyl}(t) + \epsilon(t)cos(2\pi z/\lambda)$, where $R_{cyl}(t)$ is the average cylinder radius, $\epsilon(t)$ is the time-dependent perturbation amplitude, λ is the wavelength of the perturbation, and z is the length along cylinder axis, perturbations with a critical wavelength $\lambda_{crit} = 2\pi R_0$ will increase spontaneously in amplitude until spheroidization (Figure Figure 2-2a). When this morphology evolution is governed by atomic surface diffusion, as is the case for MNWs, perturbation with wavelength of $\lambda_{max} = \sqrt{2}\lambda_{crit}$ will grow the fastest, and the cylindrical wire will eventually break into spheres with an average spacing λ_{max}. [49,50] The kinetics that govern the rate at which the above morphology evolution proceeds is best described by curvature-driven surface diffusion. That is, the growth rate of the perturbation is expressed as the following:

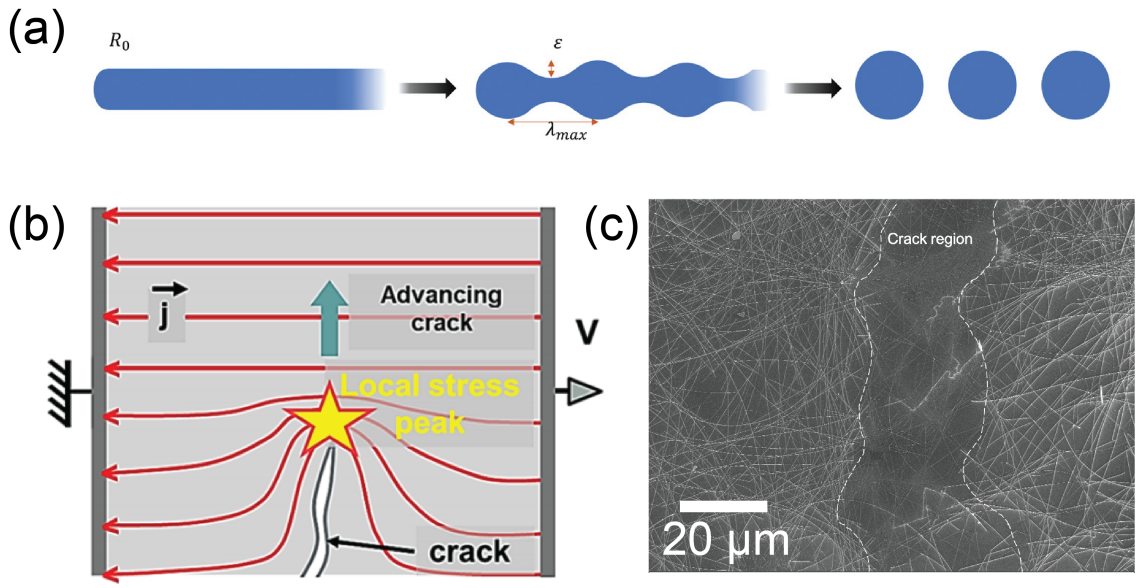

Figure 2-2: a) Schematic of the progression of spheroidization of a long cylinder. Perturbations with a wavelength of approximately λ_{max} tend to evolve fastest and cause the formation of spheres, indicating failure of the nanowire. [38] (b) Schematic representation of the mechanisms involved in the crack propagation by electrothermal failure [51] (c) SEM image showing the contrast between electrothermally-induced crack region and intact region in a AgNW network

$$\frac{\partial \epsilon}{\partial t} = \frac{\gamma \Omega^2 D_s c_s}{k_B T} \left(\frac{\partial^2 \kappa}{\partial s^2} \right) \tag{2.5}$$

where κ is the curvature as a function of position s on the cylinder surface, D_s is the diffusivity at the surface, and γ is the surface energy, Ω is the atomic volume, c_s is the concentration of surface sites, and k_B is the Boltzmann constant. [50] The surface diffusion is rapid at high temperatures, so spheroidization of the MNWs occurs around 300∼400℃ depending on heating conditions and initial NW diameter, well below its bulk melting temperature (961℃). Once the MNW has spheroidized, the resistance of the network drastically increases by several orders of magnitude. This failure at high temperature is critical for conductivity optimization of the MNW network by annealing, [27] and also for applications regarding transparent heaters as the continuously operable lifetime and maximum achievable temperature will be severely limited by the aforementioned instability. [52]

The *electrothermal* modes of failure are fundamentally governed by the same surface-diffusion dominated morphology evolution found in pure *thermal* instability. However, the difference is that the source of the thermal energy is the power dissipated by the MNW network itself. Therefore, a unique failure behavior can be observed on the network scale. For instance, one of the failure mechanisms observed during electrical tests (such as a constant linear voltage ramp), is called "thermal crack propagation," which is attributed to the localization of current density at a specific defect in the sample—typically a region with a lower mass density of MNWs. This variation in the network induces a higher local current density and localized "hot spot," which causes localized failure. The "hot spot" is observed moving across the sample, perpendicular to current flow, resulting in a divergence of the resistance of the network, as illustrated by Figure 2-2b. [51] The region of localized failure as shown in Figure 2-2c contains evidence of partial or full spheroidization, chemical corrosion, or a combination of both.

2.1.3 Mechanically induced failure

Mechanical failure in MNWs is particularly important to consider at a microscopic level to understand the benefits and limitations of large-scale networks. MNW networks are indeed typically chosen for their excellent stability in flexible and stretchable devices. [36, 37, 53] Their stability can be attributed to the fact that nanowires in a network are uniformly dispersed and randomly aligned, and thus the mechanical forces at play would be scaled by a factor of the cosine of the MNW angle relative to the strain direction. The strain is defined as a change of length of a surface (ΔL) relative to the initial length of the surface (L_0). For bending tests, the strain is defined as the ΔL of a surface assuming surface compressive strain on the inside of the bending radius, and surface tensile strain on the outside of the bending. For bending tests, the role of the substrate is important in considering the application and durability of the wires on the surface, as described in the following equation. The strain ε of a surface of a device—thus the strain experienced by the nanowires—during flexing of the device, can be written as a function of the substrate thickness t_s, film thickness t_f, radius of curvature of substrate R_c [54]

$$\varepsilon = \frac{\Delta L}{L_0} = \frac{t_s + t_f}{2R_c} \simeq \frac{t_s}{2R_c} \tag{2.6}$$

In bending tests, thicker substrates induce higher strains on each surface, which makes failure onset earlier, or at higher radii of curvature (with the assumption of strong adhesion between the nanowire and substrate). Figure 2-3 (left) shows the change in electrical resistance of AgNW networks and ITO films on poly(ethylene terephthalate) (PET) substrates of various thicknesses, after bending tests, [54] showing that thicker substrates and smaller radii of curvature cause earlier onset of failure. Figure 2-3 (right) shows the trends relating substrate thickness to ultimate failure strain, with data for ITO and AgNW networks with different diameters, showing that thicker substrates cause AgNW networks to mechanically fail at lower strains. The mechanics of individual nanowires, however, are quite nuanced.

Though films with MNWs show little variation in sheet resistance over many bend-

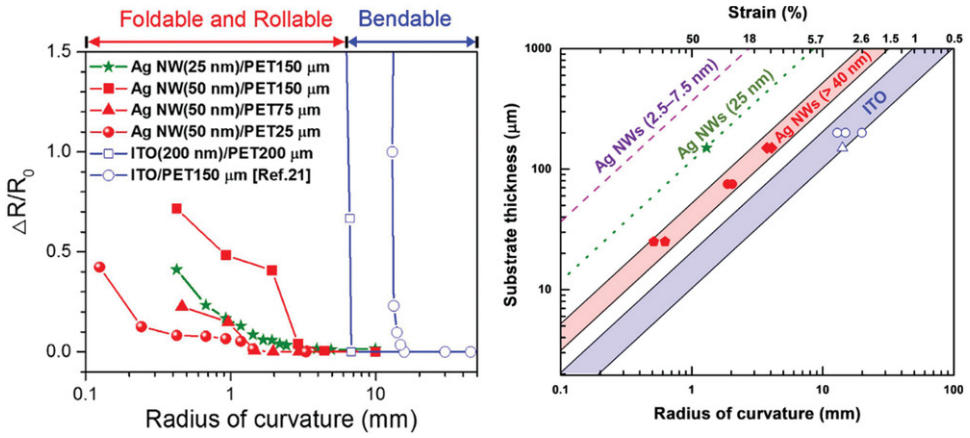

Figure 2-3: Sheet resistance change of AgNW networks on PET as a function of radius of curvature, for different thicknesses of PET and AgNW diameters, compared with ITO electrodes on PET (left). Plot representing theoretical substrate thickness versus strain/radius of curvature to failure, showing a higher hardness for lower average AgNW diameters (right). [54]

ing cycles, individual nanowires are shown to undergo brittle failure. This behavior can naively be explained by dislocation starvation—an effect where the lack of dislocations in nanoscale, crystalline materials reduces the ductility of the material (which is seen in single-crystal nanowires). However, since MNWs typically exhibit twinning, dislocations have been shown to form and subsequently be influenced by twin boundaries. For example, an increase in AgNW ductility is observed as a function of decreasing AgNW length and diameter, as shown in Figure 2-3 (right). [55, 56]

Nanowires of sizes larger than 40 nm show evidence of dislocation starvation, and thus brittle failure. However, at smaller diameters, surface nucleated dislocations arise and their motion is slowed by the twin boundaries, [55] which enables strain hardening (i.e., dislocation motion proportional to the deformation induced in the wire), which enables plastic deformation. At larger diameters, due to a lower ratio of twin boundary area to surface area, surface dislocations formed are less likely to encounter the twin boundaries, which causes dislocation pile-up and thus, brittle fracture. [57] This behavior is also observed at junctions, where the high curvature of a nanowire encasing the junction causes cracking and failure. [58] A study by Wu et al. showed that twinned MNWs had a lower ratio of plastic to elastic displacement than annealed wires in a bending test (which were shown to form single-crystal

nanowires in an inert atmosphere)—which suggests that even with a diameter of 23.2 nm, nanowires undergo failure that is closer to brittle than ductile. [59] When these wires are encapsulated, the mechanical properties of the encapsulant start to influence the failure of the nanowires, where thicker coatings result in higher network resistances after 300,000 bending cycles. [60] However, the fracture mechanism remains the same—owing to the brittleness of the oxide coatings.

2.2 Strategies to Delay MNW failure

The most straightforward strategy to address the instabilities in MNW networks is to encapsulate the vulnerable MNW networks with a material that is: (i) resilient against chemical degradation, (ii) impermeable to species that contribute to degradation, and (iii) conformally coated on MNWs to delay failure mechanisms that rely on surface atomic diffusion. With this aim, a variety of materials and processes for MNW encapsulation that are compatible with both AgNW and CuNW have been proposed. Strategies to protect and elongate the useful lifetime of AgNWs can largely be classified according to the processes used to deposit barrier materials. These processes can be largely be classified into (1) Vapor deposition-based and (2) Solution-based.

2.2.1 Vapor deposition based approaches

First, large-area graphene synthesized by chemical vapor deposition (CVD) has been widely investigated as an encapsulating layer, inspired by the near impermeable nature of a perfect graphene lattice. A combination of MNW devices with CVD-grown polycrystalline graphene have been demonstrated, [61–63] fabricated by transferring CVD grown graphene onto a silver nanowire mesh. Ye et al [61] transferred CVD-graphene onto AgNW networks and showed that the sheet resistance was nearly invariant over the course of 2 months in ambient air at room temperature, while that of bare AgNWs increased by 80%. A similar encapsulation by CVD-graphene on AgNWs was performed by Lee et al [62] where the sheet resistance change was less than 15% after 8 days in 70 °C/70% RH. Ahn et al. [63] directly deposited

graphene on CuNWs to form core–shell graphene/CuNW films by employing low-temperature plasma-enhanced CVD (LT-PECVD). While the sheet resistance of bare CuNW networks increased by 1800 times within two days in ambient conditions, that of the core–shell graphene/CuNW films increased only slightly, less than 9%, after 30 days. These observations were attributed to the excellent gas barrier properties of graphene, [44, 64] as well as the enhanced conductivity by electrical co-percolation between CuNW network and graphene grains. [65] It should be noted, however, that the synthesis of large-area graphene with low defect concentration is still difficult and is an active research topic of its own. Thus, while there are clear merits as cited above, the deployment of graphene as an encapsulating material is costly at this time.

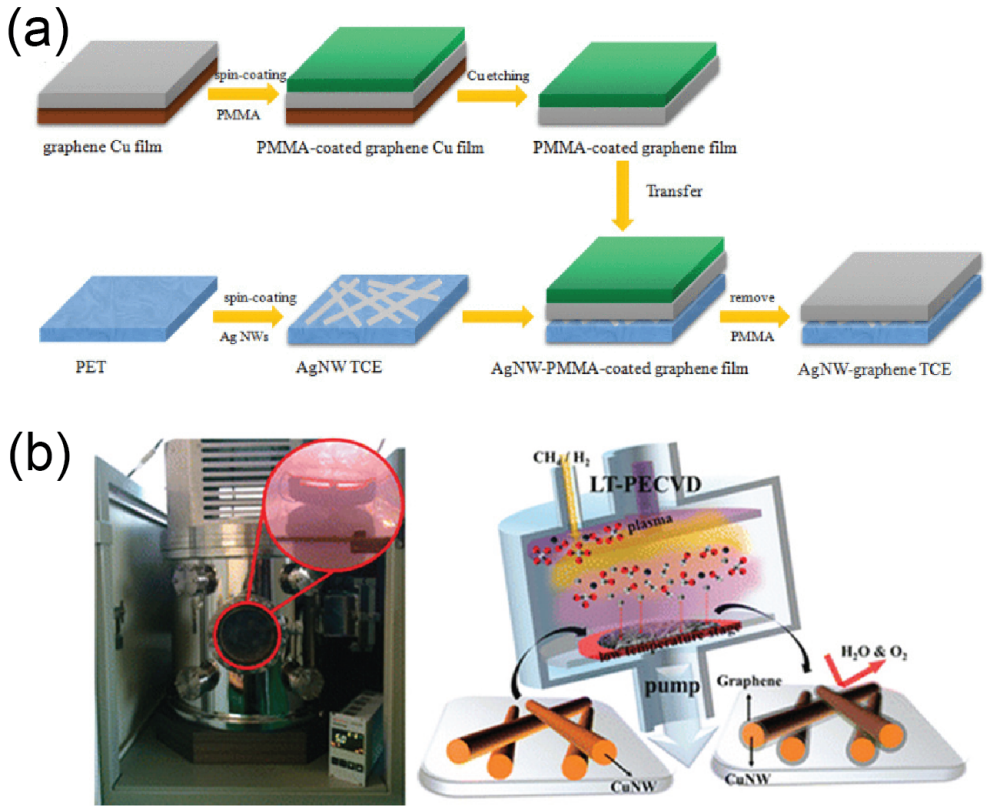

Figure 2-4: (a) Schematic of the fabrication process of the AgNW–graphene TE on a glass substrate involving transfer of CVD grown-graphene. [66] (b) Direct deposition of graphene by LT-PECVD on CuNWs. [63]

Secondly, conformal oxide coatings on MNW networks fabricated by various vapor-based deposition techniques were shown, although most studies have so far focused

on improving their thermal and electrical stabilities. For instance, embedding AgNW in sputtered ZnO layers [67] to achieve a sandwiched ZnO/AgNW/ZnO structure, or forming a thin conformal coating of ZnO using spatial atomic layer deposition (sALD), significantly improves their stability at high temperatures [68] and is expected to serve as a barrier against corrosion. ALD of oxides such as ZnO, TiO_2, [69] Al_2O_3, [70] Al:ZnO, [71] and HfO_2 [60] have been demonstrated as transparent and, in some cases, conductive, encapsulating layers; an example of a conformal ZnO coating on AgNWs is shown in Figure 16, where the electrothermal stability of the nanowires increases with increasing ZnO thickness. These coatings raise the electrical, thermal, and chemical resilience of the nanowires with minimal impact on the optical properties. For heating applications, these networks can reach temperatures upwards of 350°C, which is around 100°C higher than acceptable bare MNW processing temperatures. [68] In all cases, low-temperature depositions are favored, to avoid spheroidization as well as to ensure process compatibility with flexible substrates. Moreover, roll-to-roll processes are desirable. In the case of sputtering, pilot-scale roll-to-roll setups are already available, enabled by linear magnetrons. [72] sALD is also able to achieve high deposition rates, work in roll-to-roll compatible processes, and operate in an open air setup. [73] Thus, for high value or high performance applications, scalable vapor phase deposition of coatings on MNWs will be crucial for their commercial viability.

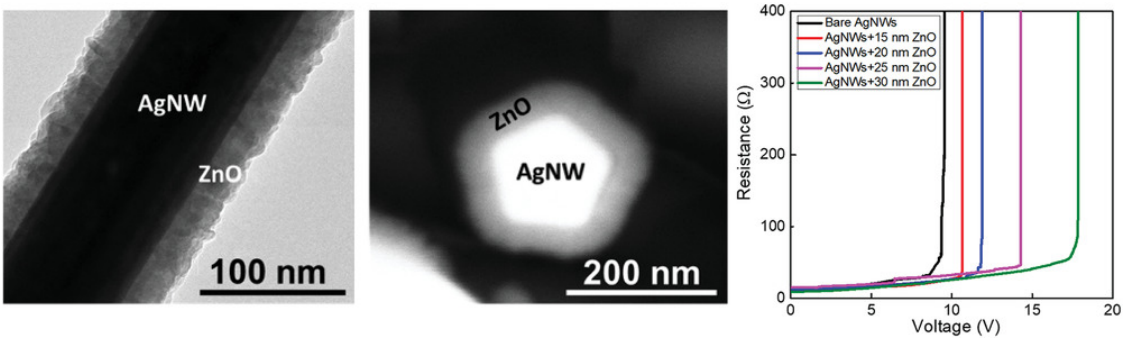

Figure 2-5: TEM (left) and SEM (middle) images of sALD-deposited ZnO coating on AgNW. Right: AgNW network resistance under a linear voltage ramp, showing a delayed failure voltage as a function of coating thickness. [68]

2.2.2 Solution deposition based approaches

Embedding MNWs into a polymer matrix has been explored for flexible electronics applications. This strategy is particularly effective in delaying mechanical failure of MNWs, while preserving their electrical properties. [74, 75] This enables stretchable devices, while also providing gas and moisture barrier properties which delays chemical failure. These advantages are substrate and application specific, since they require the implementation and compatibility of device components with the polymer environment and precursors—and if polymer processing is done separately, then they need suitable transferability and interfacing with the appropriate device layers. [76] Alternatively, conductive polymer coatings were employed to create MNW-based nanocomposites. Most notably, PEDOT:PSS was used in multiple studies due to its conductive nature and compatibility with many organic optoelectronic devices, especially as hole transport layers in organic photovoltaics (OPV). [77] However, the possibility that PEDOT:PSS is accelerating the corrosion of MNWs has not been fully ruled out due to its acidic nature. [47, 48]

Electrochemistry and wet-chemistry based methods to coat MNWs have also been developed. One approach pioneered by Wiley et al. [78] uses electrodeposition to directly coat the MNWs with oxide forming metals, such as Zn and Sn (Figure 2-6a,b). Electrodeposition at cathodic potentials preferentially coats the MNWs with a thin ($\approx$15 nm) shell of Zn or Sn resulting in minimal loss in optical transmittance. Optical transmittance can be further improved by oxidizing the Zn/Sn with a H_2O_2 treatment (Figure 2-6c). This conformal oxide coating dramatically improved the stability of CuNW networks under high humidity conditions (Figure 2-6d). [78] Electroless deposition of Ni on CuNW was also demonstrated by the same group and has shown applicability towards organic solar cells. [80] More recently, Stucky et al. [79] implemented a simple wet-chemistry process to coat AgNWs with a monolayer of SnO_2. By introducing Sn^{2+} precursors to an AgNW suspension in ethanol, a spontaneous redox reaction takes place on the AgNWs, forming a SnO_2 layer (Figure 2-6e–g). The SnO_2-capped AgNWs demonstrated thermal resilience and chemical stability. The

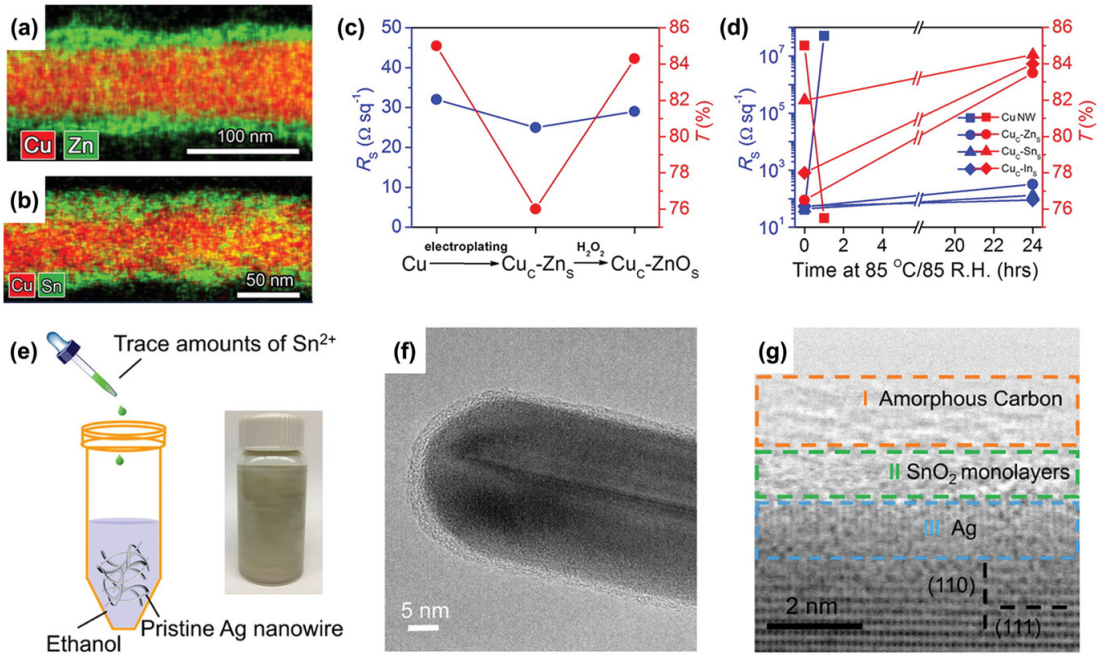

Figure 2-6: (a,b) EDS mapping images of Zn-coated (a) and Sn-coated (b) CuNWs by electrodeposition. (c) Sheet resistance and transmittance evolution of Zn-coated CuNWs upon H_2O_2 treatment. (d) Evolution of sheet resistance and transmittance of encapsulated CuNWs stored at 85°C/85% RH. (a–d) Reproduced with permission. [78] (e) Schematic of wet chemistry-based Sn^{2+} treatment of AgNWs. (f,g) TEM image (f) and bright-field HRTEM image (g) of SnO_2 coated AgNW. (e–g) Reproduced with permission. [79]

authors reported only a 27% increase in sheet resistance after a harsh O_3/O_2 exposure at 150°C for 60 min and the absence of spheroidization even at high temperatures of 300°C in air. The above approaches show significant potential given the simplicity and cost-effectiveness of solution-based processes.

As an alternative to CVD-graphene, inexpensive and solution-processible Graphene Oxide (GO) or Reduced Graphene Oxide (RGO) have been explored as encapsulants to improve the underlying MNWs' stability. GO can be readily obtained by the well-known *Hummers method*, where raw graphite is treated with sodium nitrate ($NaNO_3$), potassium permanganate ($KMnO_4$), and concentrated sulfuric acid (H_2SO_4) to form graphite oxide before hydrolyzing in water to form nearly single-carbon-thick GO. [81] The layers of GO derives from graphite, but are heavily decorated with oxygen functional groups on the edges and on the plane. Lerf et al [82] have proposed that the

carboxylic (-COOH) groups are predominant at the edge, while hydroxyl (-OH) and epoxide (-O-) are more dominant at the plane. (Figure 2-7) Due to the abundant carboxylic acid groups which ionize in solution, GO acquires negative charge in aqueous solution and can be stabilized as a colloidal solution which aids in processing. However, unlike graphene, GO is an insulator, since its sp^2 network is disrupted by sp^3 carbons due to various functional groups. To partially restore conductivity, GO can be reduced to RGO by thermal and chemical means. [83, 84]

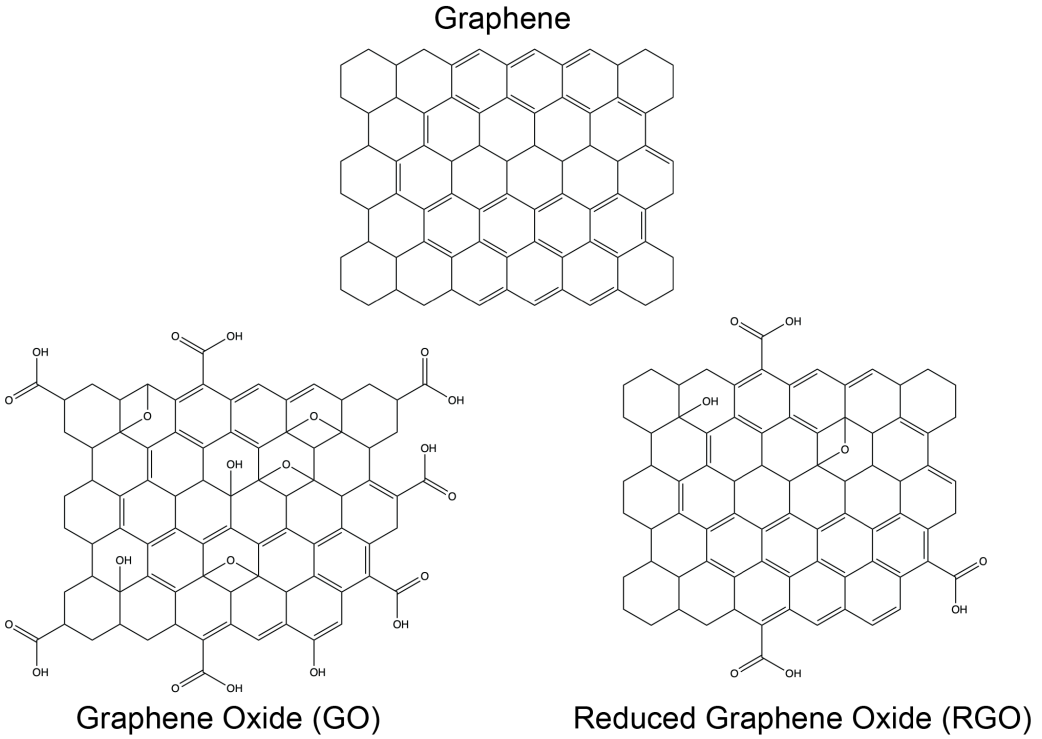

Figure 2-7: Idealized structure of Graphene, Graphene Oxide (GO) and Reduced Graphene Oxide (RGO)

A number of studies have demonstrated the incorporation of GO and RGO to MNW-based transparent electrodes. Thus far, GO/AgNW, [85–89] RGO/AgNW, [46, 90, 91] RGO/CuNW [92, 93] have all been synthesized using various solution-processing techniques including, but not limited to, spin-coating, [90] dip-treatment, [85, 93] layer-by-layer (LbL) coating, [89] rod-coating, [94] and spray-coating. [86, 91, 92] It is interesting to note that both conductive RGO and insulating GO have been used with MNW networks to fabricate TE, with significant improvement of

conductivity over bare MNW networks. [85–87,91] The additional layer over the MNW network decreases the optical transmittance compared to a bare MNW network, but more so for RGO at the same layer thickness due to RGO's higher optical absorption. [95] However, minor reductions in transparency could be justified by the improved stability, which is one of the most pressing challenges in using MNW networks. For instance, GO/AgNW films fabricated by interfacial self-assembly [87] exhibited no noticeable change in sheet resistance after 28 days of storage in air, while that of bare AgNW networks increased by 900%. Other studies [86, 88] have directly proven the chemical resilience of GO/AgNW films against sulfidation by exposing the samples to various chemicals, including H_2S. Studies using GO and RGO as encapsulating layers invariably show that the chemical stability of MNW improves by minimizing their exposure to solvents and corroding species from the atmosphere. This largely stems from the well-known gas barrier properties of GO and RGO. [96]

2.3 Assessment of Protective Coatings for AgNW networks

Given the diverse protective coating materials and processes used for MNW networks as reviewed in the previous section, it is important to qualitatively and (at least) semi-quantitatively assess their respective merits to guide materials selection for useful applications. The main goal of materials selection is to meet specific product performance goals. In this regard, it is crucial to examine existing MNW stabilization strategies in the context of existing applications and their specific performance/lifetime benchmarks.

2.3.1 Application-Specific Requirements for MNW-based TE

We first identify the success criteria for each application where the use of MNW networks were considered as either the active components or as electrical contacts. The portfolio of such device applications is diverse but can be summarized into four

broad categories: transparent film heaters (TFH), solar cells, displays, and sensors. For each group of applications, we consider the relative importance of the performance and stability criteria, including: (i) the figure of merit (FoM), (ii) (low) optical haze, (iii) chemical stability, (iv) (electro)thermal stability, and (v) mechanical stability.

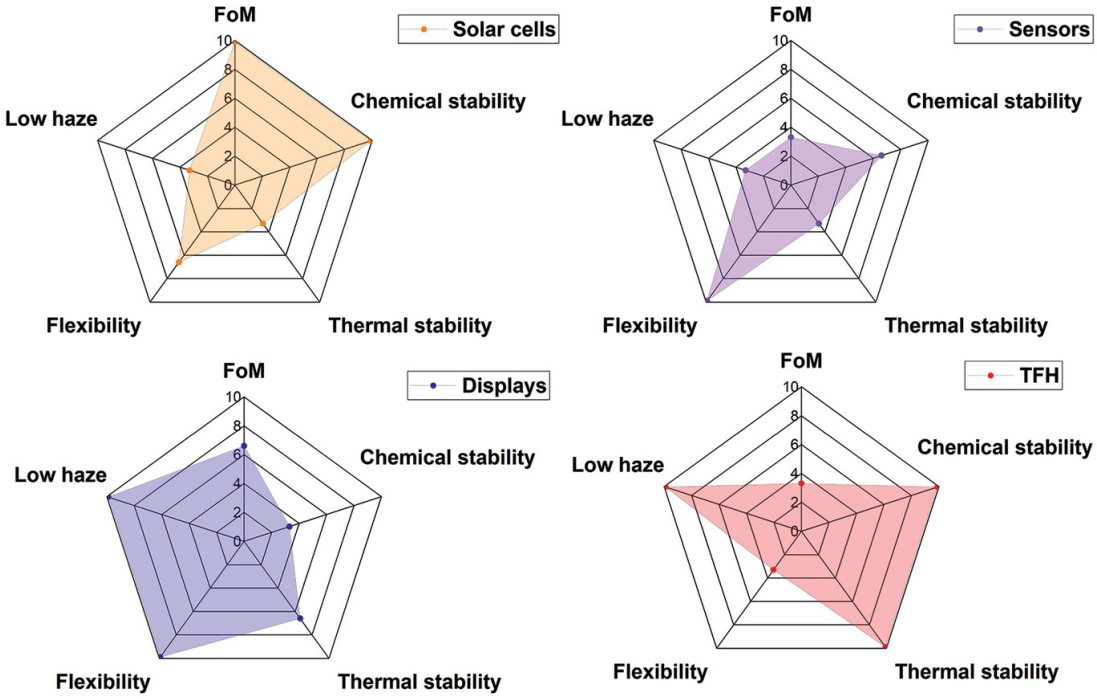

Figure 2-8: Radar plots showing the relative importance of performance metrics for TFHs, solar cells, displays, and sensors. The marks are only general qualitative indications, where a higher score denotes a favorable quantity.

The radar plots in Figure 2-8 indicate the relative importance of each criteria, based on each application's working environment and purpose. For instance, TFHs are commonly used in defrosting or defogging vehicle windows or any surface of a device exposed to the outdoor environment. TFHs operate by raising the temperature of a transparent conductor through Joule heating. Naturally for TFHs, electrical and thermal stabilities of MNWs are the most important criteria. Chemical stability is also important as high temperature induces irreversible chemical degradation of the MNWs.

Although electrothermal stability is important for solar cells, it is less critical than the electrothermal requirements for TFHs. This comparison can be quantified by the

average operating current density flowing through individual nanowires (J_{NW}). According to Khaligh et al. for solar cells operated in standard conditions, J_{NW} is on the order of 10^8 A/m^2, [97] which is around two orders of magnitude lower than the value reported by Lagrange et al. for unprotected AgNWs in TFHs when approaching failure conditions, i.e., $J_{NW,(failure)} \approx 10^{10}$ A/m^2. [69] The calculations for J_{NW} associated with solar cell and TFH with varying parameters (such as MNW density, MNW dimensions, applied voltage, etc.) have been included in the Supporting Information. On average, in standard operating conditions, the J_{NW} for solar cells is around one order of magnitude lower than the J_{NW} for TFHs. As a consequence, for solar cells, relative importance should rather be placed on the FoM, which is critical to attaining an acceptable power conversion efficiency (PCE). It should be noted that for such optoelectronic devices, the stability of MNW networks should be considered according to the specific architecture of the device. For instance, studies have shown that MNW networks can be either laminated as top electrodes, [76] or pre-deposited on a flexible substrate, [98] which illustrate that their stability is highly dependent on surrounding layers. For instance, long-term chemical stability against the environment and acidic PEDOT:PSS is important when utilizing MNW networks as top electrodes for inverted organic solar cells to ensure prolonged device lifetime. The performance/stability requirements are similar for displays, except that the optical haze should be minimized so as to not impair visibility. In the case of solar cells, increasing the optical haze could be beneficial; by introducing scattering which maximizes incident light absorption, higher short-circuit current density values can be achieved. [99] However, haze is detrimental when considering transparent/semi-transparent solar cells, for similar reasons as TFHs and displays. Finally, the most critical requirement for (often wearable) sensors comprising MNW networks is having excellent mechanical stability including and flexibility and stretchability.

2.3.2 Evaluation of MNW Encapsulation Strategies

As we have discussed earlier, TE based purely on MNW networks have poor stability, which results in limited applicability towards devices with rigorous performance

requirements. The addition of encapsulating materials will improve either chemical, mechanical, or thermal stabilities, or the combinations thereof, to varying degrees. These stability improvements typically come at the expense of processing cost or the FoM, which are all important metrics that gauge the practicality of a materials system. A comparison of different technologies, including ITO, bare MNW networks, and encapsulated MNW networks, is presented in Figure 2-9, where the cost is set based on a fixed sheet resistance requirement for all materials. We can see that all the encapsulation strategies improve the overall stability of the MNW network. In particular, GO and RGO offer a good improvement of all stability with a relatively low processing and materials cost (as will be discussed in the next section), while ALD-based approaches offer more pronounced stability improvements at a slightly higher cost. Though most existing literature focuses on encapsulation of AgNW networks, few works have also demonstrated stability improvements for CuNW-based electrodes. [100, 101]

As an example of how the gathered metrics can be used to evaluate the suitability of an encapsulation strategy for a specific application, we consider encapsulated MNW electrodes for solar cells in Figure 2-10. In this figure, the overlapping area between the application and the electrode technology shows how well the application needs are addressed. In this figure, we only consider technical performance parameters, and not cost considerations, as this will be discussed later in this section. Based on the initial radar plot, it is clear why ITO is more appealing than unencapsulated MNW networks due to its superior stability (assuming flexibility is not a major application requirement). For the GO and RGO encapsulated MNW networks, stabilities much closer to that of ITO can be achieved with the added benefit of mechanical flexibility, where ALD and sALD can offer stability closest to that of ITO while maintaining mechanical flexibility. For the solar cell application, this shows the promise of using encapsulated MNW-based electrodes for flexible solar applications. In all cases, application requirements are better met with encapsulated MNW networks than with ITO, but the specifics of which requirements are better met depends on the application. For example, since flexibility is particularly important for displays and sensors,

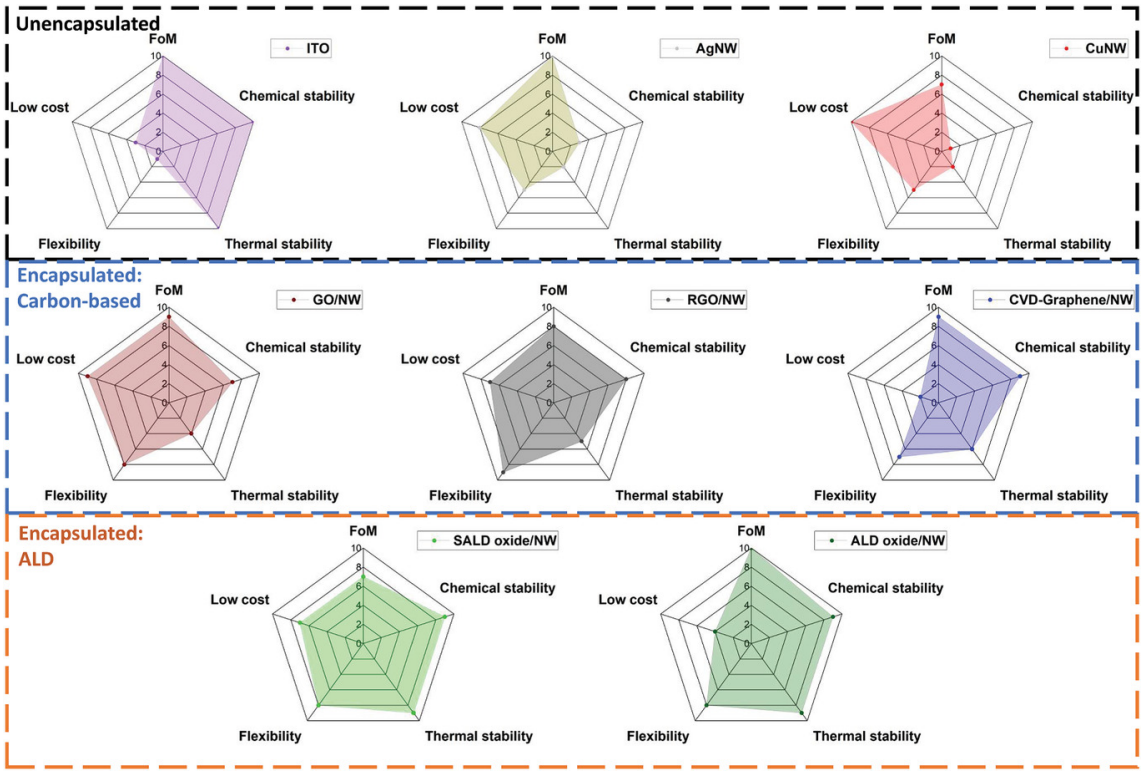

Figure 2-9: Radar plots showing comparison of various transparent electrode systems in terms of their Figure of Merit (FoM), low cost, chemical stability, thermal stability, and flexibility. The marks are only general qualitative indications, where a higher score denotes a favorable quantity. A detailed analysis to justify these marks, based on a survey of recent literature, is available in [38], or by direct request to the author.

this makes it much more appealing to use encapsulated MNW networks. The analysis with the rest of the applications is presented in available in [38].

Regardless, unequivocal comparison of the degree of stability across different systems of encapsulated MNW networks is not a trivial task. This is because failure tests are not standardized and are often not application-oriented. Elucidating the cost of materials synthesis for an encapsulant-MNW pair also requires detailed technoeconomic analysis.

2.4 Why (Reduced) Graphene Oxide?

From the technological assessment of strategies to protect MNWs as given in the previous section, it is clear that there is no one ideal type of coating material that can

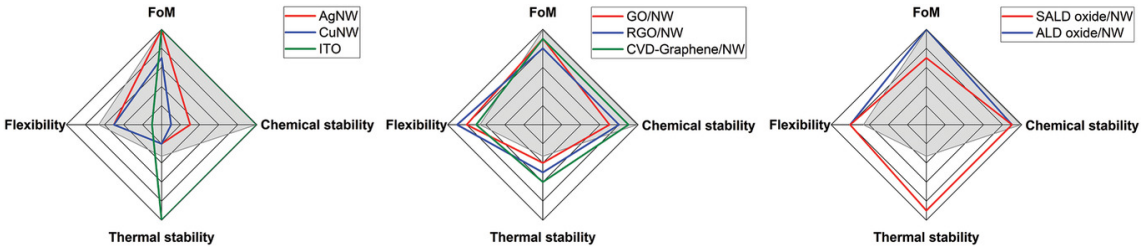

Figure 2-10: Radar plots comparing an application (in this case, solar cells) to TE technologies, namely ITO, MNW networks, and encapsulated MNW networks. The application requirements, starting from the top going clockwise, are the FoM, chemical stability, thermal stability, and flexibility. The gray area represents the application requirements, while the solid lines represent the TE technology. This illustrates how encapsulation makes encapsulated MNWs more appealing than ITO for flexible solar cell applications.

satisfy all of the requirements, including application-specific performance, cost, and long-term stability. Nevertheless, in moving towards a technological goal, it is important to put more importance on one of the requirements in order to constrain our search space to develop the best stabilizing solution for AgNW networks. In this thesis, cost effectiveness and scalability will be put forth as the most important requirements, given the fact that one of the primary motivations for using solution-processed MNWs in the first place is their low cost and ease of processing over conventional ITO. (Figure 2-9) As discussed earlier, GO/RGO are relatively cheap materials that still shows good barrier properties coupled with outstanding mechanical flexibility. Their synthesis route is now commoditized such that there are a multitude of vendors which produce them at large-scale, making them closer to actual market adoption in the near future. In this regard, the focus of this thesis was put on developing an all-solution process to stabilize AgNWs and further explore use of GO and RGO as a protective coating material.

However, there exist challenges in using GO or RGO with AgNW networks which the present thesis aims to tackle. First of which is the lack of truly scalable processes to fabricate GO/RGO-AgNW hybrid TEs.

Second, the thermal/electrothermal stability when using GO or RGO with AgNWs have seldom been discussed or have been measured to be quite poor compared to metal oxide based coatings. Earlier works by Khaligh et al. [102] and Kwan et

al. [103] cite thermal dissipation and surface diffusion hindrance, respectively, as possible mechanisms by which spheroidization of MNW can be prevented by a RGO/GO coating. Zhu et al. [104] used GO as intermediate layers between AgNW networks, assuming that GO could prevent diffusion, and showed its thermal stability. This recent progress demonstrates a growing interest in understanding the role that GO/RGO plays in the thermal and electrical stability of MNW networks, though existing hypotheses still need to be verified.

Finally, fundamental questions regarding the structure-property (-stability) relationships in GO/AgNW and RGO/AGNW TEs have not been fully answered. For instance, differences between the role of GO and RGO in enhancing the chemical stability of AgNW-based TE is less studied, although any observed differences are expected due to differences in both chemistry and structure between RGO and GO. In addition to its restored graphitic sp^2 domains, RGO has fewer functional groups at its edges and basal planes compared to GO, resulting in reduced hydrophilicity [83] and interlayer spacing. [105] This could be beneficial in protecting the underlying MNWs that are prone to moisture and oxidizing/sulfidizing species. However, it is also known that the reduction of GO results in the formation of defects, such as nanopores, through which such corroding species could be transported. [106] Other factors regarding the morphology of GO or RGO films, such as coverage and conformality over the AgNW network, film thickness, and individual flake sizes, could alter their barrier properties. The impact of these parameters on the AgNW stability remain not fully answered and a thorough and systematic study is needed.

Chapter 3

Double-Sided Encapsulation of AgNW Networks by GO

This chapter is reproduced in part with permission from refs. [45] and [107]:

W. H. Chae, T. Sannicolo, and J. C. Grossman. Double-Sided Graphene Oxide Encapsulated Silver Nanowire Transparent Electrode with Improved Chemical and Electrical Stability. *ACS Applied Materials and Interfaces*, **12**(15), 17909–17920 (2020)

T. Sannicolo, **W. H. Chae**, J. Mwaura, V. Bulović, and J. C. Grossman. Silver Nanowire Back Electrode Stabilized with Graphene Oxide Encapsulation for Inverted Semitransparent Organic Solar Cells with Longer Lifetime. *ACS Applied Energy Materials*, **4**(2), 1431–1441 (2021)

3.1 Introduction

As explained in Section 2.3, integration of MNWs with inexpensive and solution-processable graphene oxide (GO) or reduced graphene oxide (RGO) was previously explored by using spin coating, [90] dip coating, [87] rod coating, [108] and spray

coating, [86, 91, 92, 109] but challenges still remain in terms of large-scale processing. For example, spin coating is a lab-scale batch process that also results in inhomogeneous films due to edge effects and the centrifugal force on particles. Moreover, the size of the substrate is severely limited, as with vacuum filtration. Spray coating incurs a risk of spray nozzle clogging or unsteady operation, which may be a concern for nanomaterials with high aspect ratios. This may require hours of sonication to break up the GO sheets or necessitate use of ultrasonic sprays which tend to break or damage micrometer-sized GO sheets, [110, 111] placing restrictions on the morphology of the final GO film. In addition to such drawbacks, a critical limitation for all of the conventional solution-based deposition techniques is that the choice of substrate is restricted to those with a planar geometry, and pretreating them to optimize the wetting properties is critical to mitigate inhomogeneities such as "coffee stains". [112] Furthermore, although previous studies have demonstrated an AgNW-GO hybrid structure, many aspects of the chemical and electrical stability of AgNW networks imparted by the presence of GO either have not been fully demonstrated or remain poorly understood.

In this work, we report a novel fabrication process that utilizes a scalable and economically viable electrophoretic deposition (EPD) method and GO solution dip treatment to fabricate highly stable transparent electrodes where the conductive AgNW network is effectively "sandwiched" between a seamless EPD-GO film with tunable thickness and ultrathin GO (Dip-GO) composed of 1–2 layers. We demonstrate that the GO layers enhance contact between NWs to reduce the junction resistance, mitigating the need for treating NWs at high temperature. Our films demonstrated excellent sheet resistance as low as 15 Ω/sq and a tunable transmittance of 70–87% by simply tuning the EPD parameters.

Furthermore, the increase in the film stability was shown to depend largely on which GO layer is protecting the underlying AgNW network. When Dip-GO is exposed to air ("Dip-GO up"), stability reinforcement of the electrode is observed, although partial degradation can still occur. However, when EPD-GO was exposed to air ("EPD-GO up"), our hybrid electrode retains its original conductivity under

long-term storage at 80 °C in both moderate (55% relative humidity) and high (80% relative humidity) humidity conditions. The exceptional chemical stability offered by the EPD-GO layer was verified by the absence of major silver corrosion products for the AgNW as indicated by X-ray photoelectron spectroscopy (XPS). Finally, for the first time, an *in-situ* voltage ramping test up to 20 V was performed on a GO-AgNW composite structure. The results indicate a novel stabilization behavior enabled by the presence of GO that prevents abrupt divergence of the resistance to the MΩ range experienced by bare AgNW networks.

Importantly, our process allows the film to be transferred to arbitrary surfaces with desired orientation such that either EPD-GO or Dip-GO is facing up. This freedom adds versatility for future device integration where certain properties need to be emphasized over others as they are strongly correlated to the thickness/robustness of the GO protecting layer being used. For instance, a thick EPD-GO layer offering increased chemical and electrical stability at elevated temperatures and high voltages could be preferentially used at the top when integrating this film in a transparent heater, while an ultrathin Dip-GO layer could be preferentially used as an interfacial layer in solar cells as a way to enable Ohmic transport and optimize the energy level matching with other layers.

3.2 Overview of the fabrication process

We have developed a novel and cost-effective fabrication process utilizing electrophoretic deposition (EPD) and solution dip-treatment to create an EPD-GO/AgNW/GO hybrid composite transparent conductor. The process is illustrated in Figure 3-1a: (i) coating of a dissolvable sacrificial cellulose acetate (CA) layer on stainless steel (SS) substrate, (ii) EPD of GO thin film, (iii) AgNW coating, (iv) dip treatment in GO solution, (v) acetone bath to dissolve CA layer, and (vi) transfer onto arbitrary surface.

EPD is a colloidal deposition technique where an electric field is created within a colloid dispersion by applying a constant voltage between two electrodes immersed in

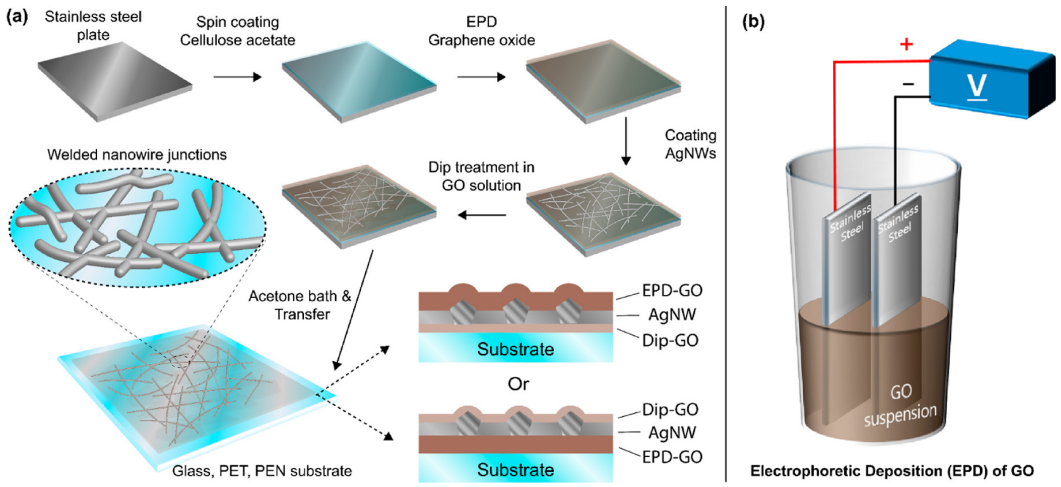

Figure 3-1: (a) Process flow for the fabrication of EPD-GO/AgNW/GO conductive films. (b) Schematic of the electrophoretic deposition (EPD) setup.

the solution (Figure 3-1b). This attracts and deposits the charged colloidal particles to the electrode with opposite charge to form a dense film. As GO flakes dispersed in water are negatively charged due to the abundant deprotonated carboxylate groups, deposits will be formed on the positively biased anode upon EPD. [113] The advantages of EPD over other solution-based processes include low cost, rapidity, simple equipment, controllable deposition rate, uniformity of deposition, and the possibility to be performed on surfaces with complex morphologies. [114] In conventional EPD, as the deposition substrate is the electrode, it is difficult to detach the deposited film from the SS substrate (electrode). Therefore, to allow transfer of the film from the substrate, a sacrificial layer made of cellulose acetate (CA) was coated on the SS substrate prior to EPD to liberate the deposited structure upon immersing in acetone, [113, 115] allowing transfer of the final EPD-GO/AgNW/GO film to arbitrary surfaces.

Upon deposition of the first GO layer by EPD (EPD-GO) on SS substrate to form EPD-GO/SS, AgNW was coated on top of the EPD-GO/SS by spin coating. The density of the AgNW is primarily responsible for the conductivity of the film and can be tuned by changing the concentration of AgNW solution and spin speed. It should be noted that the method of AgNW deposition can vary, and the inherent wettability of the GO allows AgNW to be easily coated by spray coating as well (Figure 3-2).

Therefore, our process has the flexibility to accommodate a variety of existing MNW coating techniques.

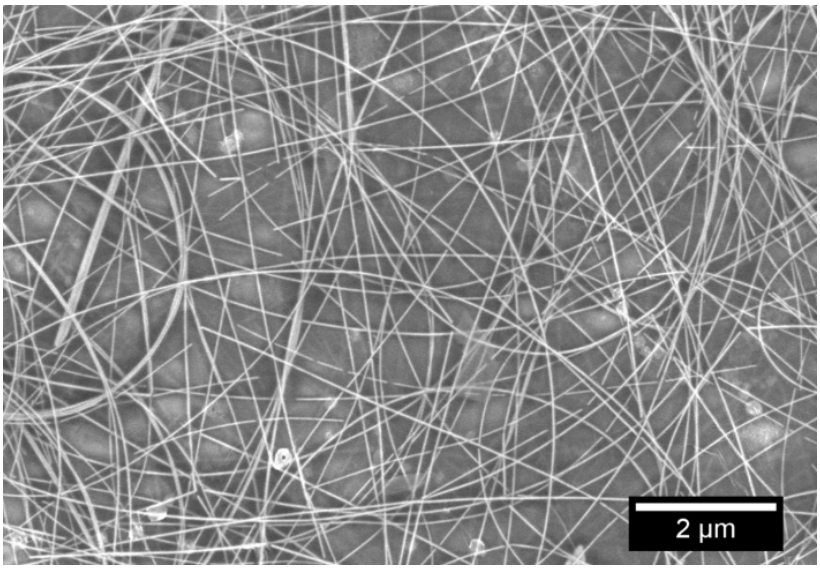

Figure 3-2: SEM image of EPD-GO/AgNW/GO film with spray-coated AgNWs.

The resulting AgNW/EPD-GO/CA/SS structure is then simply dipped in the GO dispersion, rinsed in water, and blow-dried. This dip-treatment covers the exposed AgNW with ultrathin GO flakes to mechanically weld or fix the AgNW onto the EPD-GO layer and to create a sandwiched structure of GO/AgNW/EPD-GO/CA/SS. As has been proposed by Pei et al., electrostatic attraction between AgNW and GO flakes in solution causes the AgNW network to be covered in an ultrathin GO coating composed of only a few layers. [85] Coating the AgNW by ultrathin GO at this stage of the process is also beneficial to affix the AgNW network onto EPD-GO. The contact between AgNW and EPD-GO prior to dip treatment was indeed observed to be poor as evidenced by delamination of the AgNW thin film at the air–water interface (Figure 3-3). Note that performing the second GO deposition by EPD instead of dip treatment is prevented since AgNWs already present on the deposition substrate (positive electrode) would simply dissolve as a result of the applied positive bias. The subsequent acetone bath detaches the EPD-GO/AgNW/GO film by dissolving the CA layer and allows transfer to arbitrary surfaces. As illustrated at the end of the process schematic of Figure 1a, transfer of the final conductive composite film can

be accomplished in two different orientations, where either the EPD-GO layer or the Dip-GO layer is facing up with respect to the target substrate.

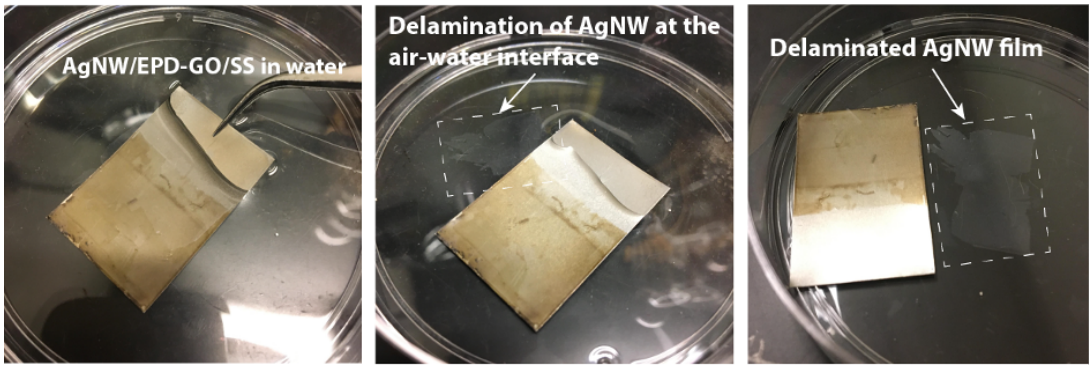

Figure 3-3: Image of AgNW film spin-coated on EPD-GO/SS being delaminated at the air-water interface prior to second GO coating by dip-treatment.

3.3 Structural characterization

Our fabrication process utilizing both EPD and solution dip treatment is not only scalable and cost-effective compared to existing techniques but also beneficial as it results in a novel composite structure where the AgNW network is "sandwiched" by two GO layers synthesized by two different means. The EPD-GO and Dip-GO that cover the AgNW network offer different properties to the final composite structure because of their structural differences which were characterized by SEM. Figures 3-4a and b show, respectively, the top and tilted view of the EPD-GO/AgNW/GO film, where EPD-GO is facing up, and illustrate the EPD-GO film following the topography of the underlying AgNW network. It is notable that thanks to the capability of EPD to form continuous films over macroscopic areas, EPD-GO did not show any discontinuities such as gaps or holes that would expose the underlying AgNWs to the external environment. Figures 3-4c and 2d are analogous images where Dip-GO is facing up. Contrary to EPD-GO, it was difficult to conclude that GO was seamlessly covering the NWs for the Dip-GO side. In most areas, the AgNW network appears to be seamlessly covered with GO based on the little contrast difference of the NWs. Figure 3-4c, which is the top-down SEM view of the Dip-GO treated side of the film,

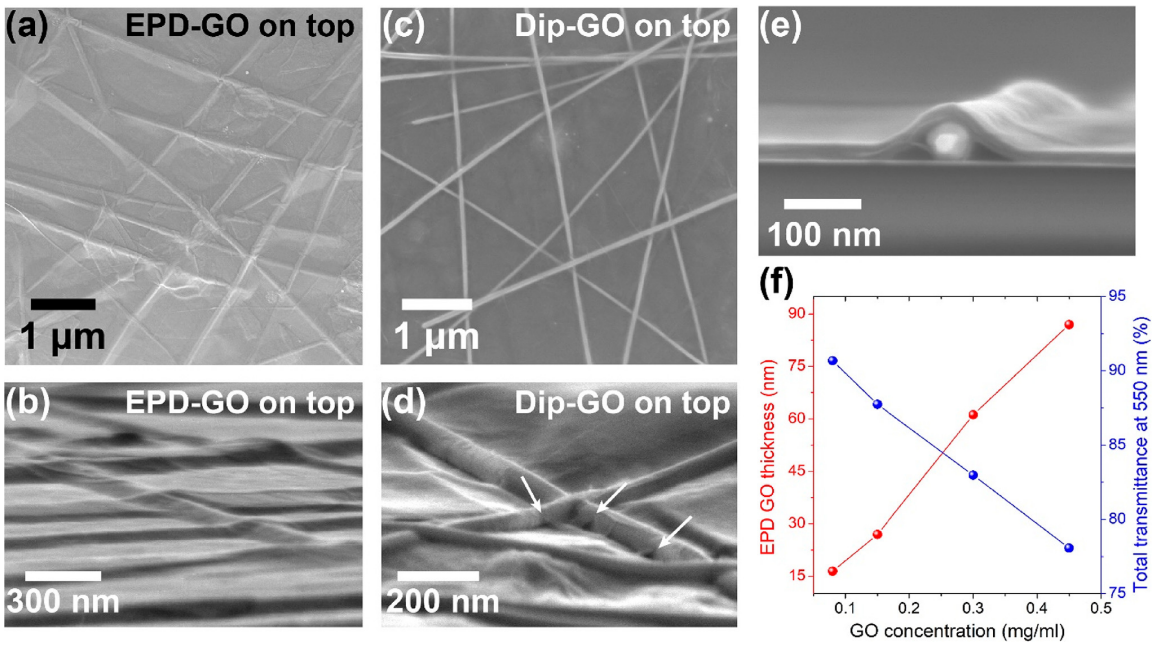

Figure 3-4: SEM images showing EPD-GO/AgNW/GO film in various perspectives including (a, c) top-down view, (b, d) tilted view, and (e) cross-section view. (f) EPD-GO film thickness and total transmittance (at 550 nm) as a function of GO solution concentration.

clearly shows individual AgNW surfaces even at a low acceleration voltage of 1 kV due to the ultrathin nature of GO. The contrast was observed to be uniform on the NWs, indicating GO flakes are completely covering the NWs in view. However, nanoscale gaps between GO flakes exposing bare AgNW were detected from the tilted view of another region of the same sample (Figure 3-4d), as indicated by the arrows. The presence of such nanoscale gaps and the contrast between individual Dip-GO sheets were more easily visualized by performing a dip treatment on AgNW networks on glass without underlying EPD-GO, as shown in the SEM images (in-lens detector) in Figure 3-5a,b. This may be due to the stochastic nature of the dip treatment as well as size differences (Figure 3-5c) between GO flakes and has implications for the AgNWs' chemical stability as will be discussed subsequently. Finally, an SEM cross-section image (Figure 3-4e) of the EPD-GO/AgNW/GO film clearly reveals the morphology of our film where NWs are covered by a thicker EPD-GO on one side and an ultrathin GO layer on the other side, demonstrating the effectiveness of our simple and solution-compatible process in creating a GO/AgNW/GO structure.

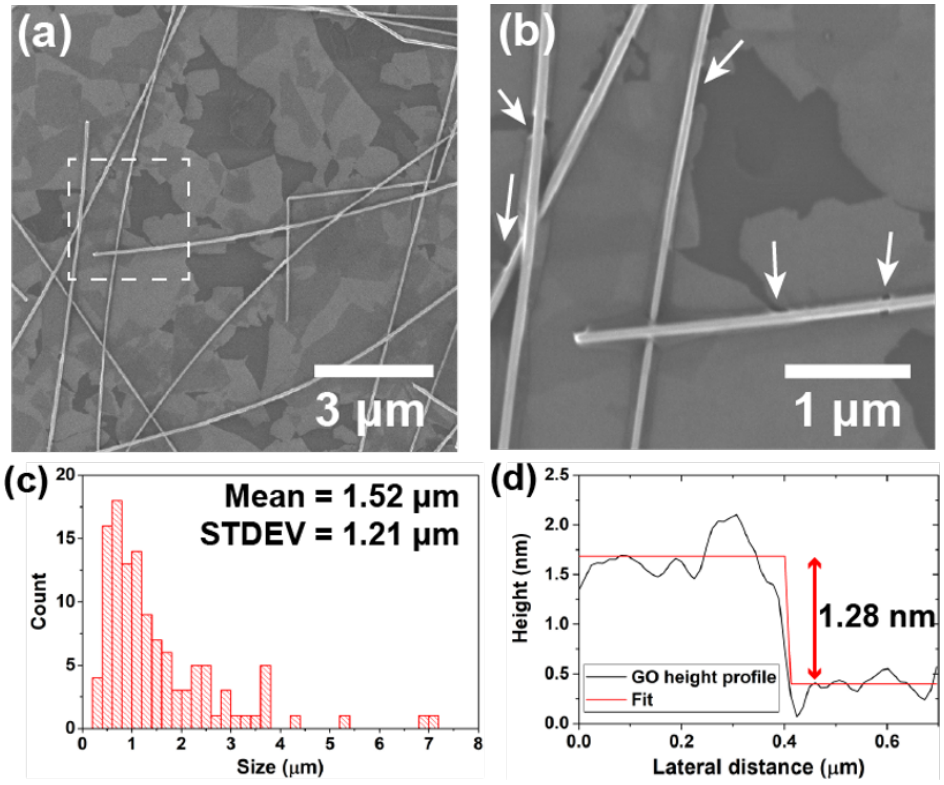

Figure 3-5: (a) SEM in-lens image of Dip-GO on AgNW deposited on a glass substrate. (b) Higher magnification view of the dashed square region in (a). Arrows indicate nanoscale gaps where AgNWs are not covered. (c) Size distribution of GO flakes showing large variation. Size was expressed in terms of equivalent square side length. (d) AFM profile of a single GO flake.

Utilizing EPD in the fabrication process allows the thickness of the GO to be easily controlled by simply tuning the deposition parameters. Among such parameters, the GO solution concentration was varied, while the deposition voltage and time were fixed in all experiments. Previous studies on the EPD of GO films [116] have demonstrated that the deposited mass is a linear function of the GO solution concentration, in line with the well-known Hamaker's law for EPD:

$$w(t) = f\mu EACt \tag{3.1}$$

where $w(t)$ is the deposited mass, f is the coefficient of deposition ($\ll 1$), μ is the electrophoretic mobility, A is the substrate surface area, C is the solution concentration, and t is the deposition time. [117] The thickness of EPD-GO films characterized

by atomic force microscopy (AFM) is plotted as a function of GO concentration in Figure 3-4f, revealing that the relationship between the thickness and GO solution concentration is close to linear. The detailed AFM images and height profiles of each EPD-GO film are shown in Figure 3-6.

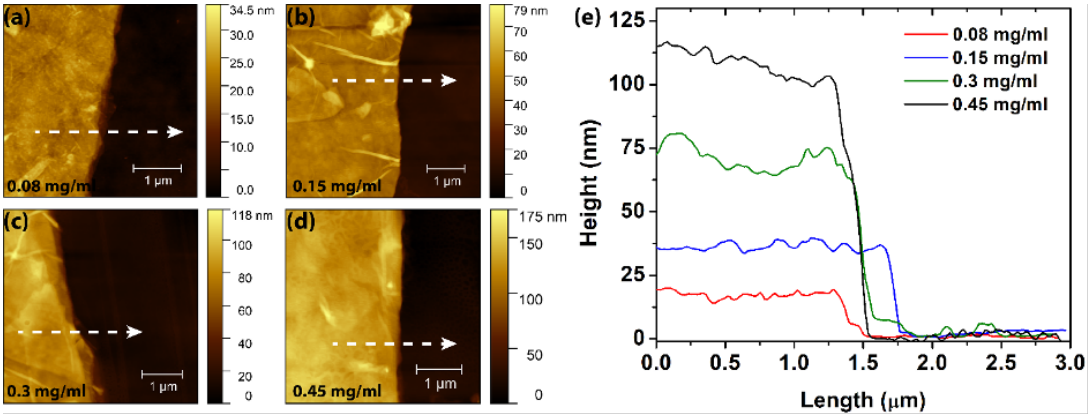

Figure 3-6: AFM image of EPD-GO films fabricated with GO solution concentrations of (a) 0.08 mg/ml, (b) 0.15 mg/ml, (c) 0.3 mg/ml, (d) 0.45 mg/ml. (e) shows the height profiles of the AFM images along the direction indicated by the white dashed arrows.

Although thickness of electrodeposited films has sometimes been reported to be inhomogeneous, particularly at the edges due to higher electric field strength at the deposition substrate edges, [118] our films exhibited very high thickness uniformity except at the sample edges (Figure 3-7). As can be seen in Figure 3-7a, the representative thickness of the EPD-GO film in this case was the value at the center, corresponding to 19.5 nm. Starting from the film edge, the thickness decreases quickly to within 10% of the center thickness from a distance of about 3 mm from the edge. This suggests that on a 25.4 mm square sample the EPD-GO thickness is perfectly uniform over a length of 19 mm, meaning that 75% over the 25.4 mm length across the film has uniform thickness. This value matches well with the region of uniform electric field intensity simulated by COMSOL for the same sample size, which was about 76% of the sample length (Figure 3-7b). This region of uniform field should correspond to consistent EPD-GO thickness, as EPD deposition thickness depends on the electric field intensity. [117] Furthermore, our simulations show that scaling up the substrate size increases the proportion of region with uniform field, which

suggests that edge inhomogeneity does not prevent EPD from being a scalable process (Figure 3-7b). While other strategies to mitigate the edge effect by employing different sizes for the deposition and counter electrode during EPD have already been investigated, [119] this is out of the scope of the present contribution.

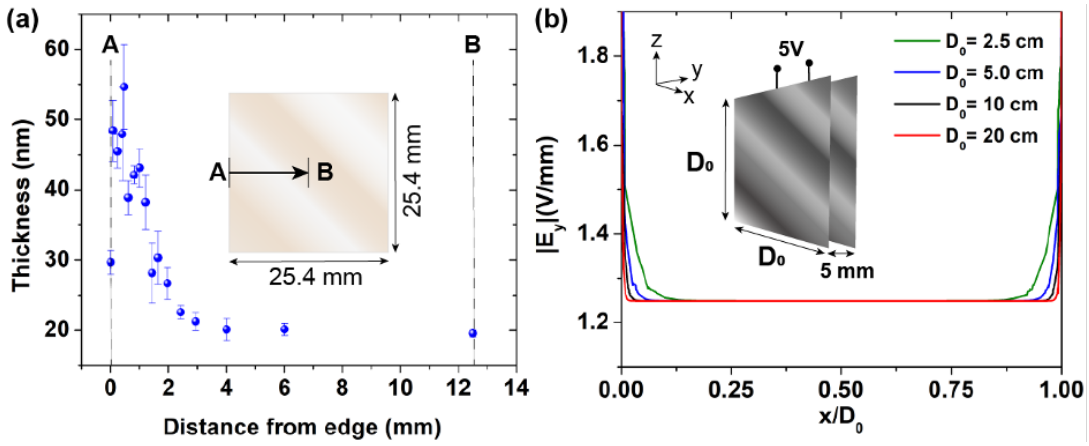

Figure 3-7: (a) Plot of the film thickness of an EPD-GO film measured by AFM against the distance from the edge of the sample. (b) Simulated intensity of electric field in the y direction 0.1 mm above the plate at the $D_0/2$ location, plotted as a function of x/D_0 (inset shows the parallel plate configuration simulated with COMSOL where 5V was applied between two square parallel plates of side length D_0, 5 mm distant from each other, in a water medium).

Implementation of EPD in our process allows facile tuning of the GO thickness from roughly 15 to 100 nm. This in turn enables the optical transmittance (at 550 nm) to be easily tuned across a wide range from 75% to above 90% (Figure 3-4f), compatible with various optoelectronic technologies using transparent conducting layers. [37] With longer deposition times and higher GO concentration, even thicker (micrometers thick) GO films can be easily realized through EPD. [114] Films with thicker GO-AgNW hybrid structures could potentially find applications in conductive membranes for electrochemical devices [120, 121] or electromagnetic interference (EMI) shielding. [122]

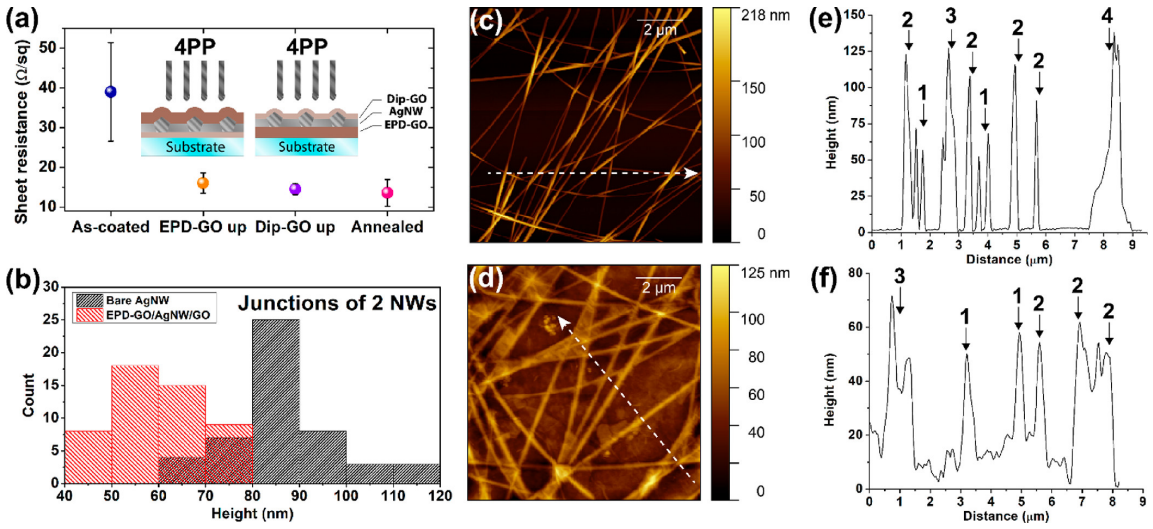

Figure 3-8: (a) Sheet resistance of EPD-GO/AgNW/GO films compared with bare as-coated or thermally annealed AgNW networks. (b) Histogram showing height distribution of two nanowire junctions. AFM images of (c) bare AgNW network and (d) EPD-GO/AgNW/GO film. (e, f) AFM height profile of the same.

3.4 Electrical and Optical properties

The mean sheet resistance and total transmittance at 550 nm are the most important optoelectronic performance metrics for transparent conductors in general. However, for MNW networks, electrical uniformity as well as light scattering deserves equally serious attention. [51, 99] In particular, ensuring low sheet resistance uniformly throughout AgNW networks is challenging due to the high resistances between individual AgNWs at the junctions and potential lack of uniformity in the AgNW coverage itself as opposed to conductive metal oxides with continuous film morphology. To assess the magnitude and homogeneity of our films, we have used the linear four-point probe (4PP) technique to measure the sheet resistance of our samples at five different locations. Although GO is an insulator, the 4PP measurements were possible for sufficiently thin GO thicknesses below 25 nm, which was achieved for EPD-GO fabricated with 0.08 and 0.15 mg/mL GO solution. Figure 3-8a shows the mean sheet resistances of the samples with various configurations along with the standard deviations over the five values measured in each case. As-coated bare AgNW networks exhibited a mean sheet resistance of 40 Ω/sq with a large standard

variation of 12 Ω/sq, indicating that the resistances between wires are not only high but are also widely varying. In contrast, bare AgNW annealed at 200 °C for 50 min showed a sharp reduction of sheet resistance to 13.6 Ω/sq and a reduced standard deviation of 3.3 Ω/sq, indicating that the majority of NW junctions have sintered to form more low-resistance conduction pathways. [34] Our EPD-GO/AgNW/GO films demonstrated similarly low and homogeneous mean sheet resistance values. For both the EPD-GO side (0.08 mg/mL GO) and the Dip-GO side, mean sheet resistance values were 16 and 14.5 Ω/sq, with standard deviations of 2.5 and 1.4 Ω/sq, respectively. As a consequence, electrical optimization was achieved without resorting to any thermal treatment. Note that the slight difference in the sheet resistance values associated with the sample with EPD-GO up and the one with Dip-GO up is due to slight fluctuations of the density of deposited AgNWs by spin coating, which is inherent for any percolating structures. The electrical performance is only driven by the density of AgNWs.

To further investigate the origin of the observed electrical optimization induced by the GO "sandwich" structure, we have performed AFM to characterize the NW junctions. Junctions where two NWs crossed were identified in the AFM images of EPD-GO/AgNW/GO films and bare AgNW networks, and the height across the junctions was measured and recorded. Figure 3-8b shows the height distribution of 50 junctions. It is clear that the overall junction height decreased for EPD-GO/AgNW/GO compared to bare AgNW, indicating partial, if not total, interpenetration between NWs. The interpenetration of NWs is also visibly apparent from the SEM image of Figure 2b,d. Example AFM images and height profiles of a bare AgNW network and EPD-GO/AgNW/GO film are shown in Figure 3-8c–f. The numbers above each peak in Figures 3-8e,f indicate the number of NWs in the junction encountered along the white dashed arrows in the associated AFM images. For both films, single NWs were measured to have similar height of roughly 50–60 nm, which is equal to their actual diameter. However, the heights measured for junctions of two or more wires are much lower for EPD-GO/AgNW/GO films than for bare AgNW where the heights of the junctions multiply in magnitude in accordance with the number of NWs. It is likely

that both the EPD-GO and the Dip-GO layers that cover the AgNW network enhance the physical contact between nanowires through downward force applied to the wires during drying of the film [85, 87] as well as from the adhesive force originating from hydrogen bonding between EPD-GO and Dip-GO nanosheets. [123] Concurrently, the uniform coverage of EPD-GO over the underlying AgNW network ensures that such junction optimization occurs homogeneously throughout the film. The combined effect of GO encapsulation mitigates the need for high-temperature treatment of NWs, making our process favorable toward using flexible plastic substrates.

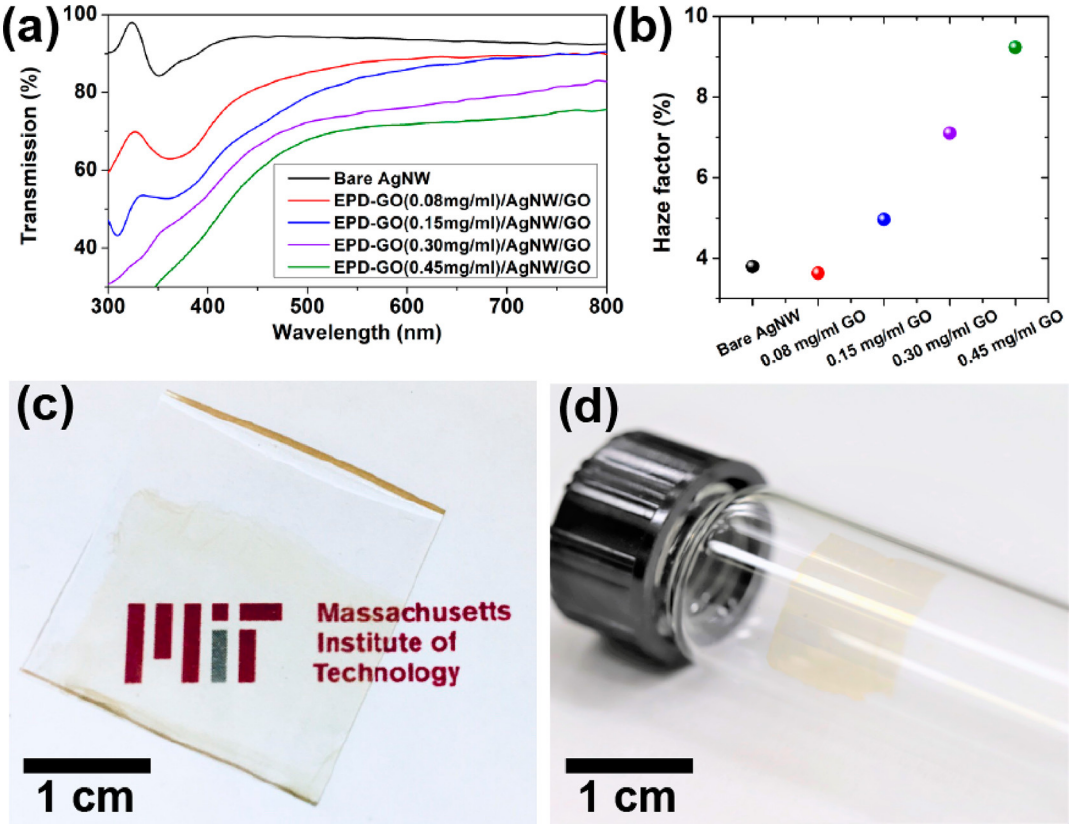

Figure 3-9: (a) UV–vis transmission spectra of bare AgNW and EPD-GO/AgNW/GO transparent electrodes fabricated with similar AgNW density ($R_{sh} = 18.2 \pm 1.6\ \Omega$/sq) but various GO concentrations used for EPD. (b) Haze factor (averaged 400–700 nm) as a function of increasing EPD-GO thickness. (c) Image of EPD-GO/AgNW/GO conductive film fabricated with 0.08 mg/mL GO solution, transferred on a 2.5 cm × 2.5 cm glass substrate and (d) transferred on a glass vial.

To assess the total transmittance and the degree of light scattering of our EPD-GO/AgNW/GO, we have performed UV–vis spectroscopy with an integrating sphere

setup. Figure 3-9a shows the total transmittance spectra in the wavelength range of 300–800 nm for AgNW networks of similar sheet resistance (R_{sh} = 18.2 ± 1.6 Ω/sq) as a function of the GO solution concentration used for EPD-GO fabrication. For all reported transmittance values the contribution from the underlying glass substrate is removed. It can be seen that the transparency of the film decreases with GO thickness and GO solution concentration used in EPD, as expected from the results shown in Figure 3-4f. Films fabricated with GO solution concentration of 0.08, 0.15, 0.3, and 0.45 mg/mL had a transmittance of 87.5%, 83.7%, 74.5%, and 70.8% at 550 nm, respectively. The uncoated AgNW network with a similar density had a transmittance of 93.8%. Using a GO solution concentration of 0.08 mg/mL for the EPD yielded the most transparent film, with a transmittance of 87.5% at 550 nm. As a reference, an image of this film on glass with a printed text background and on a 15 mL glass vial is shown in Figures 3-9c and 4d, respectively. Despite the slight loss in transparency compared to uncoated AgNW networks, our film is still compatible with many applications, where acceptable transmittance at 550 nm should be around 90%. [2, 124, 125]

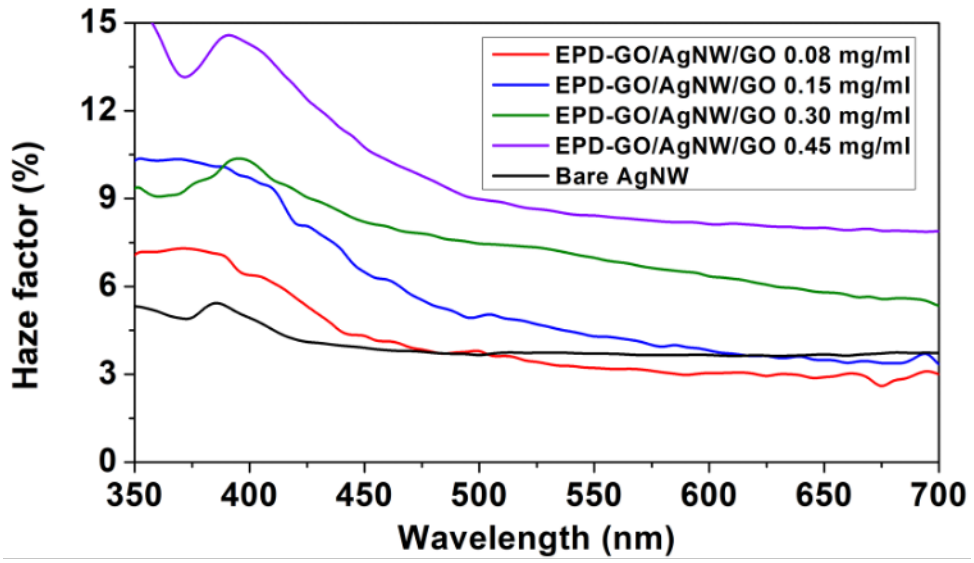

Figure 3-10: Haze factor spectra of EPD-GO/AgNW/GO films and bare AgNW in the 350-700 nm range.

The extent of light scattering can be assessed by calculating the haze factor, which

is the ratio of diffuse transmittance to total transmittance. Figure 3-9b shows the haze factor averaged in the 400–700 nm range for our EPD-GO/AgNW/GO films. Full haze factor spectra are shown in Figure 3-10. The haze factor increases with increasing EPD-GO thickness, with 3.6%, 5.0%, 7.1%, and 9.2% for the EPD-GO/AgNW/GO film, while the haze factor for the bare AgNW network was 3.8%. This is expected due to the random stacking of individual GO as well as the inhomogeneous nature of GO films which is composed of graphitic layers with various functional groups, void spaces, and water molecules. The refractive index mismatch at the interfaces caused by these inhomogeneities will lead to pronounced scattering as light passes through thicker GO films. Overall, the results suggest that by controlling the EPD parameters of GO, it is possible to predictably tune the level of transparency and haze. This could have critical implications toward using our electrodes in various applications that require different optical characteristics. For instance, high haze factor has been shown to be beneficial in organic solar cells due to increased light path length [99] while display applications require minimal haze for the sake of visual comfort.

3.5 Stability characterization

3.5.1 Chemical stability

The poor long-term chemical stability of bare, uncoated metallic nanowires such as AgNW is one of the major obstacles impeding their application. Therefore, we have assessed the chemical resilience of our EPD-GO/AgNW/GO electrodes by observing the change of their sheet resistance for a period of 20 days in comparison with that of annealed bare AgNW networks. Also, for EPD-GO/AgNW/GO electrodes, two cases were considered such that either EPD-GO or Dip-GO was facing the environment, and two different thicknesses of EPD-GO—15 and 25 nm—were chosen. The samples were stored in air at 80 °C to accelerate the degradation kinetics and were only taken out briefly once a day to measure the sheet resistance. The impact of humidity on

chemical degradation was assumed to be constant, given the insignificant relative humidity variations over the duration of the experiment. The relative humidity was measured to be very close to 55% for the entire duration of the experiment.

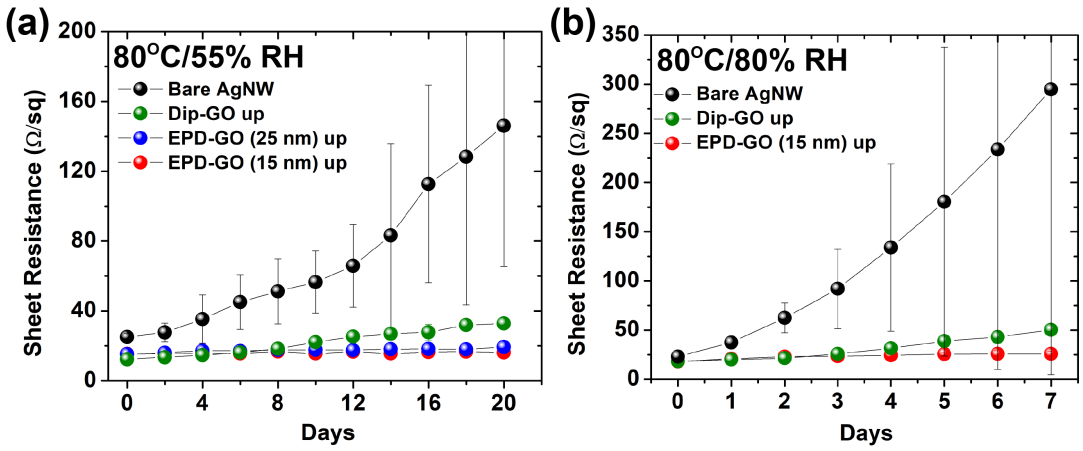

Figure 3-11: Environmental aging test of EPD-GO/AgNW/GO networks. (a, b) Sheet resistance variation for annealed bare AgNW and EPD-GO/AgNW/GO samples where either Dip-GO or EPD-GO was facing up, exposed to air for either (a) 20 days under a constant relative humidity of 55% or (b) 7 days under a constant relative humidity of 80%, both heated at 80 °C to accelerate the degradation kinetics. Note that bare AgNW, Dip-GO up, EPD-GO up (25 nm), and EPD-GO up (15 nm) samples exhibited transmittance values of 93%, 86%, 87%, and 83% at 550 nm, respectively.

Figure 3-11a shows the variation of sheet resistance for annealed bare AgNW and EPD-GO/AgNW/GO films. The samples had the same size and the same nanowire density as confirmed by their very similar initial sheet resistance. The aging process was performed simultaneously for all the samples. Bare AgNWs suffered from significant degradation as demonstrated by a 6-fold increase of their average sheet resistance after 20 days. Dip-GO provided some protection to the underlying NWs, but the mean sheet resistance still increased by a factor of 2.5 after 20 days. In stark contrast, when EPD-GO was facing up and serving a protective role against the environment, underlying AgNW networks retained their original sheet resistance for the entire duration of the experiment. The standard deviations shown in Figure 3-11a due to variations in measurement at different points on a sample indicate the degree of electrical homogeneity. The variance increases significantly to more than 110 Ω/sq

with aging for the annealed bare AgNW network, while for EPD-GO/AgNW/GO it retains its low initial value of less than 5 Ω/sq (Figure 3-12). This preservation of high electrical homogeneity suggests that the protection capability of EPD-GO is uniform across the film thanks to the continuous and seamless coating enabled by EPD. In this experiment, EPD-GO thickness of 15 and 25 nm yielded the same resilience against humidity. Hence, for EPD-GO thicknesses higher than 15 nm, the through-plane diffusion lengths of the corroding gas species are high enough to prevent them from reaching the AgNWs surface. [96] As will be further elaborated in Section 3.5.2, thin EPD-GO films are also expected to be more conformal around individual AgNWs than thicker films (Figure 3-15, insets). Therefore, decrease in conformality when increasing the EPD-GO thickness is likely to counteract the expected additional chemical protective capabilities offered by increasing the GO thickness, such that increasing the EPD-GO thickness ultimately has reduced benefit on the observed chemical stability.

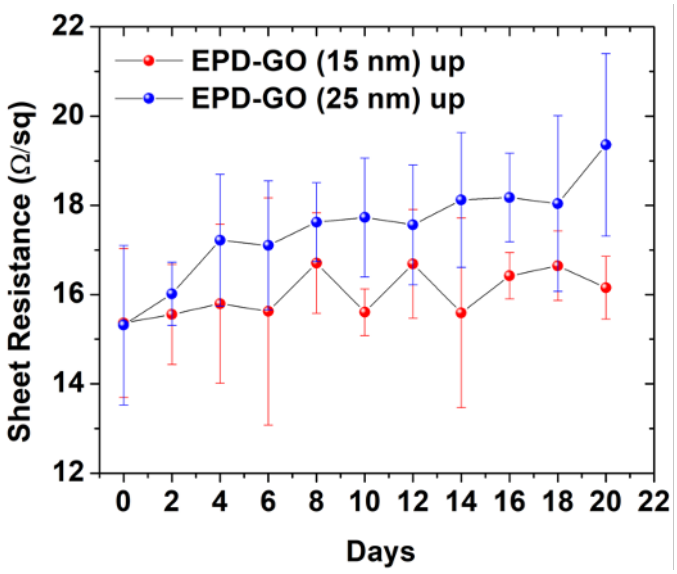

Figure 3-12: A Close-up of Figure 3-11(a); sheet resistance variation for EPD-GO/AgNW/GO samples where EPD-GO was facing up, stored in air at 80°C for 20 days.

To explain the chemical stability, morphology assessment by SEM imaging and chemical analysis by XPS were performed on the bare AgNW and EPD-GO/AgNW/GO electrodes after the degradation experiment. It should be noted that although the X-ray penetration depth is about 10 μm, only the top 10 nm can emit photoelec-

trons. As a consequence, when EPD-GO/AgNW/GO films are in the "EPD-GO up" configuration, the thickness of GO film (>10 nm) hinders accurate XPS analysis of the underlying AgNW. Therefore, we applied a double-sided carbon conductive tape onto the film and removed it, so that the entire film came off from the substrate with the tape without damage. This way, we have reversed the film orientation such that AgNWs covered by Dip-GO were exposed. As the Dip-GO is only 1–2 nm thick, this effectively exposes the AgNWs that had been covered by EPD-GO, allowing for their proper SEM and XPS characterization. Figure 3-13a–d shows SEM images of degraded bare AgNW network and EPD-GO/AgNW/GO films with either the Dip-GO or the EPD-GO layer facing up. The bare uncoated AgNW surface (Figure 3-13a) exhibits nanoparticle-like features and larger aggregates. These features are most likely Ag_2S, as has been identified in previous works as the principal corrosion product of AgNW that forms by the reaction of Ag with atmospheric sulfur-containing species such as carbonyl sulfide (OCS) and H_2S. [41] It is known that even a trace amount of these species in vapor, when aided by humidity and temperature, can induce significant sulfidation of AgNWs. Because Ag_2S particles are semiconducting and grow at the expense of Ag, it tends to increase the resistivity of AgNWs by thinning down initially pure Ag and disrupting the continuity of NWs. Although the overall coverage of the corrosion products is much less important than in the bare AgNW case, it was observed that AgNWs covered by Dip-GO (Figure 3-13b) were not completely free of such particles. In contrast, the surfaces of AgNWs that had been covered by both thicknesses of EPD-GO are free of such rough features, as can be seen in Figure 3-13c and d.

The presence of sulfidation products for bare AgNW networks and absence of sulfides for the GO-protected AgNW networks have been further confirmed by the XPS scan in the S 2p region, as shown in Figure 3-13e. For bare AgNW, a peak corresponding to Ag_2S is clearly visible near 162 eV, which can be deconvoluted into two peaks at 161.7 and 162.7 eV that correspond to the split energy levels caused by spin–orbit coupling. [41] Another peak situated at 168 eV and a shoulder peak at 168.7 eV correspond to sulfates, most likely Ag_2SO_4 or Ag_2SO_3, which are other

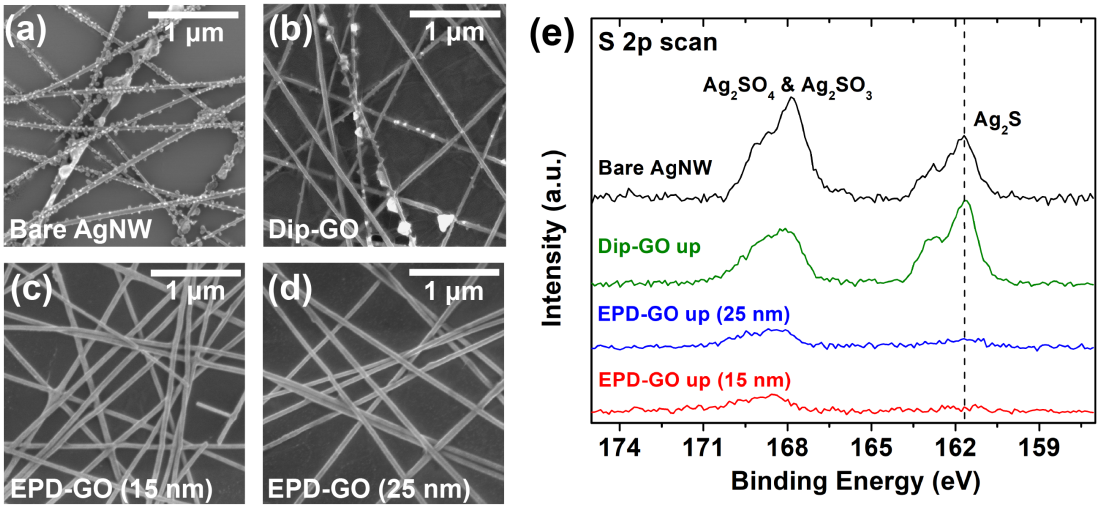

Figure 3-13: (a-d) SEM images of the degraded bare AgNW network and GO-covered AgNW networks with either the Dip-GO or EPD-GO facing the external environment, captured at the end of the aging experiment reported in 3-11(a). (e) XPS S 2p scans of the samples associated with experiment 3-11(a).

common products of silver sulfidation. [126] Similarly for Dip-GO covered AgNW ("Dip-GO up"), peaks corresponding to Ag_2S were clearly visible. This degradation can be explained by potential small gaps between GO flakes which were previously discussed and depicted in Figure 3-4d. On the other hand, the S 2p scan of the AgNWs that had been covered by EPD-GO ("EPD-GO up" samples) does not exhibit a sulfide peak expected at 162 eV, which is evidence that chemical degradation was greatly suppressed. Instead, a signal corresponding to sulfates was detected at 168 eV, which originates not from Ag but rather from GO. This was confirmed by an XPS scan in the S 2p and Mn 2p region performed on GO films only, which identified a peak corresponding to $MnSO_4$ (Figure 3-14 and Table 4.1). The residual $MnSO_4$ is expected since $KMnO_4$ and H_2SO_4 are commonly used for Hummer's method, the solution-based exfoliation of GO. [81, 127] Therefore, no XPS peak related to Ag corrosion product could be identified in the case of "EPD-GO up" samples. Also, the larger sulfate peak observed for "Dip-GO up" samples may be a combined signal originating from both Ag_2SO_4 or Ag_2SO_3 and $MnSO_4$. In summary, the results show that Ag corrosion has been prevented by the exceptional gas-barrier properties of the seamless EPD-GO that impeded transport of corroding gas species to the underlying

NW network. [128, 129]

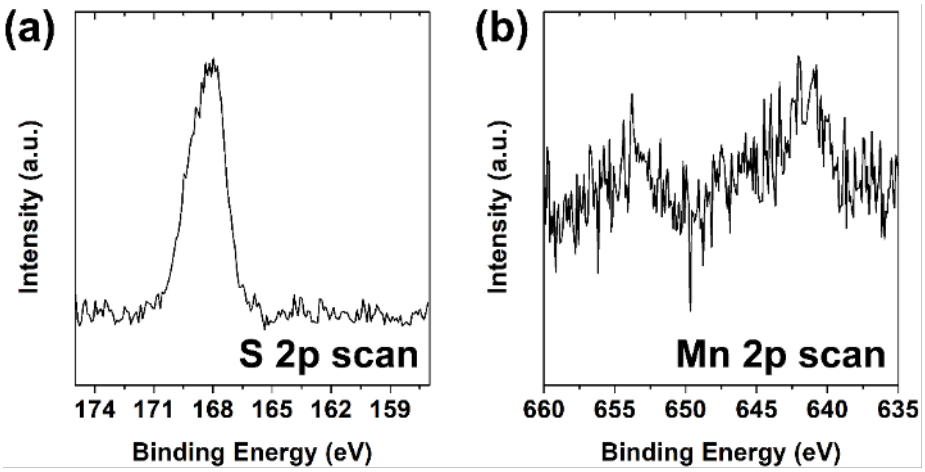

Figure 3-14: XPS spectra of bare EPD-GO films in the (a) S 2p and (b) Mn 2p regions. The S 2p peak at ∼168.1 eV and the photoelectron signal detected in the Mn 2p region suggests that $MnSO_4$ is present on the surface of GO.

XPS Binding Energies of S/Mn Compounds				
Compound	Peak	Observed BE (eV)	Reference BE (eV)	ref
Ag_2S	S $2p_{3/2}$	161.7	161.2	[41]
Ag_2S	S $2p_{1/2}$	162.7	162.3	[41]
Ag_2SO_3	S 2p	167.9	167.5	[126]
Ag_2SO_4	S 2p	168.7	168.6	[126]
$MnSO_4$	S 2p	169.8	169.6	[130]
$MnSO_4$	Mn $2p_{3/2}$	642	643	[131]
$MnSO_4$	Mn $2p_{1/2}$	654	655.1	[131]

Table 3.1: Summary of XPS binding energies and reference values for S/Mn compounds.

To evaluate the stability under even harsher environment, we also subjected bare networks and doubled-side GO protected networks under 80°C and 80% relative humidity for 7 days. Such a test was conducted in a similar fashion as the one reported in Figure 3-11a, except we used a humidity chamber to have a more precise and more reproducible control over the environment in such harsh conditions. The variation in resistance during 7 days of storage in those conditions is reported in Figure 3-11b. Results show that the mean sheet resistance of bare AgNWs rapidly increases by 12 times after 7 days due to high humidity that accelerates sulfidation. This is accompanied by increasing variation of sheet resistance within the sample, represented by

increasing variance. In contrast, samples where Dip-GO and EPD-GO (15 nm) were facing up demonstrated significant chemical stability even in such harsh conditions, evidenced by a mere 2.4-fold and 1.4-fold increase in the mean sheet resistance, respectively. The fact that we observe such chemical stability at high humidity conditions even though GO is hydrophilic indicates that GO impedes the penetration of sulfuric gas species through AgNWs, as also suggested by previous studies. [85, 87]

3.5.2 Electrothermal stability

The electrical stability of an AgNW-based transparent electrode is another important aspect of its overall robustness, particularly for transparent heater applications where DC voltage is applied to induce high temperature by Joule heating. In particular, it is of interest to delay and mitigate the abrupt failure experienced by AgNW-based networks above a certain voltage, which has been well-documented in prior studies. [69] Therefore, to fully evaluate the stability and reliability of our composite EPD-GO/AgNW/GO electrode, we measured its electrical resistance in situ while a linear voltage ramp (0.5 V/min) was applied. For the sake of clarity, normalization was done with respect to each samples' initial two-probe (2PP) resistance values. More details about the experimental setup can be found in Appendix A.

Figure 3-15 shows that the uncoated AgNW networks' resistance reduces slightly with voltage up to 5 V, followed by a steeper reduction until 9.5 V, and finally diverges to more than ∼105 times its original resistance over the course of only ∼20 s. The reduction of resistance can be attributed to NW junction optimization occurring due to Joule heating. However, a more intense Joule heating at higher applied voltages will lead to the catastrophic failure caused by the spheroidization of NWs due to Rayleigh instability. [69] A recent contribution by Sannicolo et al. [51] explains the resistance divergence by the initiation of a defect (or hot spot) induced by Joule heating, followed by the propagation of a crack parallel to the bias electrode stimulated by the constriction of current flow to the extremities of the initial defect. This "crack" composed of spheroidized NWs acts as an insulating region in the NW network that causes the measured resistance to diverge.

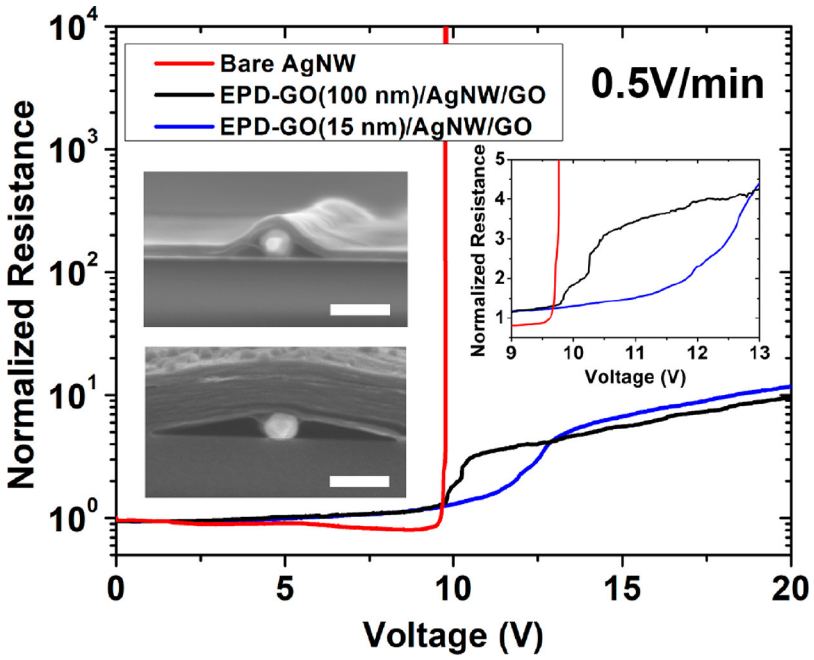

Figure 3-15: Resistance evolution during voltage ramp across bare NWs and EPD-GO/AgNW/GO films with different EPD-GO thicknesses. Values are normalized with respect to each samples' initial 2PP resistance performance. Inset graph shows magnified view of the main figure in the 9–13 V range. Insets are SEM cross-section images of the two EPD-GO/AgNW/GO films used. Scale bar is 100 nm.

With EPD-GO/AgNW/GO samples, a different behavior was observed where abrupt divergence of the electrical resistance is prevented. Figure 3-15 shows that at the initial stages of ramping the resistance of EPD-GO/AgNW/GO linearly increases, corresponding to the intrinsic resistivity increase of AgNWs by electron–phonon scattering. [33] Unlike bare AgNW networks, the resistance does not decrease for EPD-GO/AgNW/GO. This is further indication that the NW junctions are well-optimized by GO encapsulation, mitigating the need for thermal treatment to further weld the nanowires. An interesting behavior is observed as the voltage is ramped past 9.75 V. Here, the AgNW network undergoes an initial degradation as apparent from the deviation of the curves from the initial linear trend, but unlike in bare AgNWs, a complete loss of conductivity is prevented. Specifically, we have observed that the failure behavior depends on the thickness of EPD-GO layer covering the NW network. The inset of Figure 3-15 shows a close-up of the main plot in the range 9–13 V. For 100 nm thick EPD-GO, the resistance deviates from the original linear dependence

from ∼9.75 V onward, increasing to 3 times its initial value at ∼10.5 V over the course of ∼90 s. Interestingly, for 15 nm thick EPD-GO, the initial deviation from the linear behavior occurs at a slightly higher voltage around ∼11 V and increases to 4 times its initial value at ∼13 V over the course of ∼240 s. Therefore, we observe that the presence of EPD-GO slows down the initial NW failure compared to that of bare NWs, and thinner EPD-GO coating results in a higher failure onset voltage as well as a more gradual failure behavior. After this initial damage, both EPD-GO/AgNW/GO samples undergo slower increase in resistance up to 20 V. Even at 20 V, the electrodes exhibited a fairly low resistance near ∼150 Ω, a 10-fold increase from its original resistance. In the following paragraphs, we propose and discuss some mechanisms that are most likely to be responsible for our observation.

The observed delay in the onset of electrical degradation as well as the impeded degradation occurring in the early stages of electrical resistance increase may originate from two main mechanisms. First, the presence of EPD-GO and Dip-GO surrounding the NWs allows additional heat conduction pathways for the NWs, which helps dissipate the power generated by Joule heating. For an uncoated AgNW network under voltage bias, it has been demonstrated that the increase in temperature of the network is counterbalanced by heat losses in the substrate via thermal conduction, while the rest is lost via radiation and convection. [69, 132] In the case of GO-sandwiched AgNW networks, we speculate that the presence of EPD-GO and Dip-GO surrounding the NWs allows additional heat dissipation pathways for the NWs. The overall result is that AgNWs can support higher input voltage before reaching the temperature at which spheroidization is supposed to occur. Second, the presence of GO coating is also expected to slow down the AgNW spheroidization process by hindering atomic surface diffusion. For instance, it is known from previous studies that a conformal oxide coating on AgNWs drastically reduces the surface diffusivity of Ag atoms such that AgNW can sustain higher temperature and failure is initialized at higher voltages. [68, 103, 133]

As pointed out in Figure 3-15, the onset of failure was delayed only for the EPD-GO/AgNW/GO film with 15 nm EPD-GO and not for 100 nm EPD-GO. This may

be attributed to the different degrees of conformality of EPD-GO surrounding the AgNWs according to the EPD-GO thickness. From the inset SEM images of Figure 3-15, it can be seen that the thinner GO film can wrap around a larger AgNW surface area compared to its thicker counterpart. In general, deflections of thin membranes under a given load will vary as $\delta = KP/Et^3$ where δ is the deflection, P is the load, E is the Young's modulus, t is the film thickness, and K is a geometrical prefactor. Although recent micromechanical studies show that the Young's modulus of GO nanosheets is thickness-dependent, increasing for thinner GO films, the variation is not expected to significantly affect the strong $\delta \sim t^{-3}$ dependence. For instance, Cao et al. [134] report $E = 204$ GPa for 75 nm GO and $E = 291$ GPa for 24 nm GO. Given these parameters, under a given load, the displacement of the 75 nm film will be 20 times less than that of the 24 nm film. In our case, the load mainly originates from the capillary force induced by water evaporation during drying of the film after transfer. The strong influence of the thickness on the film's ability to be deflected is consistent with the increase in GO layer conformality over AgNW when minimizing the GO thickness. Also, the more tightly covered the AgNWs are, the more resilient they will be to spheroidization, which also explains the shift in the voltage failure observed in the thinner GO case. Use of thinner EPD-GO to improve the conformality could also minimize the observed loss in transparency. Further improvement of the conformality could be explored through the use of hot rolling press, for instance. [135]

Finally, beyond the change in behavior observed in the early stages of degradation (8–13 V), the slow increase in resistance observed at even higher voltages (13–20 V) can be explained as follows. Visual inspection of the EPD-GO/AgNW/GO electrode after completion of the voltage ramp test shows a darkened region localized at the center where the electrical crack has been initiated (Figure 3-17), and this corresponds to the region where maximum temperature higher than 250 °C was recorded with an IR camera (Figure 3-16). Because of this intense heat, NWs have spheroidized to a certain degree at this darkened area, while the NWs at the undarkened area were relatively intact (Figure 3-17a,c). XPS analysis performed at the end of the voltage ramp shows that this darkening is due to the partial thermal reduction of GO layers,

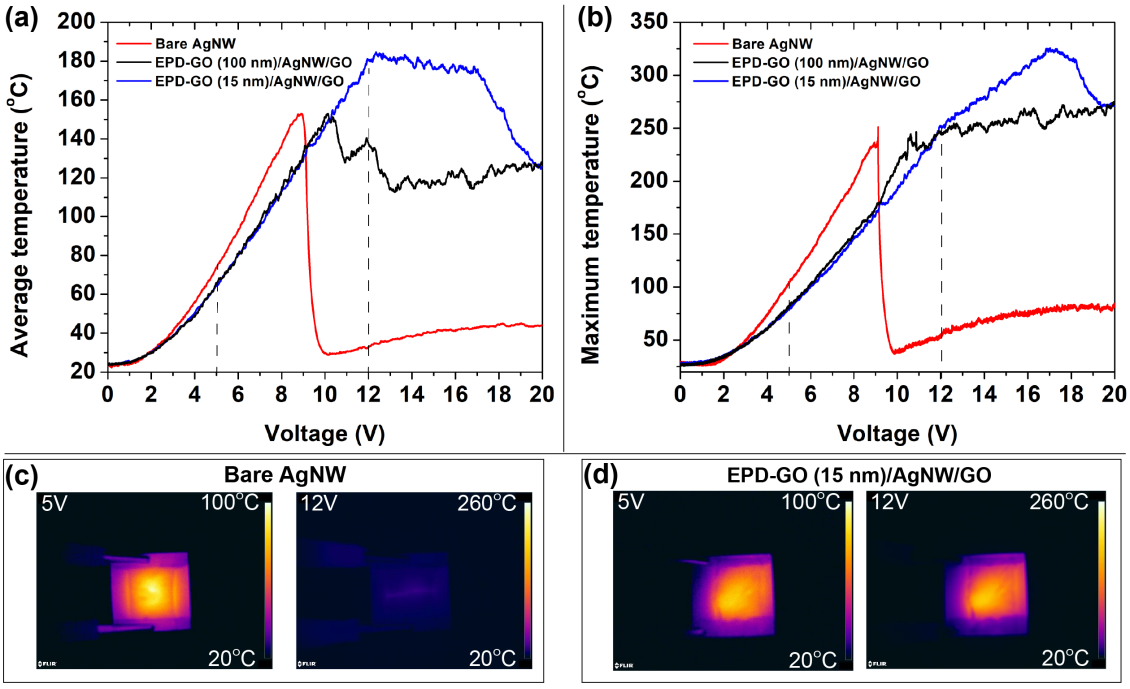

Figure 3-16: (a) Average and (b) maximum temperature evolution of bare AgNW and EPD-GO/AgNW/GO samples during voltage ramp. (c, d) Infrared camera images of the samples at selected voltages.

as depicted in Figure 3-17 d–f and Table 4.2. The survey scan indeed indicates a higher C/O ratio for the darkened region as well as a prominent increase in the carbon sp^2 peak in the C 1s scan. This is in line with recent heating studies of bare GO films which show that near 170 °C graphitic domains grow in size to the point when percolative electronic transport becomes possible, accompanied by sheet resistance reduction by 5 orders of magnitude. [136,137] Therefore, it is apparent that the center region of the GO coating is at least partially reduced during voltage ramp and plays a crucial role in preventing resistance divergence by acting as an additional current pathway. Therefore, we propose that the avoidance of resistance divergence at higher voltages (i.e., $V > 13$ V) is thanks to the reduction of GO sheets acting as an electrical bridge across spheroidized AgNW areas. In short, it can be seen that our GO encapsulation of AgNW networks effectively acts as a buffer that prevents breakdown at high applied voltages.

C 1s XPS Binding Energies in eV				
Moieties	Darkened GO	Not darkened GO	Reference BE	ref
C=C (sp^2)	284.6	284.9	284.5	[138]
C−C (sp^3)	285.3	284.9	285.5	[138]
C−O	286.8	286.9	286.5	[138]
C=O	288.2	288.3	288.5	[138]
COOH	289.3	289.3	289.5	[138]
$\pi - \pi^*$	290.5	N/A	291	[138]

Table 3.2: Summary of C 1s XPS binding energies of GO and RGO.

3.6 Application: Semitransparent Organic Solar Cell

To validate the applicability of EPD-GO/AgNW/GO (henceforth referred to as EPD-GO/AgNW/dip-GO), a use case was demonstrated as a top electrode (back electrode) of a semitransparent organic solar cell (ST-OSC) through a joint effort with Sannicolo et al. [107] GO coating may be seen as a cost-effective solution with a twofold function: protecting the AgNWs and acting as a device encapsulating layer when self-integrated with the back electrode. It should be noted that while examples of successful integration of AgNW hybridized with graphene-based materials as the front electrode in OSCs are available in the literature, [66, 139, 140] attempts to integrate such GO-AgNW composite structures as the back electrode in ST-OSCs are lacking in literature.

3.6.1 Device fabrication

We fabricated OSCs with the same core stack but various back electrodes and evaluated the impact of the back electrode configuration on the device performance and stability when exposed to lab atmosphere with various relative humidity (RH) values and to lab light. In each case, the core stack of the device consisted of ITO as the front (or "bottom") electrode, tin oxide (SnO_2) nanoparticles as the electron transport layer (ETL), a bulk heterojunction active layer comprising a polymer-donor "PV-D4610" and a fullerene acceptor $PC_{60}BM$, and PEDOT:PSS as the hole transport layer (HTL). To fabricate separate pixels within a single device, spray coating was used with a shadow mask to deposit the AgNW network, as was demonstrated in

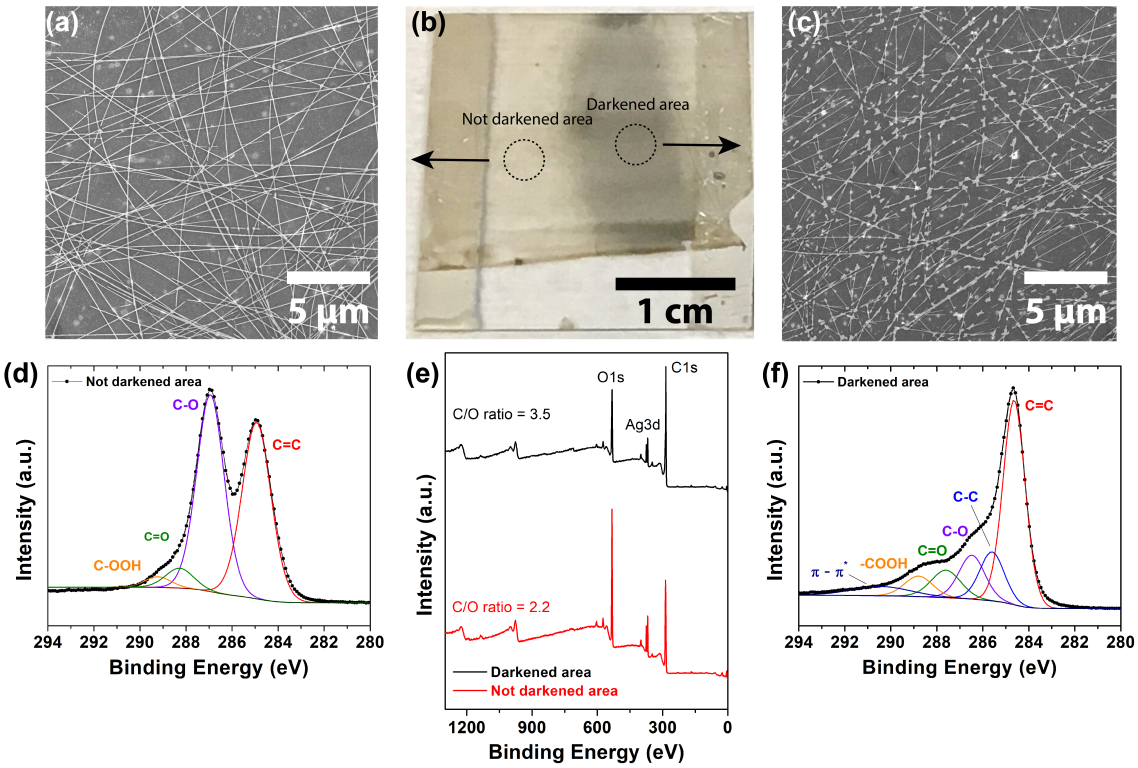

Figure 3-17: Characterization results for EPD-GO (15 nm)/AgNW/GO samples after completion of the voltage ramp. SEM image of underlying AgNWs of (a) not darkened area and (c) darkened area. (b) is the image of the film after completion of the voltage ramp. (d) and (f) show the XPS C 1s scan of the not darkened and darkened area, respectively. (e) show the XPS survey scan of the two areas which illustrates higher C/O ratio for the darkened area.

Section 3.2. A complete protocol with detailed information about the materials used, their associated deposition techniques, and the device characterization is available in Appendix A. Three types of back electrodes were fabricated and compared: (i) a homogeneous thin silver film (100 nm) deposited by thermal evaporation, (ii) a AgNW network deposited by spray-coating, and (iii) a AgNW network encapsulated with GO on both sides (EPD-GO/AgNW/dip-GO). Every sample consisted of six isolated active device pixels of 0.4 × 0.5 cm^2 on a 2.5 × 2.5 cm^2 glass substrate.

For devices associated with case (iii), a EPD-GO/AgNW/dip-GO structure was fabricated beforehand according to a procedure mentioned in Section 3.2. The latter structure could then be flipped and transferred in an IPA bath on top of the core stack of the device. Cross-linking the PEDOT:PSS layer with (3-glycidyloxypropyl)

trimethoxysilane (GOPS) [141] was essential to preserve the PEDOT:PSS integrity during device fabrication that involves water and to achieve semitransparent devices with high fill factors. A schematic of the protocol used in case (iii) is available in Figure 3-18A. Figure 3-18B,C shows SEM images of the dip-GO/AgNW/EPD-GO with the EPD-GO layer on top, after transfer on a glass sample.

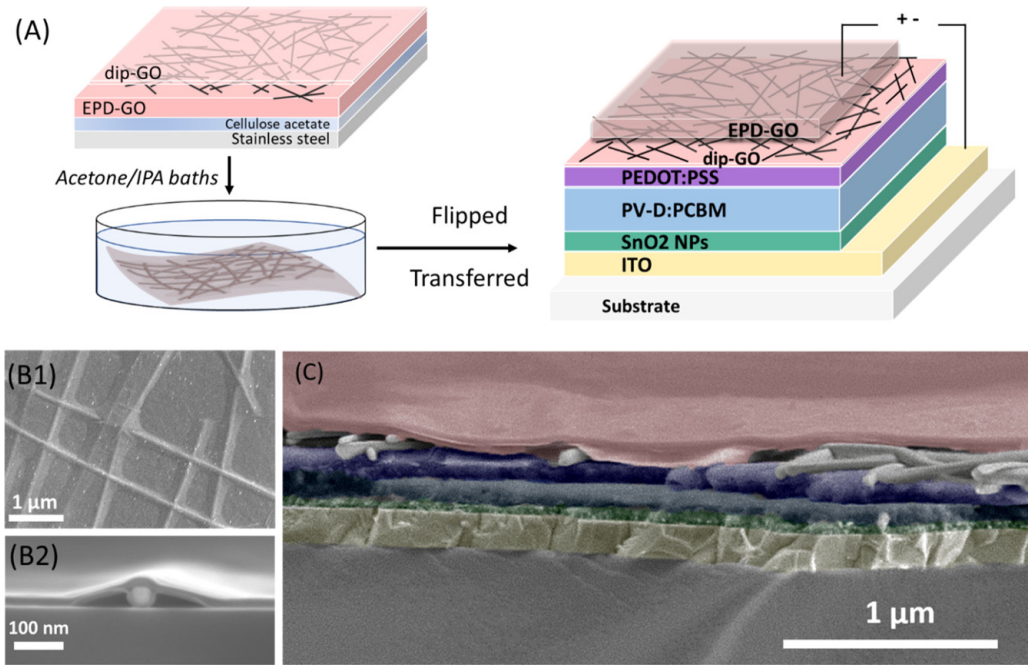

Figure 3-18: (A) Schematics showing the fabrication and transfer step of the dip-GO/AgNW/EPD-GO back electrode on top of the device's core. (B) SEM images of an EPD-GO/AgNW/dip-GO film transferred on a glass substrate in the top (B1) and cross-section (B2) views. (C) SEM image of the final device stack (tilted view) with EPD-GO/AgNW/dip-GO as the back electrode. Colors were added artificially. (ITO: yellow, SnO2 nanoparticles: green, PV-D4610:PCBM: blue, PEDOT:PSS: purple, AgNWs: gray, EPD-GO: red).

Protecting the AgNWs with GO on both sides does not negatively affect the intrinsic sheet resistance of the AgNW networks. On the contrary, GO layers induce a mechanical force at the junctions between nanowires which encourage interpenetration of AgNWs, leading to a slight reduction in R_{sh}, as mentioned in Section 3.4. The dip-GO layer is ultrathin and its thickness never exceeds 2–3 nm. Such GO ultrathin layer is used to further protect the AgNWs from the acidic PEDOT:PSS underneath. Because unreduced GO is insulating, it is of crucial importance that the dip-GO layer

remains ultrathin to allow Ohmic contact between PEDOT:PSS and AgNWs and to not affect the AgNWs' collection efficiency. [86, 142] On the contrary, the EPD-GO is not an active electrical component of the device and its thickness can be controlled within a wider range (typically 10–100 nm) by changing the GO concentration of the solution during the EPD-GO process. However, increasing EPD-GO layer thickness excessively is detrimental to the transparency of the device. However, for the sake of easy handling during the transfer step, a slightly thicker EPD-GO thickness was systematically targeted when making devices (typically 50 nm).

3.6.2 Device performance

The device performance after fabrication is reported in Figure 3-19A for the three back electrode configurations (along with a picture of the three types of devices). Note that for the bare AgNW top electrode configuration, both AgNW densities were investigated and marked as either "standard density" or "high density" depending on the number of spray cycles (6 cycles vs. 10 cycles), and the latter condition was used for EPD-GO/AgNW/dip-GO. The corresponding AgNW electrodes exhibited R_{sh}=9 Ω/sq and $T_{550} = 75\%$ for the "high density" AgNWs, and R_{sh}=30 Ω/sq and $T_{550} = 87\%$ for the "standard density" AgNWs.

Day 1 Solar Cell Parameters					
Back Electrode	PCE [%]	V_{oc} [mV]	J_{sc} [mA/cm^2]	FF [%]	R_{series} [$\Omega \cdot cm^2$]
Evaporated Ag	3.7	770	7.8	62	9
AgNW (Standard)	3.1	780	7.2	58	18
AgNW (High density)	3.3	781	6.8	63	15
EPD-GO/AgNW/GO	2.6	778	5.7	60	22

Table 3.3: Solar Cell Parameters of Devices Associated with the Three Back Electrode Configurations (Evaporated Ag, Bare AgNW, and Dip-GO/AgNW/EPD-GO) Directly After Fabrication.

As expected, the best PCE value (3.7%, as reported in Table 4.3) is achieved for the reference device which has a thermally evaporated Ag back electrode allowing for a maximized optical absorption of incident photons and collection of charge carriers.

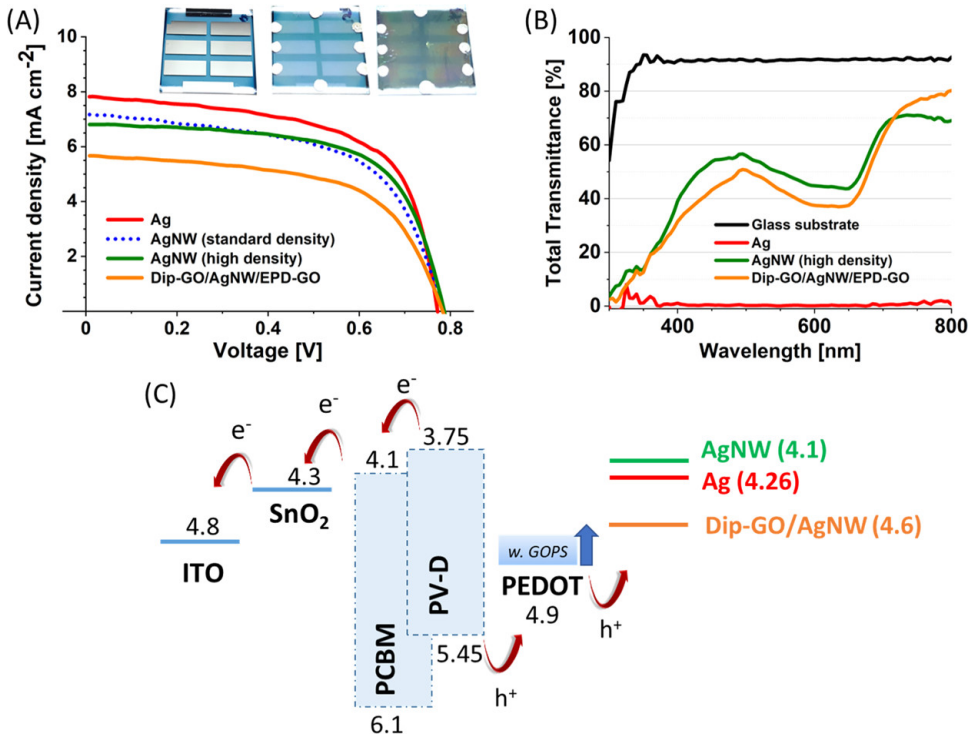

Figure 3-19: (A) J–V characteristics of OPV devices associated with the three back electrode configurations (e.g., silver, unprotected AgNW networks, and dip-GO/AgNW/EPD-GO). (B) Total transmittance of the three devices associated with the 3 J–V characteristics in (A). (C) Energy level [eV] diagram of the OPV devices investigated in this work.

When replacing Ag with discontinuous AgNW networks, one can still achieve devices exhibiting reasonable PCE values (3.3%) close to one of the reference devices. As compared to the reference device, the slight decrease in efficiency is mostly related to a lower J_{sc} value ($\approx$1 mA/cm^2 less) and a slightly higher R_{series} (see Table 4.3). The lower J_{sc} value is inherent to using a transparent back electrode. Contrary to when using an opaque electrode, the portion of non-absorbed photons cannot be reflected back in the active layer efficiently, inducing a certain amount of absorption losses. [143] The slightly higher R_{series} is because of a possible weak adhesion at the PEDOT:PSS/AgNW interface, as well as an inherently higher sheet resistance as compared to a continuous Ag thin film. However, given the solution-process compatibility of the AgNW network fabrication responsible for minimizing the costs (which is a key advantage in the frame of OSC technology), we consider the slight decrease

in efficiency as acceptable.

Beyond the cost, using a AgNW-based back contact electrode allows for achieving semitransparent organic PV (OPV) devices, which is technologically significant. The total transmittance of every device associated with the $J-V$ curves reported in Figure 3-19A is shown in Figure 3-19B. The device made with a AgNW back electrode exhibit a total transmittance of 49.7% at $\lambda = 550$ nm, whereas the reference device with a Ag back electrode is completely opaque. When using a double-sided GO encapsulated AgNW electrode, the total transmittance is decreased to 43.2% at $\lambda = 550$ nm. Such a difference is coherent with values discussed in Section 3.4 that protecting AgNW with GO layers as reported here causes around 6–10% decrease in transparency depending on the EPD-GO layer thickness.

In terms of PV performance, the device using a GO/AgNW/EPD-GO electrode exhibited similar V_{oc} and FF values to the device with a bare AgNW back electrode. However, its J_{sc} is decreased by around 1 mA/cm^2 (Table 4.3). For the sake of elucidating the difference observed in the J_{sc} values, the work function (Φ_s) of bare AgNW and dip-GO covered electrode configuration were measured by XPS. Note that contrary to the dip-GO layer which modifies the interface between PEDOT:PSS and the AgNW network, the EPD-GO layer does not influence the energy balance of the device. Φ_s values for the three back electrode configurations are reported in Figure 3-19C, along with the full energy level [eV] diagram of the OPV devices investigated in this work.

On average, the Φ_s associated with bare AgNW networks was measured to be 4.1 eV, a value close to the ones reported by several other groups. [144,145] When covering the AgNW network with a dip-GO layer (≈2–3 nm), the work function was increased by around 0.5 eV leading to an average value of 4.6 eV. Because PEDOT:PSS exhibits a Φ_s of 4.9 eV, the observed 0.5 eV increase in Φ_s of the electrode when inserting the ultrathin dip-GO layer between the HTL and the AgNW is not detrimental to the device energy balance and still allows for Ohmic transport of the holes.

As reported by Håkansson et al., [141] adding the GOPS cross-linker in PEDOT:PSS does not significantly modify the PEDOT:PSS work function. According

to the authors, a volume ratio of 0.6% GOPS in the PEDOT:PSS films can lead to a relative shift of ∼0.25 eV in the PEDOT:PSS work function. For 1% volume ratio and higher, however, Håkansson et al. measured the relative shift in Φ_s to be more significant around 0.5 eV. [141] In the present contribution, the 30 wt % GOPS added to the PEDOT:PSS corresponds to a lower volume ratio of 0.4%. Hence, the modified HTL work function is not expected to be lower than 4.65 eV, a value still compatible with Ohmic transport when in contact with a 4.6 eV dip-GO/AgNW electrode (Figure 3-19C).

Therefore, the slight decrease in J_{sc} observed when adding the dip GO layer between the PEDOT:PSS layer and the AgNW network does not originate from any work function mismatch that would lead to enhanced charge recombination at the interfaces. In this specific case, potential morphology defects, for example, microscale wrinkles in the dip-GO layer, created during the top electrode transfer onto the device stack might have been the location of additional charge recombination near the PEDOT:PSS – dip-GO interface. Because the dip-GO layer is so thin (≈2–3 nm), such assumption is hard to confirm with conventional nano-characterization tools. However, the slight decrease in device efficiency when adding GO can be counterbalanced by the significant improvement in its stability and lifetime, as discussed hereafter.

3.6.3 Device stability

To evaluate the benefits of double-sided GO encapsulation around the AgNW-based back contact electrode on the device stability, a large set of devices associated with the three back electrode configurations was fabricated and their solar cell parameters were measured over a period of 26 days. All devices were exposed to lab atmosphere and lab light during the entire aging duration. The relative humidity (RH) and temperature were automatically recorded every minute, leading to average values of 28% RH and 22 °C, respectively.

Figure 3-20A shows the averaged J_{sc} values over all the tested device associated with the three configurations. More specifically, for the "evaporated Ag" back electrode (red curves) and the bare AgNW back electrode with either standard or high

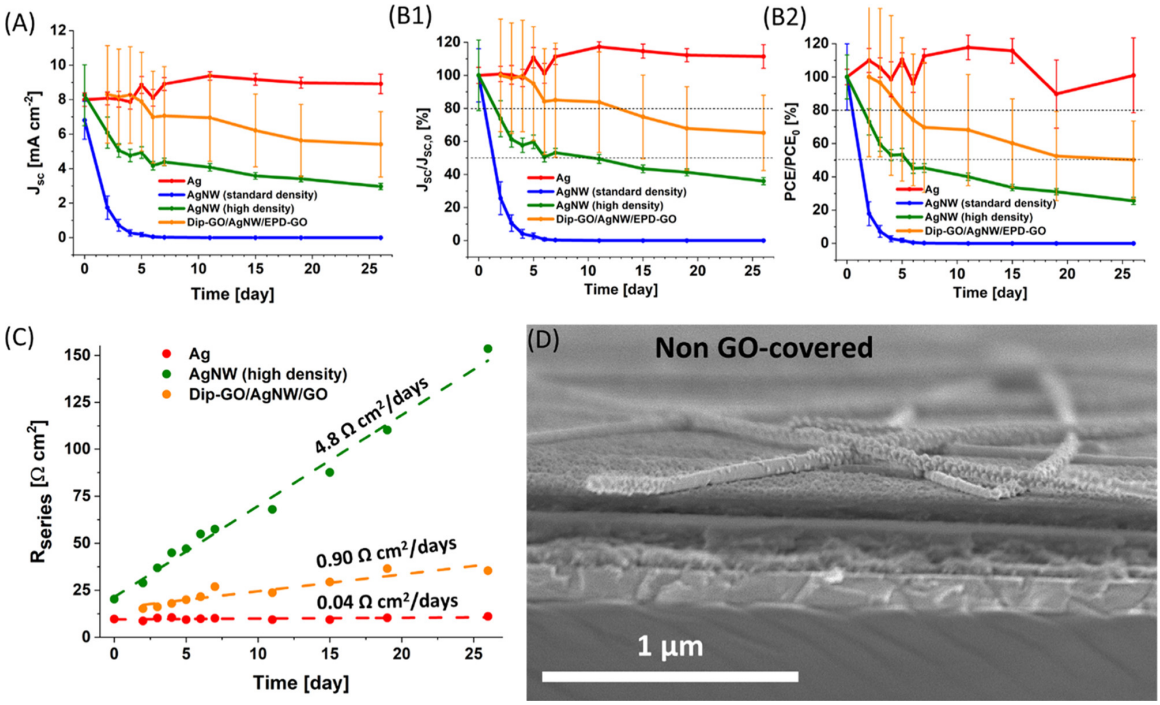

Figure 3-20: (A) Evolution of the averaged JSC values of OPV devices with the three back electrode configurations, measured over a period of 26 days, while stored in lab atmosphere (22 °C, 28% RH) and exposed to lab light. (B1–B2) Evolution of the normalized JSC and PCE values with respect to their initial value for the same set of devices. (C) Evolution of Rseries over time for the three back electrode configurations. (D) SEM image (tilted view) of the cross-section of a device with a bare AgNW back electrode at the end of the aging test.

AgNW density (blue and green curves), the J_{sc} and every other solar cell parameter were averaged over the performance of 12 devices in each case (2 samples with six device pixels each). For the dip-GO/AgNW/EPD-GO configuration (orange curve), they were averaged over 24 devices (4 samples with six device pixels each). The error bars associated with curves are also reported in Figure 4A. Note that higher error bars associated with the dip-GO/AgNW/EPD-GO device configuration originate from a larger number of devices being tested along with a slightly less favorable and stable probing when measuring device because of the presence of GO on top of the AgNW networks.

J_{sc} is the critical parameter for evaluating the aging behavior of the active layer and the PEDOT:PSS layer. As expected, opaque devices with a thermally Ag back electrode exhibits the most stable J_{sc} over time, while semitransparent devices exhibit

either a slow or fast decrease in J_{sc}. It was observed that the less covered/protected the active layer and the PEDOT:PSS layer, the faster the decrease in J_{sc}. Devices with the bare AgNW electrode (standard density) indeed exhibits the lowest coverage, followed by the AgNW electrode (high density). Thanks to the GO-enhanced coverage, the devices with a dip-GO/AgNW/EPD-GO back electrode exhibit a significantly slower decrease in J_{sc}. This is a clear evidence of the encapsulation function offered by the GO layers.

The ratio $J_{sc}/J_{sc,0}$ with $J_{sc,0}$ as the initial short-circuit current density value is also plotted in Figure 3-20B1. $t_{j,80}$ and $t_{j,50}$ represent the storage time when such ratio equals 80 and 50%, respectively. On the one hand, when AgNWs were not encapsulated with GO, $t_{j,80}$ and $t_{j,50}$ were both lower than 2 days for standard density electrodes (blue curve). For high density electrodes (green curve), $t_{j,80}$ was lower than 2 days, while $t_{j,50}$ was around 6 days. As a consequence, unprotected AgNW networks as the back electrode does not allow for a decent lifetime of the OPV device. On the other hand, $t_{j,80}$ and $t_{j,50}$ associated with double-sided GO-protected AgNW back electrode (orange curve) exceeded 11 days and 26 days, respectively, which represent around a fivefold increase in the J_{sc} stability.

Contrary to non-protected AgNW devices which exhibited a steep slope down in the early stages of the aging test, GO-coated AgNW devices showed very high stability up until 5 days. However, the period of high stability was then followed by a slow and regular decrease, at a similar rate compared to non-protected devices. Such transition in the evolution of J_{sc} can be explained by the occurrence of a so-called "lag-time" in the permeability of GO against gaseous species such as oxygen. For instance, Yamaguchi et al. reported a lag-time of 100 hours for 20 nm thick GO films, [146] in line with a the lag-time of around 5 days observed in the present case. Interestingly, the oxygen/moisture barrier performance of GO can be further increased when reduced as a result of the reduced interlayer distance between graphene planes, thus clogging the preferential permeation paths. [146, 147] Given that reducing GO is at the cost of the film transparency, reduction of the thick EPD-GO layer would jeopardize the semitransparency of the device. Instead, reducing only the ultrathin

dip GO layer could potentially bring additional resilience against oxygen and water permeation without significantly affecting the optical transmittance. While out of the scope of the present contribution, this could be seen as a promising way to take further advantage of the versatility offered by the dip-GO/AgNW/EPD-GO sandwich structure.

Although the evolution of the J_{sc} parameter is very relevant to get a sense of the aging behavior of both the active layer and PEDOT:PSS layer within the device stack, interfaces and the electrodes may also be subject to degradation. [148] R_{series} mostly accounts for the contact resistance between the HTL and the back electrode, as well as for the sheet resistance of the electrodes themselves. For each device configuration, we extracted R_{series} from the various J-V curves generated during the aging test. The typical evolution of R_{series} for the three back electrode configurations is reported in Figure 3-20C. While R_{series} remained low and exhibited an almost negligible increase of 0.04 $\Omega \cdot cm^2$/day for opaque devices with an Ag electrode, R_{series} increased more significantly over time for semitransparent devices. However, such increase was almost 5 times faster for devices with unprotected AgNW back electrode (4.8 $\Omega \cdot cm^2$/day) than for devices with double-sided GO-protected AgNW back electrode (0.9 $\Omega \cdot cm^2$/day). The contributing factors for R_{series} include the resistance of AgNW network itself, interface between AgNW and PEDOT:PSS, and the quality of the PEDOT:PSS layer itself, assuming the active layers are intact which is typically the case for organic solar cells. Since it was shown that the quality of AgNWs themselves remain intact by EPD-GO overcoating in Section 3.5.1., and that it also promotes contact between AgNW and the underlying surface, it is most likely that the degradation of hygroscopic PEDOT:PSS itself is the limiting culprit of cell degradation for EPD-GO/AgNW/GO devices, consistent with prior literature. [149]

As shown in Figures 3-20D and 3-21A, a significant change in the morphology of both the PEDOT:PSS front surface and AgNWs was detected after aging. The AgNWs exhibited many nanoparticle-like features on their surfaces. Such aging products are most likely Ag_2S which originate from the reaction of Ag with atmospheric sulfur-containing products, as discussed in Section 3.5.1. Such semiconducting nanoparticles

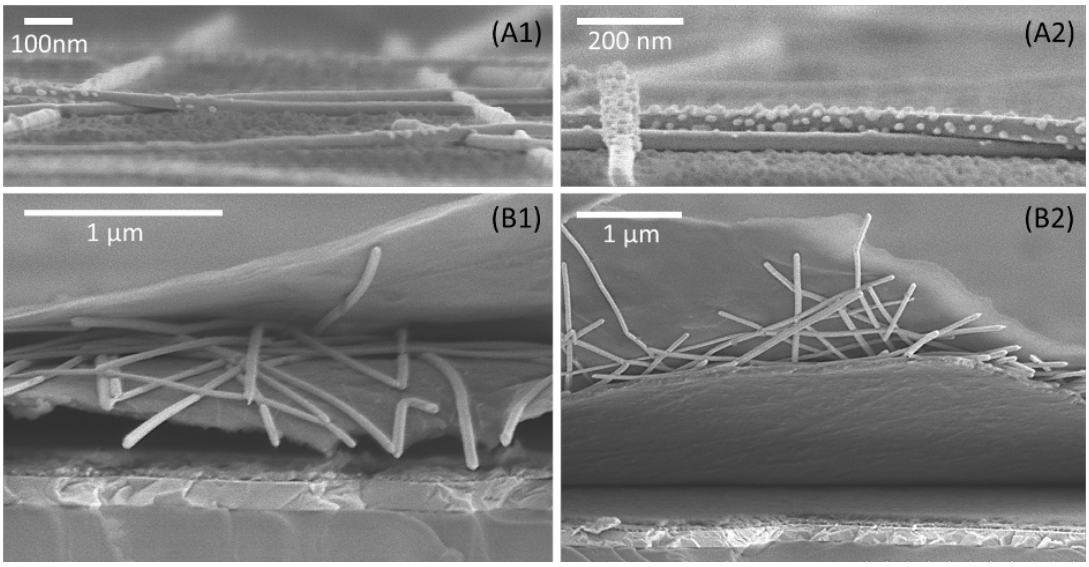

Figure 3-21: (A1-A2) SEM images (tilted view) of the surface of a device with a bare AgNW back electrode captured at the end of the aging test. Both PEDOT-PSS surface and AgNWs appear to be significantly degraded. (B1-B2) SEM images (tilted view) of the cross-section of a device with a double-sided GO-protected AgNW back electrode captured at the end of the aging test. Delamination of the PEDOT:PSS and above layers of the device stack occurred during the cutting process, allowing for visualizing "inside" the device. The AgNWs exhibit no sign of degradation.

tend to increase the resistivity of individual AgNWs, leading to an increasing sheet resistance over time and resulting in a higher R_{series} for the device. On the contrary, such particle-like features around the AgNWs were not visible when encapsulated with GO (Figure 3-21B).

Additionally, we evaluated the impact of PEDOT:PSS on the degradation of AgNWs by measuring the evolution of the electrical resistance of several AgNW networks, either uncoated or coated with either bare PEDOT:PSS, GOPS–PEDOT:PSS, dip-GO/PEDOT:PSS, or dip-GO/GOPS–PEDOT:PSS. Figure 3-22 reports the evolution of their electrical resistance normalized against their initial resistance. Samples were all stored in a humid environment of 80% RH, and their resistance was measured once every day. As expected, the bare AgNW network underwent the fastest increase in resistance, closely followed by the AgNW network coated with bare PEDOT:PSS which underwent a 300% increase after 13 days. Such fast degradation originated from the release of H^+ ions in solution by sulfonic groups (-SO_3H) of the excess PSS,

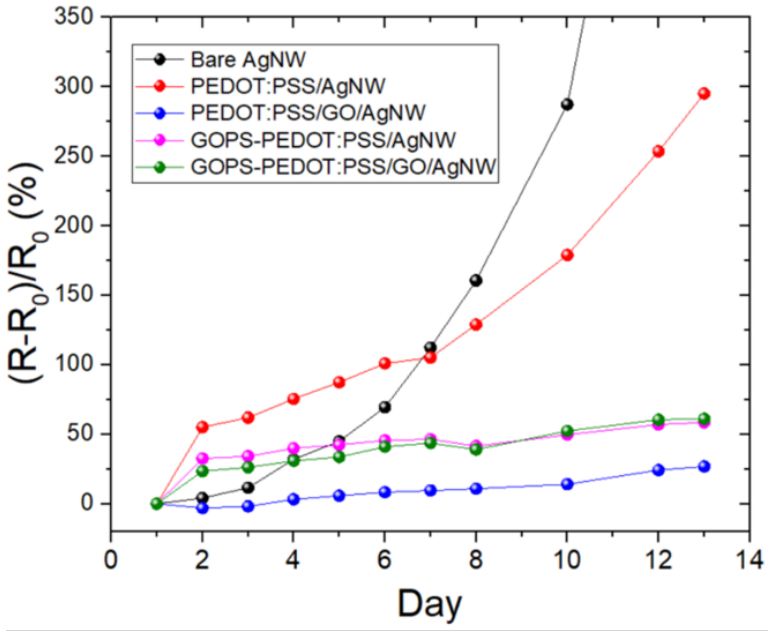

Figure 3-22: Evolution the electrical resistance (normalized against the initial resistance) of several AgNW-based networks, either uncoated or coated with either bare PEDOT:PSS, cross-linked GOPS-PEDOT:PSS, dip-GO/PEDOT:PSS, or dip-GO/GOPS-PEDOT:PSS. The samples were stored in humidity chamber at 80 % RH/25°C for the entire duration of the aging test.

causing acid corrosion of AgNWs. Interestingly, when inserting a ultrathin dip-GO layer between the AgNWs and PEDOT:PSS, the normalized resistance was barely modified, resulting in an increase of only 20% after 13 days (Figure 3-22). This highlights that the insertion of the dip-GO layer is essential to preserving AgNWs from PEDOT:PSS-induced acidic corrosion. It should be noted that the AgNW networks coated with cross-linked GOPS–PEDOT:PSS also exhibited a good electrical stability. We assume that the cross-linking mechanism occurring between GOPS and the sulfonate groups of the excess PSS helps delaying significantly the release of H^+ ions responsible for the acidic corrosion of the AgNWs.

Because the PCE takes all the solar cell parameters into account, the overall increase in the device stability when adding GO can also be evaluated when plotting the evolution of the normalized averaged PCE with respect to its initial value PCE_0 (Figure 3-20B2). For bare AgNW back electrodes, the corresponding $t_{PCE,50}$ increased from lower than 2 days (standard density) to 5 days (high density). For double-sided

GO protected AgNW back electrodes, $t_{PCE,50}$ went up to 26 days, which corresponds to more than a fivefold increase.

3.7 Conclusion

By utilizing EPD and dip treatment of GO, we have developed a scalable and solution-based processing method to fabricate resilient EPD-GO/AgNW/GO transparent conductive films capable of being transferred to arbitrary substrates. Structural characterization by SEM shows that the AgNW network is effectively "sandwiched" between two GO layers, with one side covered by a seamless EPD-GO thickness as low as 15 nm and another side by 1–2 layers of GO. The GO encapsulation allows intimate contact between individual AgNW junctions, which effectively reduces the high junction resistance down to 15 Ω/sq without relying on high-temperature annealing of the NWs and allows electrical uniformity across the entire film. Simultaneously, the transmittance of the film and its haziness were shown to be tunable between 70% and 87% at 550 nm and between 3.6% and 9.2%, respectively, by simply changing the EPD-GO thickness. Importantly, we show that the sufficient thickness and defect-free quality of the EPD-GO film impart exceptional chemical stability to the AgNWs by mitigating spontaneous sulfidation of Ag that leads to conductivity loss. Furthermore, in situ resistance measurements during linear voltage ramp on our films showed that the catastrophic resistance divergence to the MΩ range which is typical of bare AgNW networks was avoided even at a high applied voltage of 20 V. Although this novel electrical stabilization behavior warrants further scrutiny, we believe that the effects of delayed spheroidization of NWs by GO coating, thermal management by heat conduction through GO, and reduction of GO are collectively responsible for the observed behavior.

Thanks to its double-sided structure, our EPD-GO/AgNW/GO transparent electrode can offer combined assets, which is favorable toward its compatibility with various devices. On the one hand, the relatively thicker and seamless EPD-GO side offers outstanding chemical and thermal resilience to the outside environment, making

the electrode compatible with either high voltage, temperature, or humidity sensitive applications such as transparent heaters or thermochromic windows. On the other hand, the ultrathin Dip-GO layers offer improved stability while still allowing Ohmic contact through any potential adjacent layers, making it compatible with applications sensitive to efficient charge carrier transfer or energy level matching, such as solar cells or LEDs. Depending on the architecture of the target device, one or the other configuration could be preferred and easily controlled during the film transfer step.

The above idea was explored by a joint effort with Sannicolo et al., [107] where the double-sided EPD-GO/AgNW/dip-GO TE was integrated as a back electrode for Semitransparent Organic Solar Cells (ST-OSC). Here, the GO double-sided GO layer, namely EPD-GO and dip-GO on opposite sides of the AgNW network, serve a dual role in the context of ST-OSC. First, the EPD-GO layer facing the environment is aimed at encapsulating the device, limiting water and gas penetration within the device as well as maintaining the integrity and performance of the AgNW electrode. Secondly, the ultrathin dip-GO layer underneath the AgNW network is facing the inside of the device stack, preserving the integrity of AgNWs against the PEDOT:PSS HTL as well as to minimizing the shunt. Such ultrathin GO layer does not adversely affect the device energy balance and Ohmic transport of the holes to the electrode is preserved, resulting in a reasonable PCE of 2.6%. The device lifetime was as measured by $t_{PCE,50}$ was increased fivefold when the AgNW-based back electrodes is protected with GO on both sides in a sandwich-like structure.

Chapter 4

Conformally Coated AgNW Networks by Nanosized GO and RGO

4.1 Introduction

In the previous chapter, a method of fabricating a long-term stable TE incorporating GO and AgNW was presented. Despite the abundance of studies along with results shown in the previous chapter that show the ability of GO/RGO in improving the long-term chemical stability of MNWs, enhancing their all-round stability including thermal and electrothermal stability is a direction that has been largely unexplored. This likely has to do with the fact that most GO/RGO coatings that have been explored are not conformally coating the MNW networks, unlike metal oxide coatings achieved through sputtering or ALD. As-obtained GO has a wide distribution of lateral flake sizes, mainly consisting of microns-wide layers. [95] When deposited on MNW networks, such large-sized layers cannot conformally cover the surface of the wires, which are typically on the order of less than 100 nm in diameter. This results in only partial protection of the MNW surface, where the uncovered surfaces of MNWs may still be susceptible to surface atomic diffusion, leading to spheroidization under elevated temperatures. In addition to the lack of control over the conformality of GO/RGO overcoating, a general understanding of the relationship between its structure and its protective capabilities is still lacking despite the abundance of previous

studies that use GO/RGO in MNW-based transparent electrodes.

In this chapter, I present an all-solution-based process towards achieving a conformally coated AgNW network by size-reduced RGO. To achieve conformality, I tailored the lateral size of our starting GO material by probe ultrasonication in order to simultaneously decrease their size down to orders of ∼100 nm diameter and homogenize the size distribution. To encapsulate AgNW networks with the downsized nanoscale-GO (nGO), I implemented a layer-by-layer (LbL) approach to controllably tune the coating thickness on AgNWs and perform a post-treatment on the obtained composite film with a $NaBH_4$ solution resulting in a chemically reduced R(nGO)/AgNW TE. This process is entirely solution-based, does not require any specialized equipment, and can be performed on both rigid and flexible substrates with arbitrary shapes and sizes. The resulting transparent electrode conformally encapsulated by R(nGO) has excellent optoelectronic properties, combined with enhanced thermal, electrothermal, chemical, and mechanical stability. Overall, the newly developed process enables a facile and industrially viable solution towards enhancing the operational stability of metal nanowire networks when used in various applications.

4.2 Overview of the fabrication process

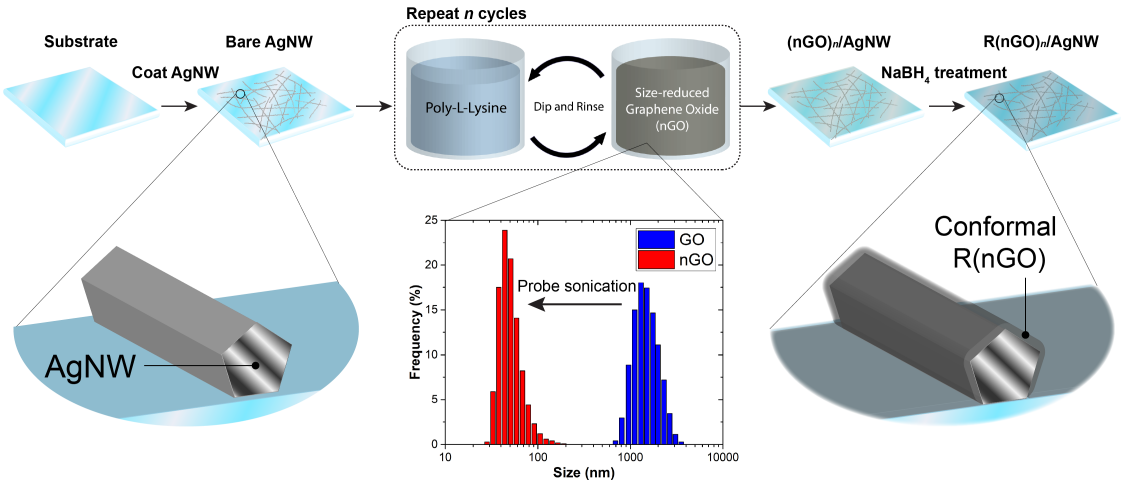

Figure 4-1: Schematic illustrating the fabrication process of $R(nGO)_n$/AgNW.

Figure 4-1 illustrates our all-solution process where the general GO coating step

is as follows. After the cleaning step, the glass or polyethylene terephthalate (PET) substrate was incubated in a poly-L-lysine (PLL) solution to provide an overall positive charge to the substrate, followed by AgNW spin coating. [25] The use of the polycation PLL is necessary for the sequential layering of GO, as GO layers are negatively charged in solution, indicated by our zeta potential measurement (-39 mV at pH = 4). Then the AgNW-coated substrate was immersed in GO solution. The sample was then taken out and rinsed with de-ionized water and blow-dried with nitrogen, leaving a mostly monolayer of GO coating the entire sample. This alternating step of PLL incubation and GO immersion can be repeated n times to obtain a GO overcoating with the desired thickness (GO_n/AgNW). In our study, we have used n = 1∼3, but more coating cycles can be performed if desired. This coating process is essentially a layer-by-layer (LbL) deposition, with many variations having been explored in previous works. [53, 89, 150] After the coating step, the entire composite film was immersed in $NaBH_4$ aqueous solution to chemically reduce the GO film, resulting in R$(GO)_n$/AgNW.

Unique to our process is the size-tuning of GO, where we have reduced the flake size of the GO sheets using probe ultrasonication in order to achieve a more conformal encapsulation around the nanowires. The plot and inset in Figure 4-1 show the size distribution of GO flakes probe sonicated continuously for 2 hours, as measured by dynamic light scattering (DLS). Before sonication, as-received GO has an DLS average size of ∼1600 nm with a wide standard deviation of 490 nm. After 2 hours of sonication, the DLS average size of GO is significantly reduced to ∼52 nm with a standard deviation of 18 nm, which we name nGO. Figure 4-1 shows the average square equivalent size of GO as a function of sonication time measured by atomic force microscopy (AFM). In line with previous studies, [151, 152] the average lateral size undergoes a rapid reduction in the first 30 minutes along with narrowing of the size distribution, with nGO average size of ∼100 nm. AFM-derived size of nGO is larger than DLS-derived size, due to the fact that DLS provides the equivalent hydrodynamic diameter rather than direct, physical measurement that AFM provides. [152] Similar to pre-sonicated GO, nGO is also negatively charged (-35 mV at pH = 4)

and compatible with our LbL coating scheme. Using nGO solution in our process as described above, we have obtained nGO_n/AgNW and $R(nGO)_n$/AgNW. Figure 4-3a and b are representative images of $R(nGO)_3$/AgNW deposited on a 2.54 cm by 2.54 cm glass and a larger 5 cm by 5 cm PET substrate, respectively, and demonstrate the versatility and scalability of our coating process. The coating process can be carried out on a larger substrate (Figure 4-3c) as long as the size is compatible with the liquid vessel used to hold the GO and PLL solution and may be extended to an industrially relevant roll-to-roll process. [153] The complete details regarding sample preparation and characterization are presented in Appendix B.

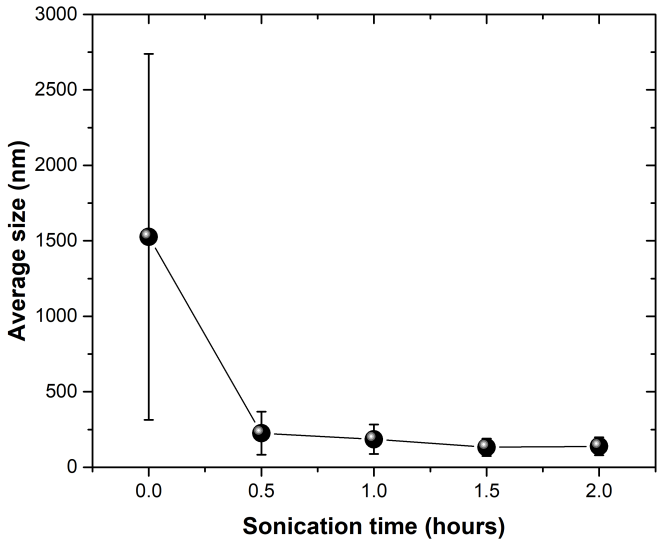

Figure 4-2: Size change of GO with sonication time measured by Atomic Force Microscopy (AFM)

4.3 Structural Characterization

The effectiveness of a protective coating layer is directly related to its structural and physicochemical characteristics. Therefore, we have characterized the film thickness, chemical properties, and the degree of conformality of the $R(nGO)_n$ film. The thickness variation of $R(GO)_n$ and $R(nGO)_n$ films as a function of coating cycle n measured with AFM demonstrates the controllability of our process. From Figure 4-4a, it can be observed that the thickness of nGO and, in turn, R(nGO) increases in a linear

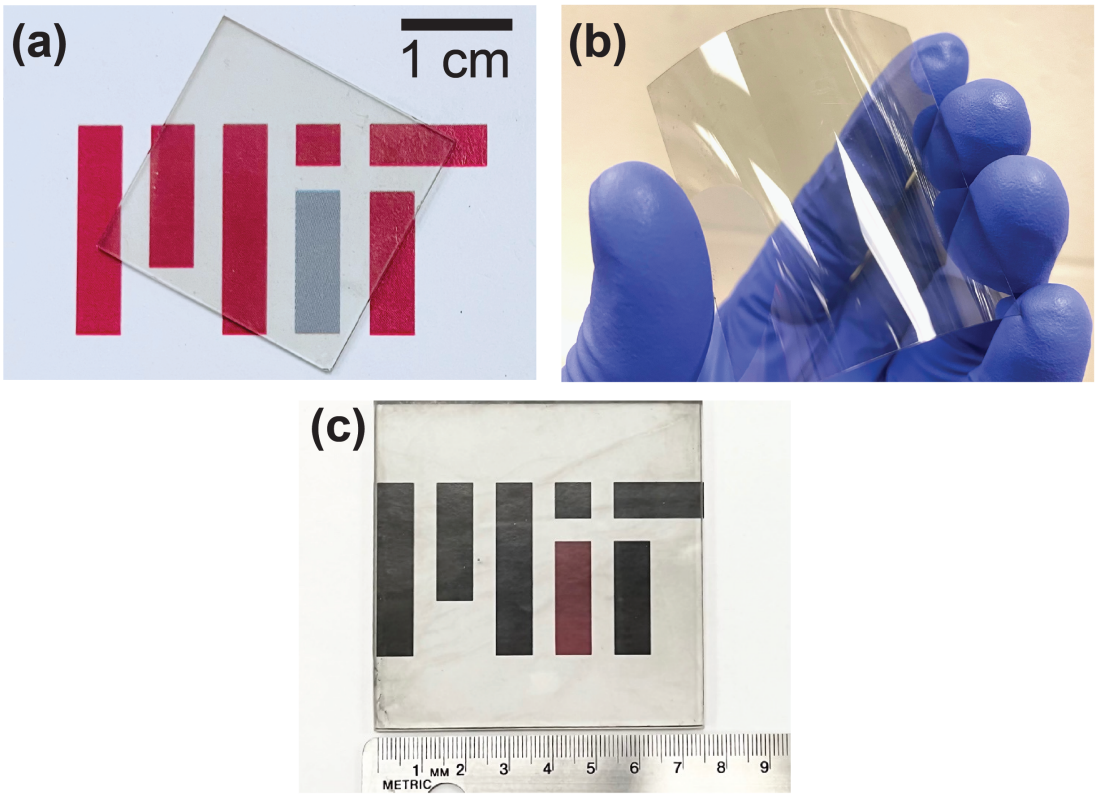

Figure 4-3: Representative image of R(nGO)$_3$/AgNW fabricated on a (a) 2.5 cm by 2.5 cm glass, (b) PET substrate, and (c) on a 7.5 cm by 7.5 cm glass substrate

manner with n up to 3, consistent with other studies that employ an LbL-type coating scheme. [53] Regular-sized GO and RGO were observed to follow a similar trend (Figure 4-4b). The smaller thickness of R(nGO)$_n$ films compared to (nGO)n films is due to the loss of functional groups, and water molecules present between GO layers upon chemical reduction by $NaBH_4$, leading to reduced interlayer spacing. [154]

X-ray Diffraction (XRD) results (Figure 4-5a) indeed suggest a reduced interlayer spacing of R(nGO). The calculated interlayer spacing was 1.02 nm for nGO films and 0.39 nm for R(nGO). Similar values were observed for GO and R(GO) samples as well (Figure Figure 4-5c). It should be noted that the interlayer spacing of our GO film was slightly larger than that of vacuum filtered GO films (∼0.88 nm) [95], but this is expected since our films are composed of bilayers of GO sheets and PLL. The effect of chemical reduction by $NaBH_4$ was also probed by X-ray photoelectron spectroscopy (XPS) results (Figure 4-5b,d) which show the successful removal of oxygenated func-

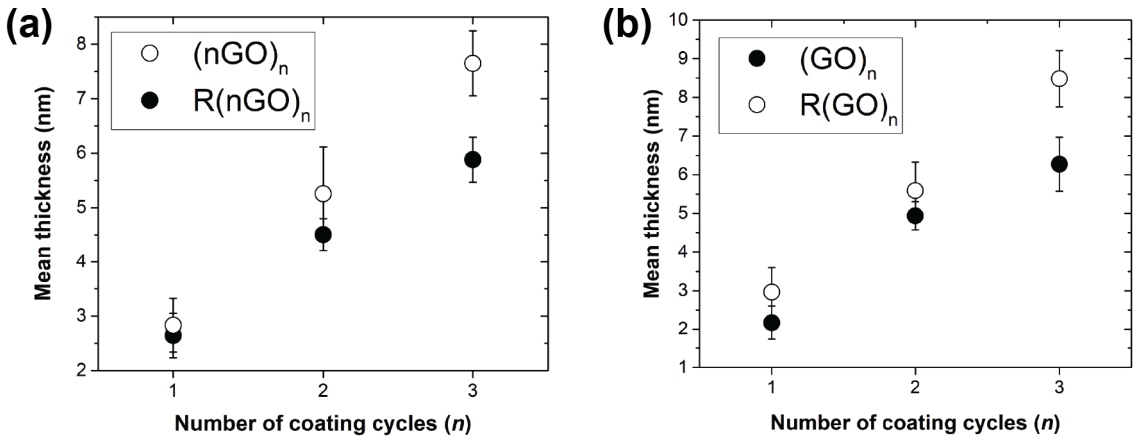

Figure 4-4: (a) Variation of nGO and R(nGO) thickness according to the number of coating cycles performed. (b) Variation of GO and R(GO) thickness according to the number of coating cycles performed.

tional groups. For R(nGO), the peak areas of C-O and C=O groups are dramatically reduced relative to C-C/C=C peaks, showing the successful removal of oxygenated functionalities at the edge and basal planes of the GO sheet. Thermogravimetric analysis (TGA) also indicates a difference between the unreduced and reduced GO, where the weight loss experienced by the former is due to loss of moisture and oxygen functionalities (Figure 4-5e). These results explain the reduced interlayer spacing and suggest modification of surface chemistry and hydrophilicity, which heavily influences the stability of underlying AgNWs, as will be described in subsequent sections.

To examine the microstructure of our film and assess the degree of conformality around the AgNWs, we performed SEM on R(GO)/AgNW and R(nGO)/AgNW. Figure 4-6a-d shows the cross-section and tilted-angle SEM images of R(GO)/AgNW and R(nGO)/AgNW. It should be mentioned that while only one coating cycle was used for tilted-angle imaging, three coating cycles were necessary for cross-section imaging due to the ultrathin nature of R(GO) and R(nGO) sheets. The flakes are seen to uniformly cover the entire area for both R(GO) and R(nGO), but a significant difference in conformality is apparent when examining the cross-section. In Figure 4-6a, the R(GO) is in contact with only the two top faces of the pentagon-shaped AgNW, while in Figure 4-6c, R(nGO) is seen to cover all four faces of the AgNW except for the face in contact with the substrate. The difference in conformality is also seen

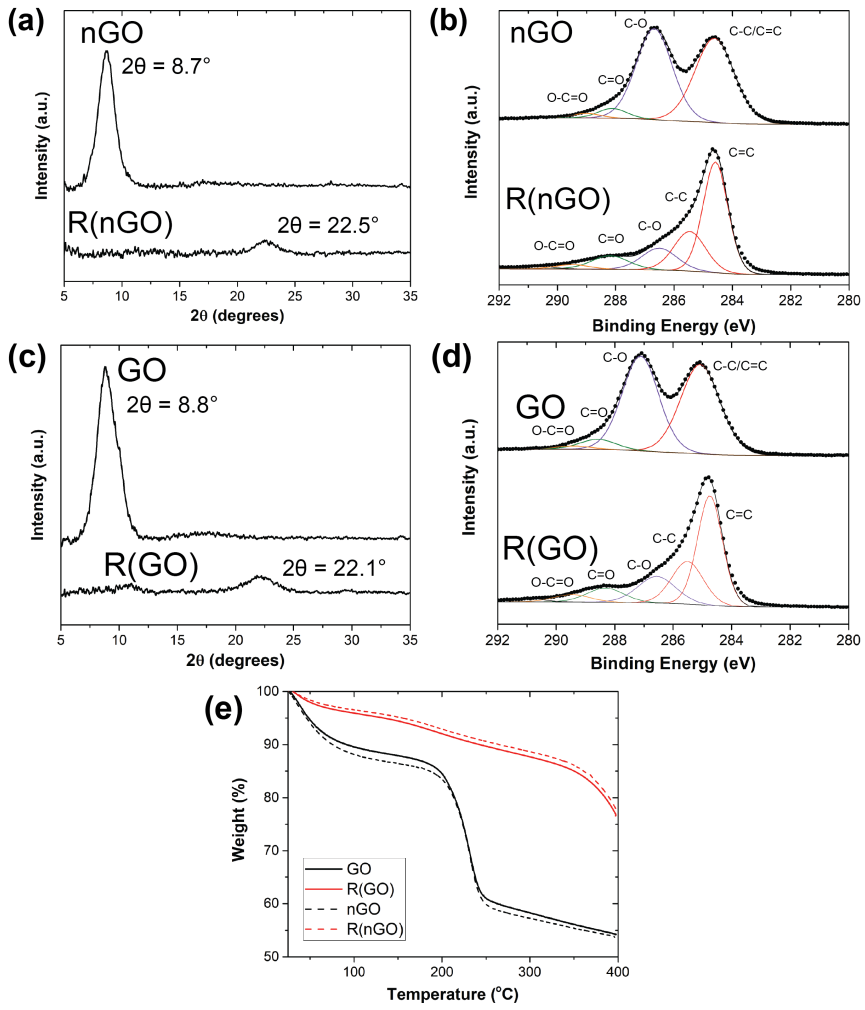

Figure 4-5: (a) X-ray diffraction (XRD) spectra and (b) C 1s X-ray photoelectron spectroscopy (XPS) scan of nGO and R(nGO) films. (c) and (d) are respective results for GO and R(GO) films. (e) Thermogravimetric analysis (TGA) of GO and RGO performed in air (6°C/min)

in the tilted-angle images (Figure 4-6b, d), particularly near AgNW junctions where R(GO) is seen to be hanging without directly contacting the substrate or the AgNW, in contrast to R(nGO). It should be noted that the difference in conformality is caused primarily by differences between coating GO versus nGO before performing the chemical reduction, judging from similar conformality difference between GO/AgNW and nGO/AgNW. While monolayer GO is intrinsically flexible enough to bend around the AgNW facet, [155] its large size compared to the circumference of the AgNW (∼300 nm) causes significant interaction with the substrate surface during its deposition

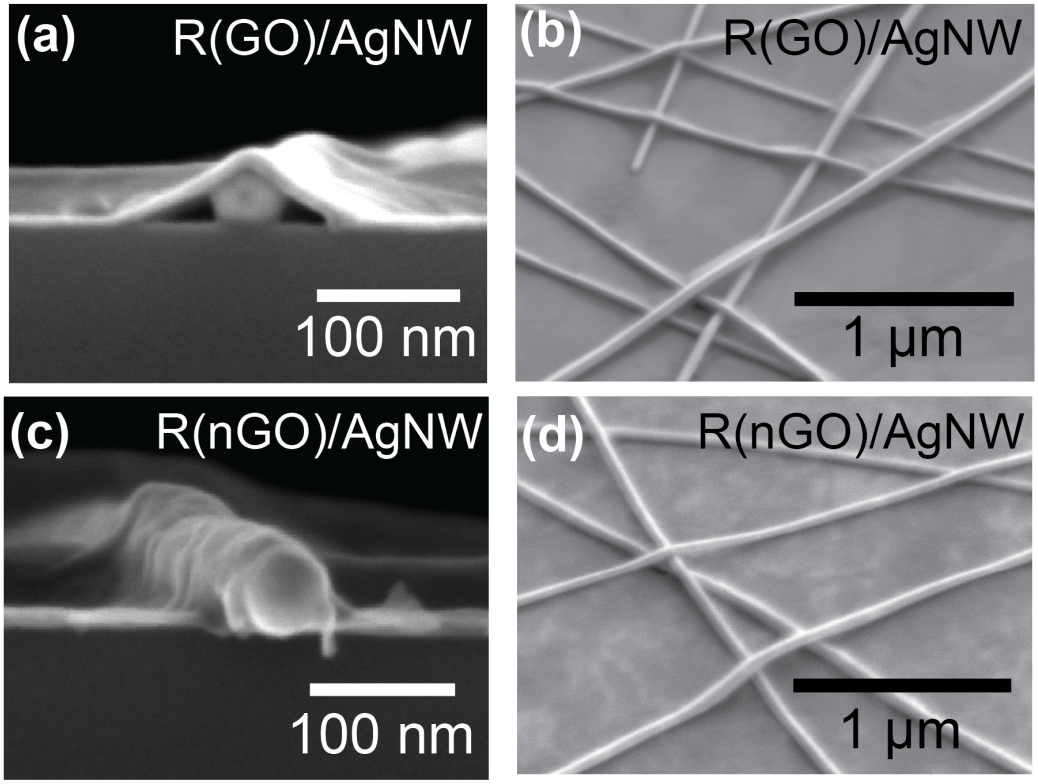

Figure 4-6: SEM cross-section and tilted-angle images of (a, b) R(GO)/AgNW and (c, d) R(nGO)/AgNW films.

that effectively 'pins' the GO sheet, preventing it from completely wrapping around the AgNW. In contrast, the improved conformality of nGO is attributed to the fact that its size is below the circumference of the AgNWs and is small enough to cover the sides of the nanowires without being pinned on the substrate.

4.4 Electrical and Optical Properties

The optoelectronic performances of R(nGO)$_n$/AgNW and R(GO)$_n$/AgNW as transparent electrodes were characterized by UV-vis spectroscopy and 4-point probe (4PP) measurements. Figure 4-7a shows the total transmittance spectra of our films in the wavelength range of 300-800 nm along with that of bare, uncoated AgNWs. For all measurements, the contribution from the underlying glass substrate is removed, and the areal mass density of the AgNW was kept the same for all samples. It can be

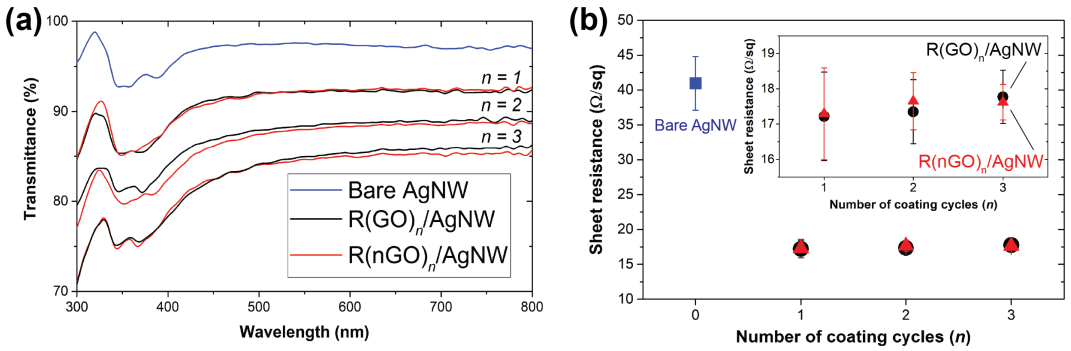

Figure 4-7: (a) UV-vis spectra and (b) Sheet resistance measurements of bare AgNW, R(GO)$_n$/AgNW, and R(nGO)$_n$/AgNW films. Inset of (b) shows a magnified view of the same plot.

seen that the transparency of the film decreases with the increasing number of coating cycles, in agreement with increasing thickness of the RGO or R(nGO) with cycle number n. Furthermore, the transmittance spectra did not depend on whether RGO or R(nGO) was being used. The bare AgNW network has a transmittance of 97.6% at 550 nm, and after coating cycle number $n = 1$, decreases to 92.2% transmittance. Subsequent coating cycles result in approximately 88.4% and 85% transmittance at 550 nm for $n = 2$ and $n = 3$, respectively. We note here that such loss in transmittance loss is compensated by the significant gain in stability, as will be discussed in subsequent sections.

Figure 4-7b shows the mean sheet resistances and their standard deviations of our samples measured by the 4PP method on five different locations within the 2.5 cm by 2.5 cm sample. Uncoated bare nanowires had a sheet resistance of 41 Ω/sq with a standard deviation of 3.9 Ω/sq. This relatively high resistance and variation within the sample is typical of as-prepared MNW-based transparent electrodes, due to the high nanowire-to-nanowire junction resistance. [27] In our R(GO)$_n$/AgNW and R(nGO)$_n$/AgNW samples, a significantly reduced sheet resistance of around 17.5 Ω/sq was observed for all n, and the variation within the sample was also significantly reduced compared to bare AgNWs (standard deviation reduced to ∼1 Ω/sq). This is a ∼57% reduction in sheet resistance and 74% reduction in its standard deviation. These improvements can be explained by the tight binding of the AgNW junctions

to lower their contact resistance thanks to the RGO or RnGO overcoating. [85] It should be noted that thicker RGO or RnGO did not have a meaningful effect on the sheet resistance, possibly due to the fact that our RGO/RnGO shows very high resistance (∼100 kΩ/sq) compared to AgNWs so that co-percolation effects [156] between RGO/RnGO and AgNW can be ignored. This means sheet resistance is primarily governed by the areal mass density of AgNWs in our materials. Nevertheless, increasing the number of coating cycles did result in a slight improvement in reducing the sheet resistance variation within the sample. For instance, the standard deviation decreased from 1.3 Ω/sq for $R(nGO)_1$/AgNW to 0.5 Ω/sq for $R(nGO)_3$/AgNW. The favorable role of fully solution-processed RGO or RnGO coating in improving the sheet resistance of AgNW networks holds technological significance as high temperature annealing typically required to lower the nanowire junction contact resistance is not compatible with flexible plastic substrates.

4.5 Stability Characterizations

4.5.1 Thermal Stability

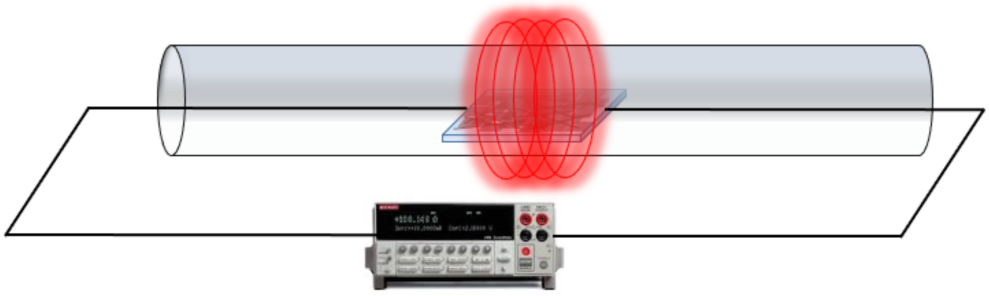

Figure 4-8: Schematic of the *in situ* thermal ramp test setup

In order to assess the thermal stability of AgNW coated by n layers of GO, nGO, RGO, and R(nGO) we employed an *in-situ* thermal ramp technique as described in Figure 4-8, in which the conductive film is placed in a quartz tube furnace, and the resistance is measured simultaneously as the temperature is linearly ramped up from room temperature at a fixed rate of 6°C/min. During heating, the current is supplied

at a minimum level to measure the resistance in order to prevent Joule heating and purely examine the thermal stability of the material being examined. In order to quantitatively assess irreversible degradation, we define the degradation parameter ν as:

$$\nu = \frac{R}{R_0} - (1 + \beta \Delta T) \tag{4.1}$$

where R is the resistance at a given temperature T, R_0 is the initial resistance, $\beta = 3.8 \times 10^{-3}\ K^{-1}$ is the temperature coefficient of resistivity for bulk Ag, and $\Delta T = T - T_0$ where T_0 is the initial temperature. While lower β values have been reported for AgNWs, [157] the bulk value was still used for simplicity since it has little quantifiable impact close to the point of failure where R/R_0 diverges. Therefore, ν expresses the normalized resistance while taking into account the resistance increases with temperature for metals, and $\nu > 0$ corresponds to an irreversible increase in film resistance due to thermally-induced degradation.

Figure 4-9a-b shows thermal ramp curves for Bare AgNW, GO_n/AgNW, and $(nGO)_n$/AgNW. Bare AgNW networks start to undergo irreversible degradation from 160°C, where a rapid increase in ν is observed. The measurements indicate that for GO coating, increasing the thickness from $n = 1$ to 5 did not result in a meaningful delay in failure temperature compared to Bare AgNWs. For nGO coating, increasing the thickness of the coating resulted in a delayed failure behavior (smaller rate of increase in ν), where more delay was observed for thicker coatings. Nevertheless, the onset of degradation described by the point at which ν begins to increase above 0 is not modified. This means that the kinetics of AgNW surface diffusion that leads to fragmentation is not truly slowed down.

Figure 4-9c shows thermal ramp curves for Bare AgNW and $R(GO)_n$/AgNW. $R(GO)_1$/AgNW show increased thermal stability compared to bare nanowires since degradation starts near 190°C. However, increasing the number of layers of R(GO) does not significantly impact the onset of degradation, although it was observed that the rate of degradation was slowed down when $n = 3$. In contrast, when using nGO

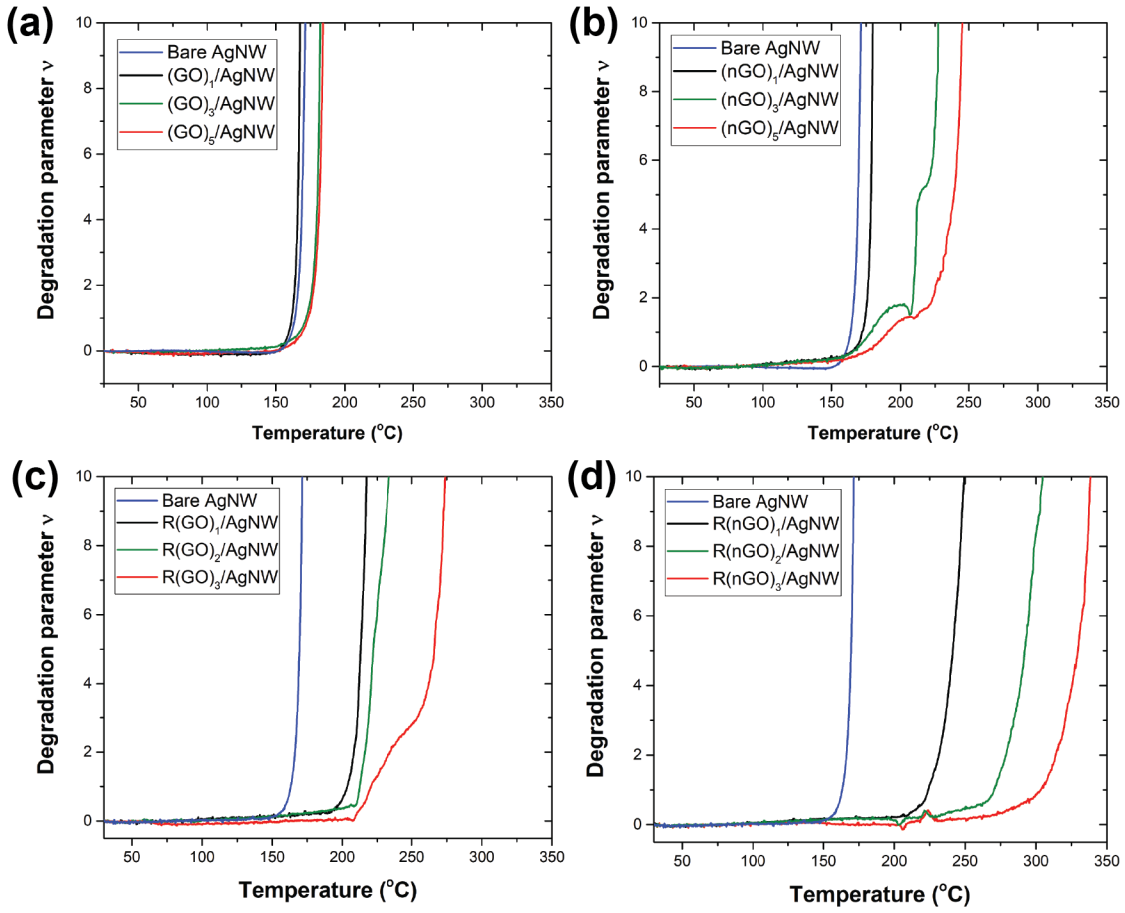

Figure 4-9: Resistance measured *in situ* for (a) $(GO)_n$/AgNW (b) $(nGO)_n$/AgNW (c) R$(GO)_n$/AgNW and (d) R$(nGO)_n$/AgNW during a thermal ramp of 6°C/min.

to form a conformally coated R$(nGO)_n$/AgNW, delay of the degradation onset temperature was observed with increasing coating layers. Figure 4-9d shows that for n = 1, the degradation onset occurs near 200°C, similar to R(GO)-capped samples. However, for n = 2 and 3, the degradation onset occurs at increased temperatures. Figure 4-10 plots the mean degradation temperatures and standard deviations for five samples of each coating type under thermal ramp and clearly shows the impact of R(nGO) coating on improving the thermal stability of AgNWs. For convenience, we have defined the degradation temperature to be the temperature at which $\nu = 2$. As can be seen, the degradation temperature increases at a greater slope with increasing R(nGO) coating thickness than for R(GO), indicating that the conformally coated R(nGO) has a more significant effect of protecting the wires. The most thermally

stable sample was R(nGO)$_3$/AgNW with a degradation temperature of 300°C, indicating an enhancement of the thermal limit by ∼130°C compared to untreated bare AgNWs. In summary, our thermal ramp experiments suggest that a coating that is conformal and thick enough is needed to increase the thermal stability of AgNWs, which is a similar result observed for ALD-deposited metal oxide coatings. [68]

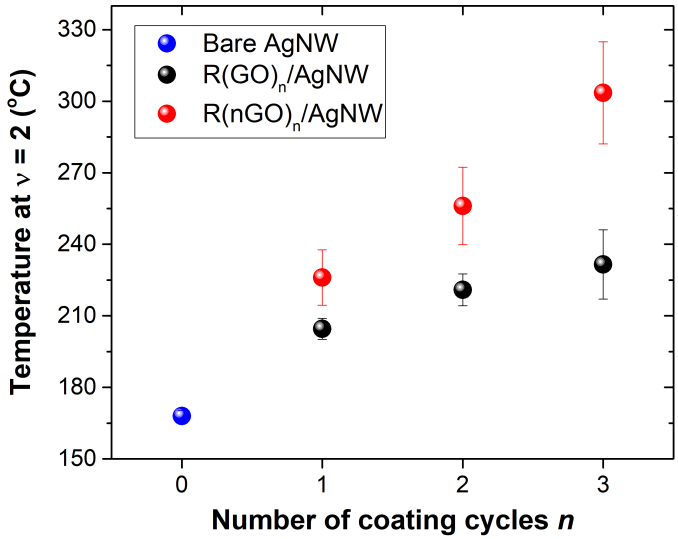

Figure 4-10: Summary of thermal ramp studies where the average temperature at which ν=2 are shown for all samples tested.

To further elucidate how the coating conformality influences thermal stability, we examine the origin of thermal instability in a MNW network. Two types of morphological instabilities must be considered, the first of which is the thermal instability of individual MNW segments. This instability results from their tendency to evolve into discontinuous rows of spheres under high temperature, known as Rayleigh-Plateau instability. [49] The thermodynamic driving force of such spheroidization is the minimization of total surface energy, while the kinetics of the morphological transition is primarily governed by the NW surface atomic diffusion, which must be delayed to increase the temperature at which spheroidization occurs. The second type of morphological instability in a MNW network occurs due to Capillarity-induced surface diffusion [158] at the MNW junction where two or more wires form a physical contact. The surface atomic flux J_s in this case is given as

$$J_s = -\frac{D_s(T)\gamma\Omega^{2/3}}{k_B T}\nabla_s\kappa \tag{4.2}$$

where $D_s(T)$ is the temperature-dependent surface diffusion coefficient, γ is the surface tension, Ω is the atomic volume, k_B is Boltzmann constant, T is temperature, and $\nabla_s\kappa$ is surface curvature gradient. Thus, the negative surface curvature at the contact point between wires drives atomic surface diffusion towards the junction, which first fuses and eventually spheroidize to disconnect from the wire segments. It is important to note that for networks of NWs, the morphology evolution and disconnection at the interwire junction occurs at lower temperatures than the spheroidization of single wire segments, as has been shown by recent Kinetic Monte Carlo (KMC) [159] and phase-field models of NW junctions. [160] Therefore, the key to preserving the NW network resistance upon heating is to delay surface diffusion at the junction through conformal encapsulation. Since it has been shown in previous studies that graphene in conformal contact with a metal surface suppresses morphological evolution by lowering $D_s(T)$, [161] a similar effect is expected to take place with a conformal RGO coating on AgNWs.

In this regard, the superior thermal stability demonstrated by R(nGO)/AgNW samples is explained by evaluating coating conformality at the NW junction. Figures 4-11a-b show AFM images of R(GO) and R(nGO)-covered AgNW samples at a two-wire junction, where the dashed lines correspond to where the topography profiles were taken. The corresponding profiles are shown in Figure 4-11c, which clearly indicates the junction is much more conformally covered for the R(nGO)/AgNW, evident from the less steep topography of R(GO)/AgNW. This is due to the fact that larger R(GO) sheets are hanging across the substrate surface and the top of the NW junction, leaving much of the side surfaces of the AgNWs near the junction uncovered. This will lead to a relatively unhindered surface atomic diffusion and earlier fragmentation occurring at the junction for R(GO)/AgNW. Figure 4-12a-b shows SEM images of $R(GO)_3$/AgNW and $R(nGO)_3$/AgNW samples taken out at 300°C during a thermal ramp and clearly exhibits a difference in terms of AgNW

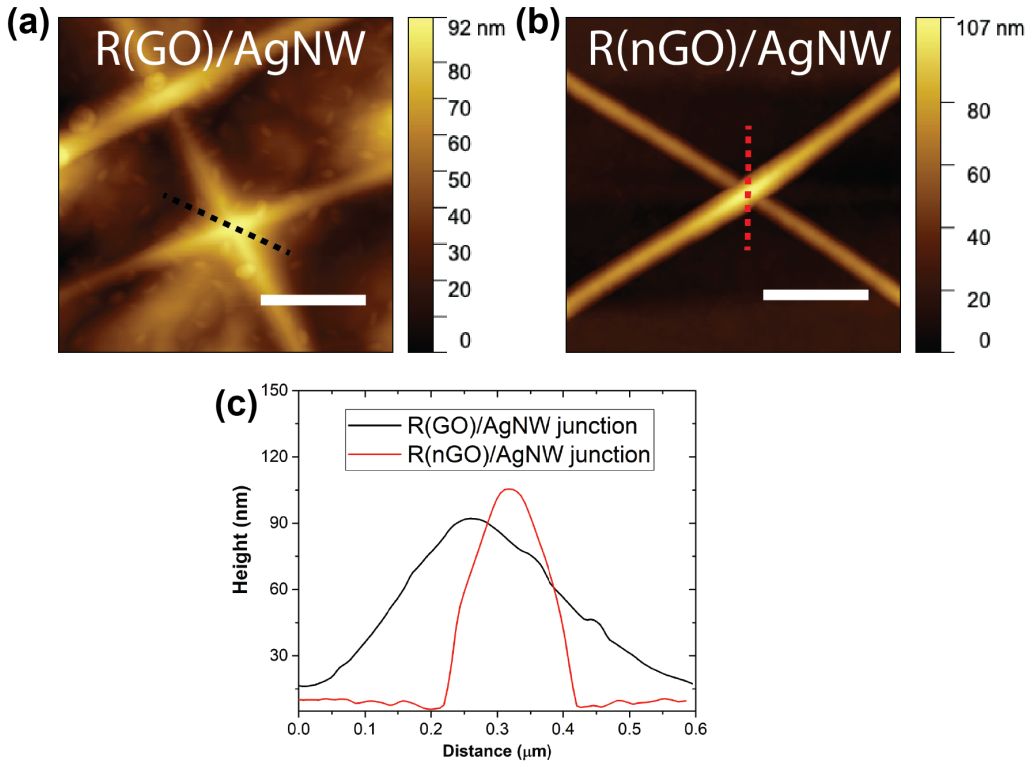

Figure 4-11: AFM images taken on a AgNW junction for (a) R(GO)/AgNW and (b) R(nGO)/AgNW sample. (c) Height profiles along the dashed lines.

morphology. For $R(GO)_3$/AgNW, nearly all NW junctions have disconnected due to the agglomeration of Ag at the junction. In contrast, the extent of morphological evolution appears significantly less pronounced for $R(nGO)_3$/AgNW, although some junction disconnections are observed. This is direct evidence that demonstrates the superior ability of R(nGO) in enhancing the thermal stability of the underlying AgNW network through conformal encapsulation.

4.5.2 Electrothermal Stability and Transparent Heater Application

The electrothermal stability of an AgNW-based transparent electrode is another crucial measure of its overall robustness, particularly for transparent heater applications where DC voltage is applied across the terminal to induce Joule heating. [162] One of the most straightforward methods to gauge the electrothermal stability of a AgNW

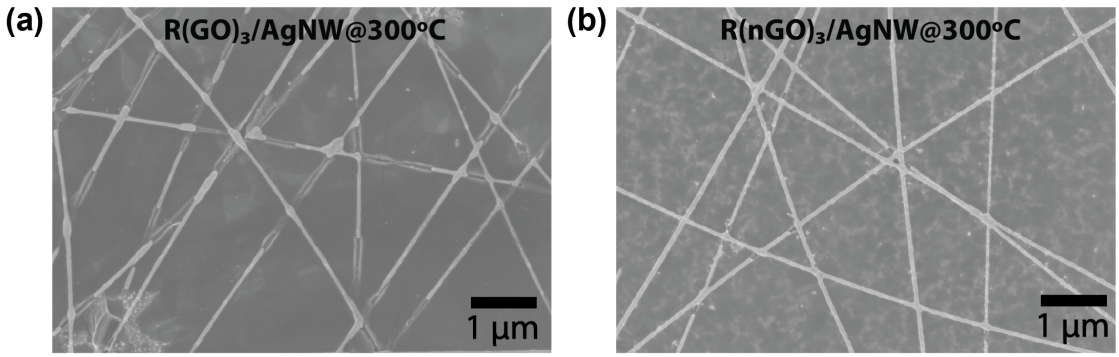

Figure 4-12: SEM images of (a) $R(GO)_3$/AgNW and (b) $R(nGO)_3$/AgNW taken out at 300°C during a thermal ramp.

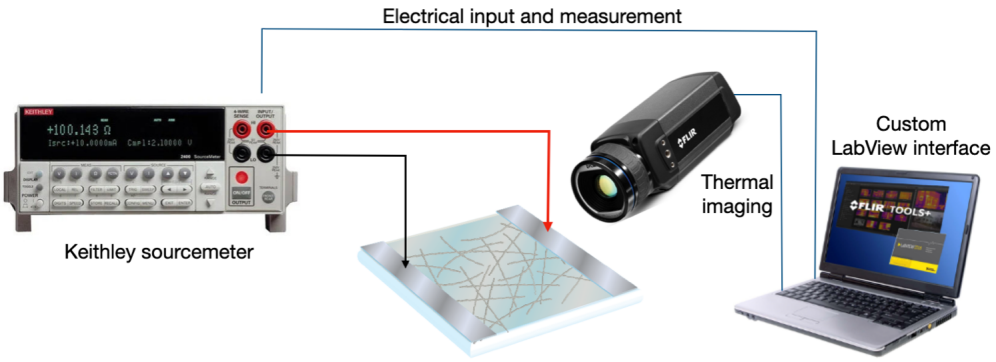

Figure 4-13: Schematic of a *in situ* voltage ramp/plateau test setup

network is to subject it to a linear voltage ramp until irreversible damage occurs. Previous studies have employed *in situ* monitoring of the resistance change and heat profile dynamics of the AgNW network under a linear voltage ramp. [45, 51, 69] In a typical setup, a sourcemeter unit is used to collect the resistance (current) values simultaneously with voltage application, and an infrared camera is used to capture the temperature profile in real-time (Figure 4-13). We have used the same technique to $R(nGO)_n$/AgNW and $R(GO)_n$/AgNW films using a linear voltage ramp rate of 1V/min.

Figure 4-14a shows the result of the voltage ramp experiment where the change in resistance is plotted as a function of increasing voltage, and Figure 4-14b shows the corresponding maximum temperature of the sample tracked with an IR camera. For bare AgNWs, the resistance is seen to increase steadily with increasing temperature

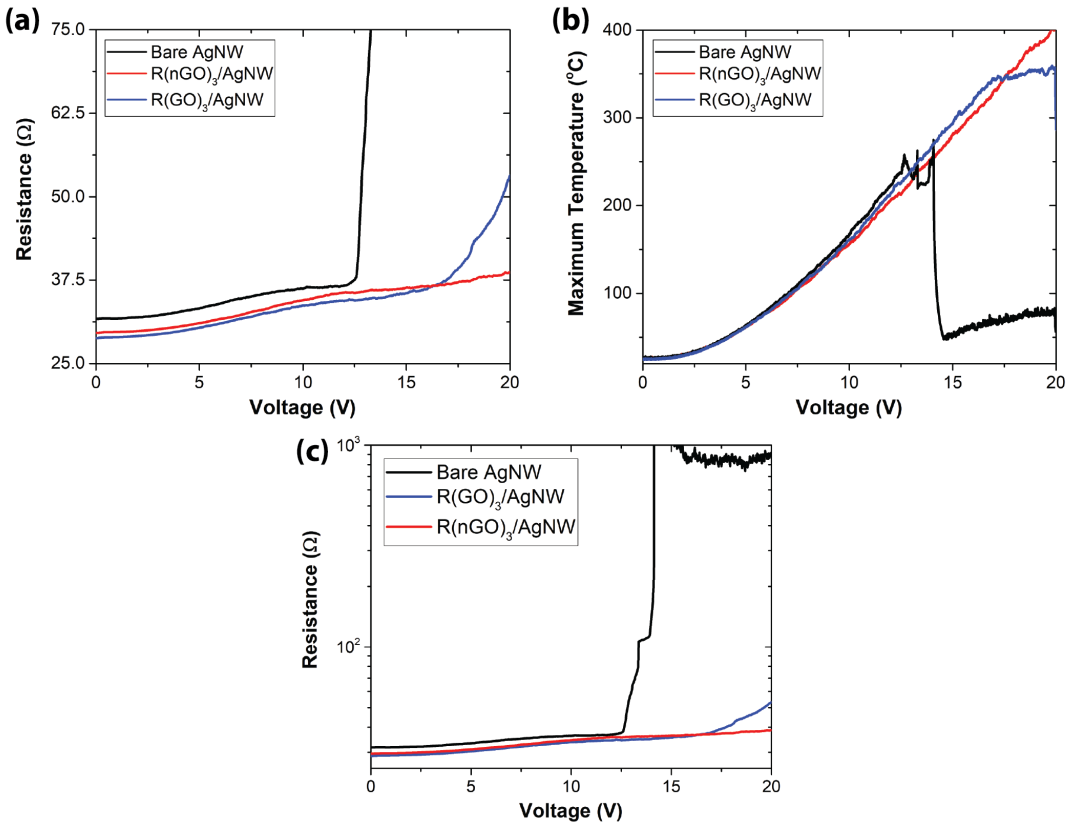

Figure 4-14: (a) Resistance and (b) maximum temperature measured in situ for bare AgNWs, $R(GO)_3$/AgNW and $R(nGO)_3$/AgNW during a linear voltage ramp of 1V/min. (c) Log-scale figure of voltage ramp shown in (a) showing kΩ divergence

until 10V, then encounters a plateau until 12.5V, followed by a rapid divergence to the >kΩ range (Figure 4-14c). This resistance divergence is also apparent from an abrupt reduction in Joule heating due to the network no longer being able to sustain a current load (Figure 4-14b). A resistance plateau during a voltage ramp can be attributed to NW junction sintering occurring due to Joule heating and a reduction in the 'true' network resistance. The occurrence of resistance divergence at even higher voltages can be explained by the initiation of hot spots induced by Joule heating, followed by the propagation of the hot spots in the direction orthogonal to the current flow direction, consistent with a previous study. [51] The propagation of a hot spot leaves behind a trail of spheroidized or disconnected NWs unable to carry current. This 'crack' composed of spheroidized NWs that acts as an insulating region within the NW network causes the measured resistance to diverge. Therefore, it is apparent

that localized hot spots that form during intense Joule heating cause disconnection and eventual spheroidization of AgNWs due to thermal instability modes identical to those discussed in the previous section.

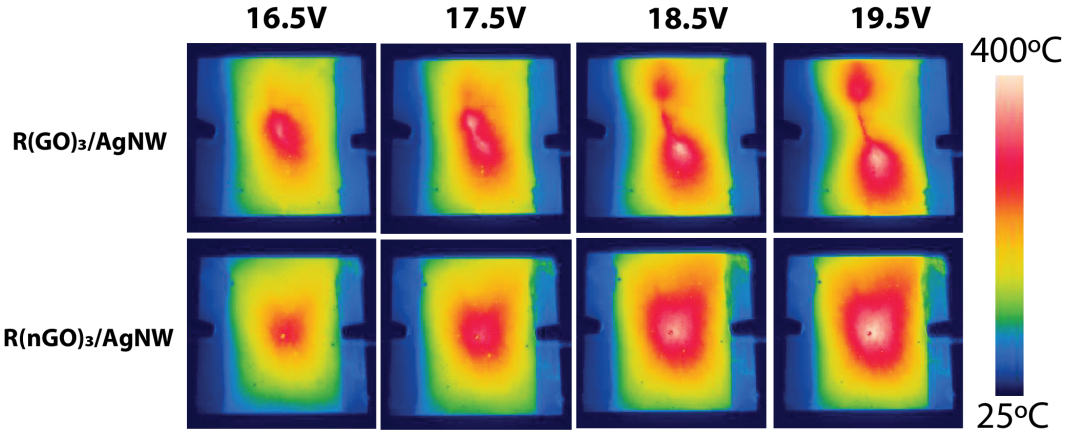

Figure 4-15: Temperature profiles taken with an infrared camera during a linear voltage ramp of 1V/min

Contrary to bare AgNWs, divergence of resistance is avoided for $R(GO)_3$/AgNW and $R(nGO)_3$/AgNW (Figure 4-14a). However, $R(GO)_3$/AgNW undergoes an irreversible degradation above 16V, while such degradation was not observed for $R(nGO)_3$ coated AgNW even at 20V, which was the voltage limit of our sourcemeter. The difference between the two samples can also be seen in Figure 4-14b, where the slope of increasing maximum temperature with voltage for $R(GO)_3$/AgNW is reduced above 16V, unlike for $R(nGO)_3$/AgNW. Furthermore, infrared snapshots taken for the two samples at different voltages during linear ramp clearly shows the differences between the two samples (Figure 4-15). A hotspot propagates across the sample forming a 'crack' in the AgNW network for $R(GO)_3$/AgNW while $R(nGO)_3$/AgNW remains intact. Similar to the thermal ramp results (Figure 4-9c, d), we note a thickness dependence on the observed electrothermal stability. Figure 4-16a-d shows the voltage ramp results for thinner RGO and R(nGO) coated AgNWs where $n = 1$ and 2, which shows that the onset of failure occurs at a reduced voltage than for $n = 3$, but in all cases, R(nGO) coated AgNWs experienced a delayed failure compared to R(GO) samples. The observed electrothermal stability difference between the two samples

with the same thickness is attributed to the improved thermal stability of more conformally encapsulated R(nGO)$_n$/AgNW samples, as discussed in the previous section. That is, conformally wrapped AgNW junctions are better able to resist morphology evolution and disconnection even under intense Joule heating.

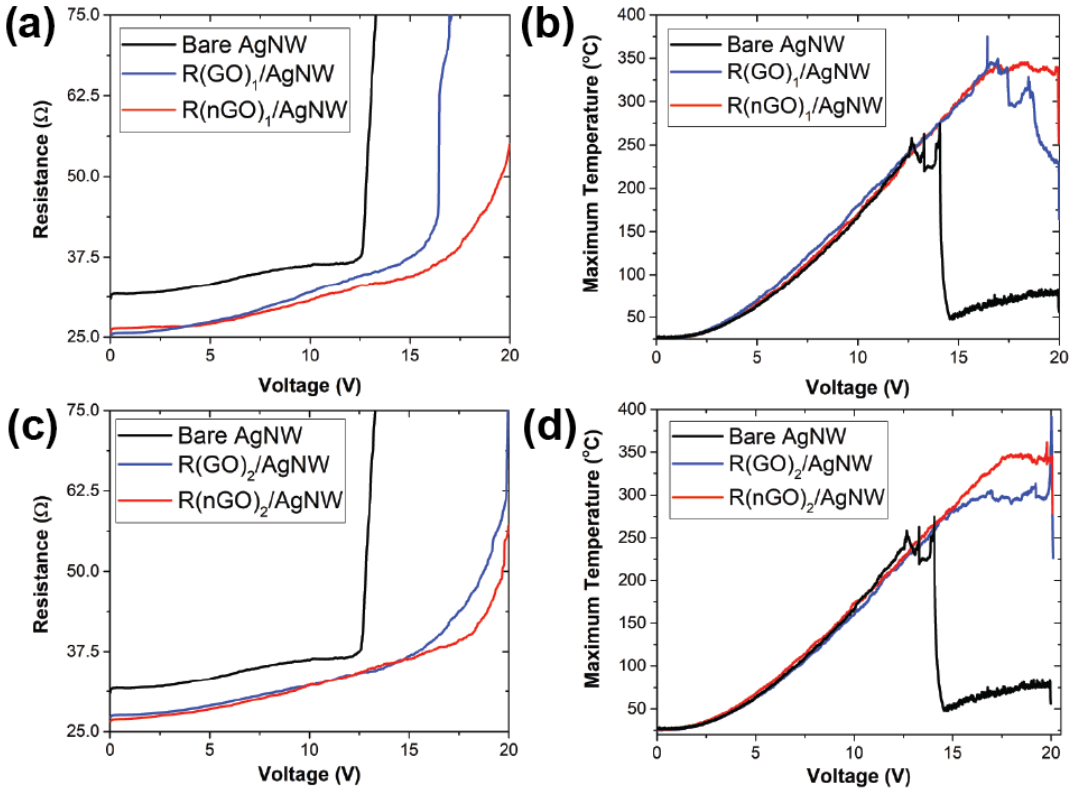

Figure 4-16: *In situ* resistance and maximum temperature evolution during a linear voltage ramp of 1V/min for (a), (b) $n = 1$ and (c), (d) $n = 2$

The superior electrothermal stability of R(nGO)$_3$/AgNW is directly related to the operational stability when used as transparent film heaters. This was made evident through the voltage plateau experiments, where the results are shown in Figure 4-17a. The samples were subject to constant voltage plateaus at 2 V, 5 V, 8 V, 11 V, and 14 V for 15 minutes each and back down to 2 V following the same sequence in reverse order. It was observed that bare AgNWs' ability to sustain Joule heating was completely lost as soon as 11 V was applied due to failure. At the 14 V plateau, R(GO)$_3$/AgNW does not completely fail, but the temperature decreases by almost 30°C rather than maintaining a steady-state temperature. This indicates an

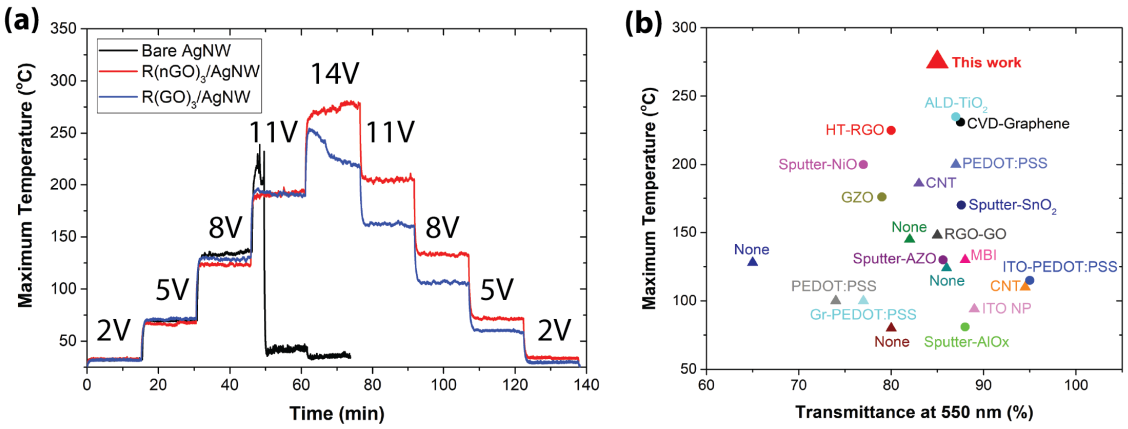

Figure 4-17: (a) Maximum temperature recorded during a voltage plateau experiment where each voltage was applied continuously for 15 minutes each. (b) Comparison of $R(nGO)_3$ with other coatings for AgNWs reported in literature in terms of transparent heater performance. Triangular labels represent coatings attained by an all-solution process at room temperature. All references for the devices shown are listed in Table B.1, Appendix B, along with heater test methods.

irreversible resistance increase and is also apparent from the decreased temperature when descending in voltage plateau compared to when ascending in voltage plateau. On the other hand, $R(nGO)_3$/AgNW is able to sustain constant Joule heating at 14 V corresponding to a steady-state temperature of 275°C, and even undergoes a slight increase in temperature since a reduction in resistance due to AgNW junction sintering has likely occurred. During descending plateaus, the temperature of $R(nGO)_3$/AgNW was higher compared to values at the same voltages measured during ascending plateaus, again due to reduction in the AgNW network resistance. In summary, the superior thermal stability of conformally coated $R(nGO)_3$/AgNW directly translates to its excellent electrothermal (Joule heating) stability. Overall, a higher maximum temperature and increased reliability during continuous heater operation are achieved for R(nGO)-coated AgNWs. A brief literature survey of transparent heaters based on coated AgNW networks (Figure 4-17b) indicates that our $R(nGO)_3$ coated on AgNW demonstrates a superior maximum temperature at the same transmittance compared to other coating types. It is noteworthy that while our coating process is all-solution based and carried out at room temperature, it surpasses heater performance attained by methods such as sputtering, ALD, and CVD.

4.5.3 Chemical Stability

Although it was observed that R(nGO) could provide significantly improved thermal and electrothermal (Joule heating) stability, it should also be able to provide protection against chemical and mechanical degradation to enable a broader application that requires long-term reliability. It is well known that for silver, sulfidation rather than oxidation is the dominating mechanism of long-term atmospheric corrosion and is more commonly known as the underlying cause of silver tarnishing. [42] Sulfidation of AgNW has been attributed to trace sulfur compounds in the atmosphere, such as H_2S and OCS, which react with Ag in the presence of surface-adsorbed water to form Ag_2S nanoparticle-like features. [41, 43] The Ag_2S particles are semiconducting and grow at the expense of Ag, causing the resistivity of AgNW to increase significantly over time. Therefore, a suitable protective barrier for AgNWs should hinder the transport of sulfuric gas species and minimize the adsorption of moisture.

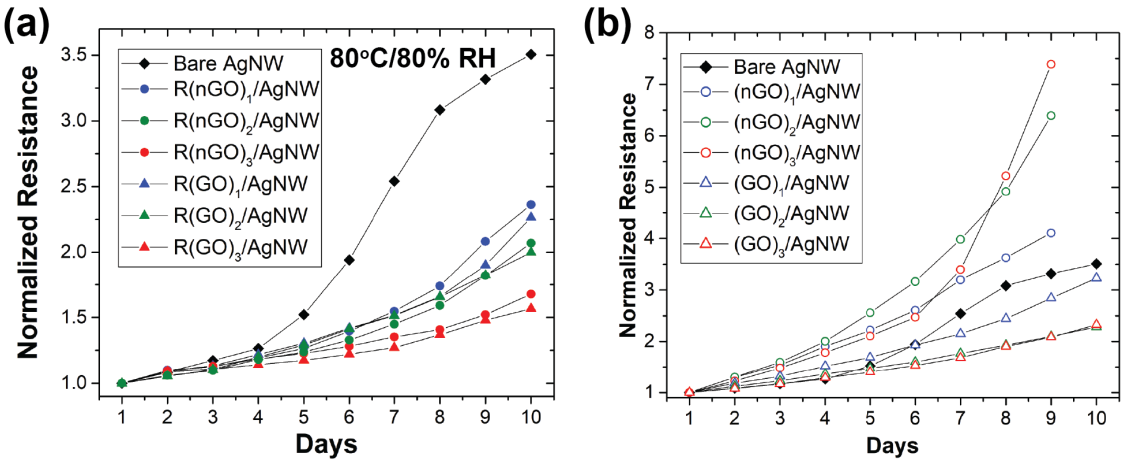

Figure 4-18: Long-term resistance evolution of (a) bare AgNW, $R(GO)_n$/AgNW and $R(nGO)_n$/AgNW and (b) $(GO)_n$/AgNW and $(nGO)_n$/AgNW stored under 80°C and 80% relative humidity.

We have evaluated the chemical resilience of R(GO) and R(nGO)-covered AgNW electrodes by measuring their resistance evolution over a period of 10 days under atmospheric storage in 80% relative humidity and 80°C in order to accelerate the degradation process. Figure 4-18a shows the variation of resistance normalized by their respective initial values. All samples had the same size and the same nanowire

density, and their aging process was carried out simultaneously. Bare AgNWs underwent a resistance increase by 3.5 times within 10 days of storage. In contrast, all of the R(GO)/AgNW and R(nGO)/AgNW samples' resistance change was not as pronounced as bare AgNWs, in agreement with previous reports. [46, 91] For both R(GO) and R(nGO)-based samples, the initial resistance was better preserved with increasing thickness, with final resistance being 1.6 and 1.7 times that of initial values, for $R(GO)_3$/AgNW and $R(nGO)_3$/AgNW, respectively. We have imaged the degraded AgNWs at the end of the 10-day storage, as shown in Figure 4-19. To fully visualize the AgNWs under the coating, we applied a double-sided conductive tape to the sample, then peeled and flipped it upside down to uncover the AgNW surface (Figure 4-19). As the images show, nodular features were evident on bare AgNW surfaces, indicating the formation of Ag_2S. [41] AgNWs that had been covered by $R(GO)_3$ and $R(nGO)_3$ show no such feature, which attests to their excellent barrier properties.

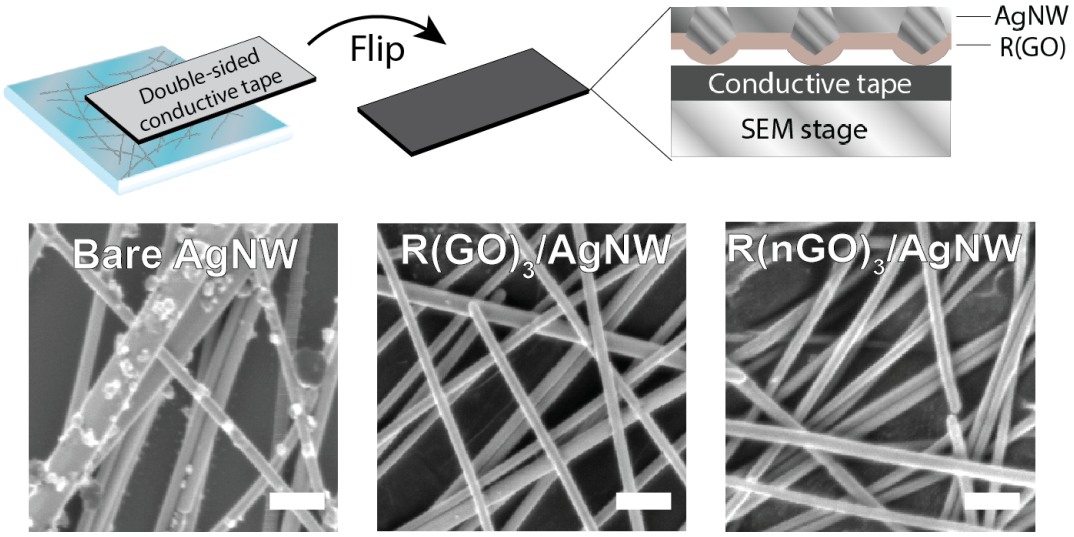

Figure 4-19: SEM images showing the exposed AgNWs of degraded samples taken out after 10 days.

For all thicknesses, R(GO)-covered AgNWs were observed to have slightly better stability compared to R(nGO)-covered AgNW, although the difference between the two was not significant for each n. Although the diffusion length through the layered

structure of a R(GO) film should be significantly longer than for a R(nGO) film considering an order of magnitude difference in average flake size, the trend of increasing resistance over time was primarily similar for both R(GO) and R(nGO)-based films for a given thickness. This means that for reduced GO films, the barrier properties against gas or moisture exhibit very little size dependence, in agreement with a previous study by Su et al. [128] which observed that chemically reduced GO is practically impermeable against moisture or gas penetration with no dependence on flake size. Zhang et al. [163] also found little difference in relative resistance increase between when AgNW was covered by small RGO sheets or large RGO sheets, although the sizes compared were much larger than our study (45 μm vs. 500 μm).

The observed excellent barrier properties of R(GO) and R(nGO) originate from their collapsed interlayer spacing which leaves no space for the transport of water or other molecules. This is in contrast with GO before chemical reduction, where free permeation of water occurs via a network of GO capillaries filled with one or two monolayers of water. Our XRD results have indeed shown that the interlayer spacing for R(nGO) (0.39 nm) approaches that of graphite, [83] while that of GO is much wider (1 nm) (Figure 4-5a,c). This is further illustrated by the fact that $(GO)_n$ and $(nGO)_n$ covered AgNWs degraded much more severely compared to their reduced counterparts (Figure 4-18b). In particular, we have observed that $(nGO)_n$/AgNW undergoes a more rapid degradation than bare AgNWs, which suggests that nGO coating causes the AgNW surface to be saturated with water creating a favorable environment for rapid sulfidation.

4.5.4 Mechanical Stability

Finally, the mechanical stabilities of R$(GO)_3$/AgNW and R$(nGO)_3$/AgNW coated on 125 μm thick PET were evaluated for potential applications in flexible electronic devices. AgNW-network-based films demonstrated superior mechanical stability over continuous ITO thin films, in agreement with previous studies. [37] Figure 4-20a shows the percent resistance change ($\Delta R/R_0$) as a function of bending radius r (setup as shown in the inset). The bending radius r and nominal strain ϵ acting on the thin

film on top of the substrate with thickness h are related as $\epsilon = h/2r$. [54] ITO on PET shows a steep increase in resistance around $r = 6.5$ mm or $\epsilon = 1.5\%$. This is expected due to the brittle nature of the ITO thin film that causes the formation of cracks during straining. [8] On the other hand, bare AgNWs show a significantly reduced change in resistance upon bending, reaching only 3.25% change in resistance around $r = 4$ mm ($\epsilon = 1.5\%$). The excellent flexibility is thanks to the ability of the AgNW-network to simply stretch the network rather than straining the individual wires. AgNWs can reorient themselves in response to applied tensile strain before individual nanowires are strained and break. Nevertheless, the 3.25% change in resistance upon bending for bare AgNWs is not entirely negligible, indicating that the reorientation of AgNWs upon straining causes the contact between nanowire junctions to become loose. [164] Interestingly, we have observed that the change in resistance is reduced to 1.25% and 1% at the same bending radius of $r = 4$ mm when coating with R(GO) and R(nGO) layers, respectively. This is possibly due to the R(GO) and R(nGO) overcoating layer improving the interwire contact and AgNW-substrate adhesion, helping the AgNW-AgNW contact quality to remain intact under strain.

We have also subjected the samples to bending fatigue tests, as shown in Figure 4-20b. Each AgNW-based sample was subject to the same bending cycle from an unbent state to a bending radius $r = 4$ mm ($\epsilon = 1.5\%$) for 1200 cycles at a fixed bending rate. For bare AgNWs, it was observed that the resistance increases rapidly for the first 100 cycles to $\sim$7% and follows a slower trend to reach 12.5% increase at the end of 1200 cycles. The rapid increase in resistance during the early stage followed by a slower rate of increase is in agreement with bending fatigue tests conducted on AgNWs by a previous study [165], and is related to the irreversible nanowire junction contact upon repeated bending cycles. In contrast, for $R(GO)_3$/AgNW and $R(nGO)_3$/AgNW, a significantly improved fatigue resistance compared to bare AgNW was observed. Both $R(GO)_3$/AgNW and $R(nGO)_3$/AgNW on PET exhibited only a $\sim$3% increase in resistance after 1200 bending cycles. Throughout the bending fatigue test, $R(nGO)_3$/AgNW, in particular, demonstrated a slightly smaller variation in resistance between the unbent and bent state compared to $R(GO)_3$/AgNW, which

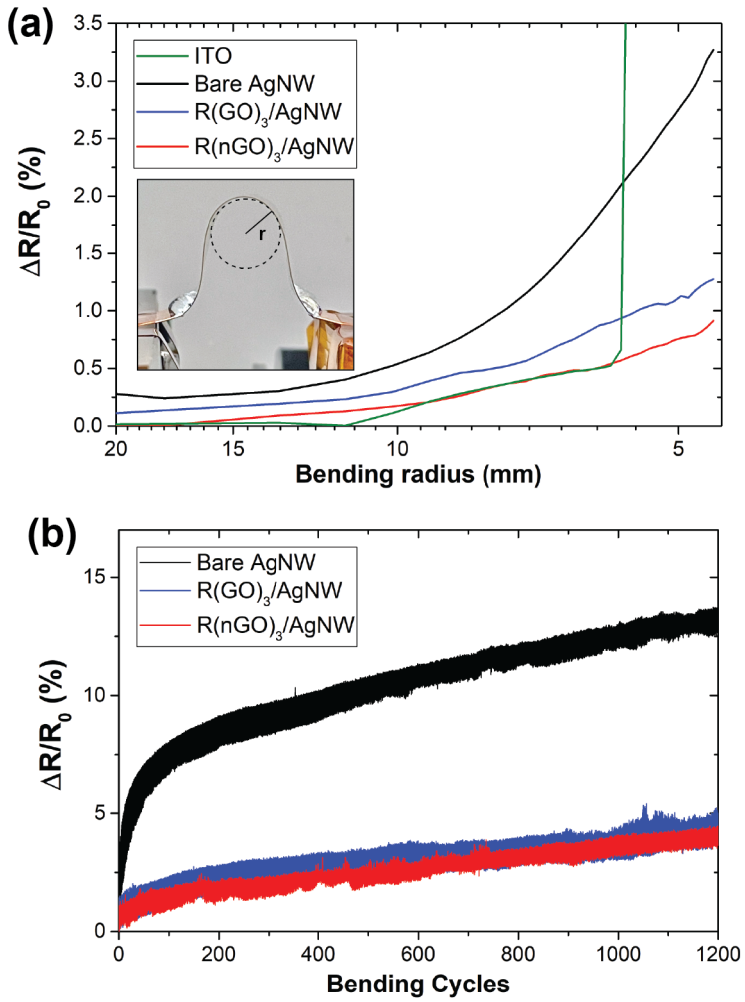

Figure 4-20: (a) Change in resistance ($\Delta R/R_0$) of ITO, bare AgNW, R(GO)$_n$/AgNW and R(nGO)$_n$/AgNW on PET as a function of bending radius. Inset shows the bending test setup indicating the bending radius. (b) Change in resistance of above samples during 1200 bending cycles to a bending radius of $r = 4$ mm.

is in line with observations made in Figure 4-20a. While similar results were also observed by previous studies that employed graphitic coating layers with unoptimized conformality [91,140], our measurements indicate that a conformal R(nGO) coating is an effective resistance stabilizer for AgNW networks under repeated straining cycles.

4.6 Cost Analysis of the Process

One of the main merits of the process introduced in this chapter is its potential to be translated into large-scale manufacturing, specifically through roll-to-roll (R2R) manufacturing. [153] For instance, initial AgNW coating and nGO LbL deposition cycles can be performed in a continuous manner by mayer rod coating and sequential liquid immersion, respectively. The final reduction step using a reducing agent can be performed in a similar immersive manner. A schematic of this hypothetical R2R setup is shown in Figure 4-21. In this section, a basic cost analysis regarding the process to fabricate R(nGO)$_n$/AgNW is presented, following closely a similar analysis performed by Sandstrom and Edman for the R2R fabrication of Light Emitting Electrochemical Cells. [166]

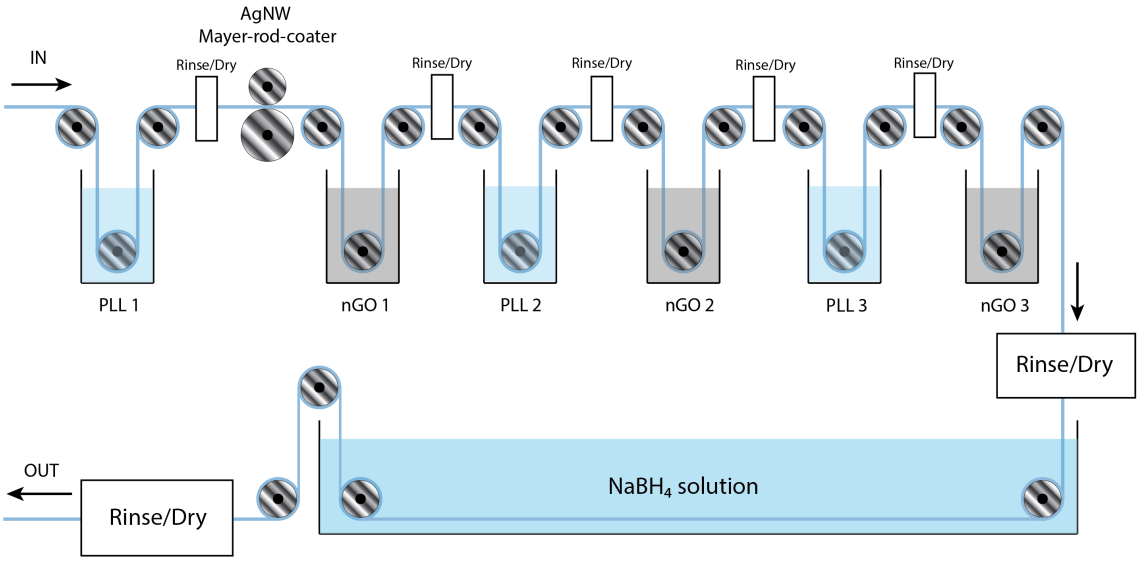

Figure 4-21: A schematic of a hypothetical R2R production of R(nGO)$_3$/AgNW on PET. Diagrams are not to scale.

Three process cases are compared to quantify the cost of R(nGO)$_3$/AgNW:

Case A. Low-volume batch processing involving spin coating of GO

Case B. Low-volume batch processing involving LbL process used in this study

Case C. Large-volume R2R fabrication based on LbL process

Not considering the process yield, the total cost to produce a unit area (m^2) of $R(nGO)_3$/AgNW on PET films can be roughly broken down into the materials cost, capital expenditure (CAPEX) and processing cost [166]:

$$Cost_{TOTAL} = Cost_{CAPEX} + Cost_{MAT} + Cost_{PROCESS} \tag{4.3}$$

4.6.1 CAPEX

Different equipment are required for each production cases, which are outlined in Table 4.1. For Cases A and B, the main difference is the process to coat GO. As a representative lab-scale technique, spin coating is used for GO for Case A, while a more scalable LbL method is used for Case B (identical to the process introduced in this chapter). For both cases, spin coating is used to coat AgNW. For Case C, we assume that a R2R apparatus is used to coat AgNW and GO continuously, and industrial grade sonicators capable of processing up to 20L of liquid are used. The CAPEX for each case is calculated as a per week basis, assuming a 10 year depreciation period (52 weeks per year). (Table 4.1)

CAPEX				
Equipment	Cost ($)	Case A	Case B	Case C
Probe sonicator (lab)	3,369	1	1	0
Bath sonicator (lab)	1,130	1	1	0
Probe sonicator (industrial)	14,000	0	0	1
Bath sonicator (industrial)	5,000	0	0	1
Scale	1,500	1	1	1
Spin coater	5,000	1	1	0
Drying oven	2,500	1	1	1
R2R apparatus	150,000	0	0	1
Total cost ($)	-	13,499	13,499	173,000
Cost per week($)	-	25.96	25.96	332.69

Table 4.1: Summary of CAPEX associated with cases A, B and C.

The prices of each equipment are only estimates based on a survey of popular manufacturers. Especially, a R2R apparatus can be customized, and its price ranges from $20,000 from $500,000. We choose $150,000 as a representative price as a commonly

encountered price for pre-customized large-scale R2R apparatus. It is noted that the cost of using laboratory space or factory floor is not explicitly taken into account, due to lack of reliable information. Nevertheless, this basic first-order Capex estimation already shows that the initial equipment installment cost is an order of magnitude higher for Case C compared to lab-scale production, which is compensated by the very low processing cost, as will be shown in subsequent sections.

4.6.2 Materials Cost

Materials Cost				
Material	Manufacturer	Price ($)	Unit size	Unit price
PET	Alibaba vendor	750	3623.2 m^2	0.21 $/$m^2$
Graphene Oxide	Graphenea	1430	100 g	5.72 $/g
poly-L-Lysine (0.1%)	Alibaba vendor	13	25 mg	0.52 $/ml
AgNW	in-house	-	-	11.81 $/g
$NaBH_4$	Sigma-Aldrich	415	500 g	0.83 $/g

Table 4.2: Summary of materials costs associated with cases A, B and C.

A summary of the raw materials' per-unit-cost used for all cases can be seen in Table 4.2. All of the raw materials' prices are those listed in the manufacturers' respective websites as of April 2022. The price of common solvents such as deionized water and isopropanol used to dilute or disperse raw materials has been omitted for simplicity. The assumption is that such solvents are common enough to be sufficiently cheap and can be included in the facilities use cost which is not explicitly considered. It should be noted that the prices indicated in this table are only rough guidelines, as wholesale unit prices (typically through a Alibaba vendor) vary widely depending on the scale of purchase. The price of GO also varies widely across different manufacturers, along with their overall quality and chemical properties, which should be taken into account when actual production is concerned.

For GO, the price is calculated from that of a commercial 4L GO solution with 2.5 wt % concentration, and the unit price is calculated in terms of solid content mass. poly-L-Lysine (PLL) used for LbL deposition of GO has a concentration of 0.1% w/v, and the price in terms of solid mass has been converted to unit price in

Materials Cost for Case A - per Sample			
Material	Conc. (mg/ml)	Volume per sample (ml)	Mass per sample (g)
GO	0.5	1.5	0.00075
AgNW	1.7	0.5	0.00085
$NaBH_4$	5.7	30	0.17

Materials Cost for Case A - per Batch		
Material	Amount used per batch	Cost per batch ($)
PET	0.0026 m^2	0.0005
GO	0.003 g	0.0172
AgNW	0.0034 g	0.0402
$NaBH_4$	0.17 g	0.1411
	Total Materials Cost per Batch	0.20
	Total Materials Cost per m^2	77.09

Table 4.3: Materials costs associated with Case A.

terms of volume for a 0.1 w/v% PLL solution in water. For AgNW unit price in terms of solid mass, a value calculated assuming in-house synthesis was used. [38] Finally, for $NaBH_4$, the unit price per solid mass in grams was used.

Next, the material costs associated with each production case are calculated. Since Cases A and B are batch processes, the number of samples handled per batch, and the size of each sample must be predefined. For Case A, it is assumed that each batch contains four 2.5 cm by 2.5 cm samples on PET, and for each sample, 3 nGO spin coating cycles are used without PLL. According to our experience, spin coating a 2.5 cm by 2.5 cm substrate requires 0.5 ml volume of liquid, so 1.5 ml of nGO solution in total will be used per sample, and 0.5 ml of AgNW solution will be used. The mass used per sample and per batch have been calculated accordingly. The samples are typically immersed in a 30 ml of 150 mM (5.7 mg/ml) solution of $NaBH_4$ after nGO deposition and can contain the 4 samples in a single batch. The total materials cost per batch and per m^2 were thus calculated (Table 4.3)

For Case B, which is the process actually demonstrated in this chapter, it is assumed that each batch contains four 7.5 cm by 7.5 cm samples on PET, and for each sample, 3 nGO LbL cycles are used with PLL. According to our experience, a single cycle of LbL coating wastes far less liquid compared to spin coating, only about 0.01 ml for a 2.5 cm by 2.5 cm substrate. Extrapolating this to a sample size of 7.5

Materials Cost for Case B - per Sample			
Material	Conc. (mg/ml)	Volume per sample (ml)	Mass per sample (g)
GO	0.5	0.27	0.000135
PLL	default	0.27	-
AgNW	1.7	4.5	0.00765
$NaBH_4$	5.7	200	1.13

Materials Cost for Case B - per Batch		
Material	Amount used per batch	Cost per batch ($)
PET	0.0225 m^2	0.0047
GO	0.00054 g	0.0031
PLL	1.08 ml	0.56
AgNW	0.0306 g	0.3614
$NaBH_4$	1.13 g	0.94
	Total Materials Cost per Batch	1.87
	Total Materials Cost per m^2	83.17

Table 4.4: Materials costs associated with Case B.

cm by 7.5 cm, 0.09 ml of GO solution and PLL solution will be used per sample per cycle. For 3 LbL cycles, 0.27 ml of each solution are used. Since AgNW still uses spin coating, 4.5 ml of AgNW solution will be used per sample. The mass used per sample and per batch have been calculated accordingly. The samples are typically immersed in a 200 ml of 150 mM (5.7 mg/ml) solution of $NaBH_4$ and can contain the 4 samples in a single batch. The total materials cost per batch and per m^2 were thus calculated (Table 4.4)

Finally for Case C, which is the continuous R2R process, the material cost is calculated in terms of unit area (m^2). Again, 3 nGO LbL cycles are used with PLL. We extrapolate volume of liquid used for Case B to a sample size of 1 m^2, so that 16 ml of GO solution and PLL solution will be used per m^2 per cycle. For 3 LbL cycles, 48 ml of each solution are used. For R2R coating of AgNW, we are assuming a process such as Mayer rod coating is used, where AgNW solution wastage can be ignored. Based on a previous study, we are assuming the areal mass density required to reach 10 Ω/sq is 40 mg/m^2, and the AgNW solution used is less concentrated than for spin coating. Therefore, 40 ml of 1 mg/ml AgNW solution will be used per m^2. Near the end of the roll, it can be assumed that the film passes through a large vat of 150 mM (5.7 mg/ml) solution of $NaBH_4$ for 2 hours for reduction of nGO. (Figure 4-21) The

Materials Cost for Case C			
Material	Conc. (mg/ml)	Volume per m^2 (ml)	Mass per sample (g)
GO	0.5	48	0.024
PLL	default	48	-
AgNW	1	40	0.04
$NaBH_4$	5.7	8889	50.37

Materials Cost for Case C		
Material	Amount used per m^2	Cost per m^2 ($)
PET	1 m^2	0.21
GO	0.024 g	0.14
PLL	48 ml	24.96
AgNW	0.04 g	0.47
$NaBH_4$	50.37 g	41.81
	Total Materials Cost per m^2	67.58

Table 4.5: Materials costs associated with Case C.

amount of $NaBH_4$ solution used per m^2 has been calculated by extrapolating from Case B, where it was assumed that 200 ml was used for a single batch that contained four 7.5 cm by 7.5 cm samples. This results in using 8.9 liters of $NaBH_4$ solution per m^2. The total materials cost per batch and per m^2 were thus calculated in Table 4.5.

4.6.3 Process Cost

The process cost for all cases can be considered in terms of the cost of labor and the throughput of each process. Cases A and B can be assessed in a similar manner since both are batch processes. For labor costs, we assume a technician works 52 weeks per year, 40 hours per week, and costs $80/hour including wage and facility use fees. From our own experience, a skilled technician can make at most 3 batches per workday. Therefore, the throughput for each case can be calculated in terms of sample area (m^2) per week. For Case A, the throughput is 0.0375 m^2/week = (0.025 m * 0.025 m) * (4 samples/batch) * (3 batches/day) * (5 days/week). The cost per week is 3200$/week = (80$/hour)*(40 hours/week). The process cost per m^2 is then given by 85333 $/$m^2$ = (3200 $/week)/(0.0375 m^2/week) (Table 4.6).

In a similar manner for Case B, the throughput is 0.3375 m^2/week = (0.075 m * 0.075 m) * (4 samples/batch) * (3 batches/day) * (5 days/week). The cost per week

Process Cost for Case A and B		
Cases	Case A	Case B
One full-time technician makes	3 batches/day	3 batches/day
1 batch contains	4 samples	4 samples
Area m^2 per batch	0.0026	0.0225
Area m^2 per week	0.0375	0.3375
Process cost per week ($)	3,200	3,200
Process cost per m^2 ($)	85,333	9,481.48

Table 4.6: Process costs associated with Cases A and B.

Process Cost for Case C	
Number of technicians	2
Web speed	10 m/hr
Web width	1.8 m
Area m^2 per week	720 m^2
Process cost per week ($)	6,400
Process cost per m^2 ($)	8.89

Table 4.7: Process costs associated with CaseC.

is 3200$/week = (80$/hour)*(40 hours/week). The process cost per m^2 is then given by 9481.48 $/$m^2$ = (3200 $/week)/(0.3375 m^2/week) (Table 4.6).

For Case C, since it is a continuous R2R process, the speed of the roll (web speed) is an independent variable. We assume here a relatively slow web speed of 10 m/hr and also assume that the width of the PET roll is 1.8 m. Assumptions on the labor cost is the same as other cases, but we assume two technicians are required to sustain the process. Although the cost associated with facility use may be different considering the cost of electricity needed to operate the machine, we omit in this analysis due to lack of information. Using the above assumptions, the process cost per area for Case C is 8.89 $/$m^2$, significantly lower than Cases A and B thanks to the high throughput enabled by the R2R process. (Table 4.7)

4.6.4 Total Cost

Finally, we calculate the total cost associated with each case according to equation 4.3. The summary is shown in Table 4.8 and Figure 4-22. When using the novel LbL process as discussed in this chapter (Case B), we may expect an order of magnitude

Total Cost ($/m^2)				
Cases	Cost (Materials)	Cost (CAPEX)	Cost (Process)	Cost (Total)
A	77.09	692.26	85,333.33	86,102.68
B	83.17	76.92	9,481.48	9,641.57
C	67.58	0.46	8.89	76.94

Table 4.8: Total costs associated with each case.

reduction in cost compared to using a conventional spin coating based process (case A). However, when adapting our process to an R2R format, even more significant cost advantage can be realized, bringing the cost per m^2 down to $77. For context, the wholesale price for ITO coated PET as of April 2022 ranges from $15 to $220, depending on the order size and sheet resistance of the ITO. This result shows that our process can be competitive in the market for transparent electrodes, with the added advantage of being more flexible than ITO, and using materials that are more sustainable than indium.

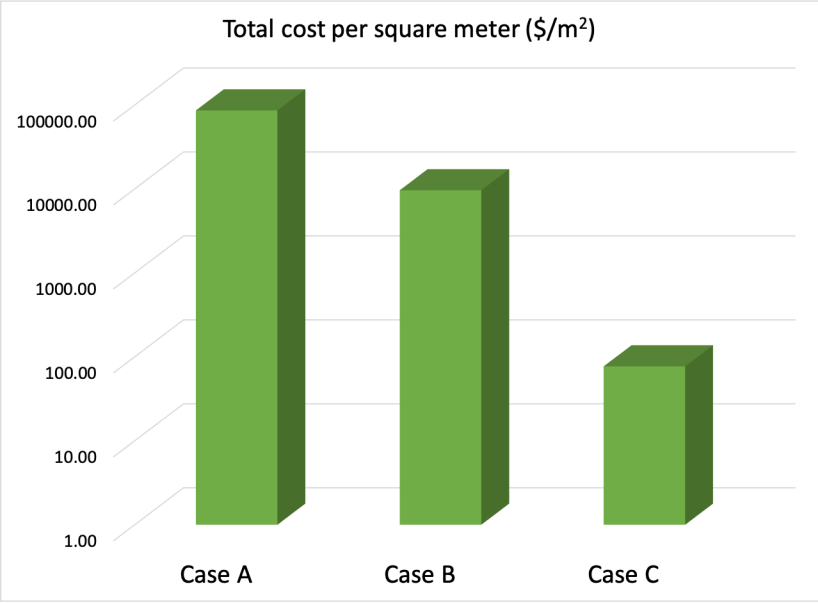

Figure 4-22: Summary of the total cost to produce R$(nGO)_3$/AgNW for all cases.

Upon examining the cost distribution between materials, capex and process (Figure 4-23), it can be seen that for batch processes (Cases A and B), the process cost constitutes the majority of the total cost, while for Case C, the total cost is mostly dominated by the materials cost. Therefore, reducing the materials cost further for

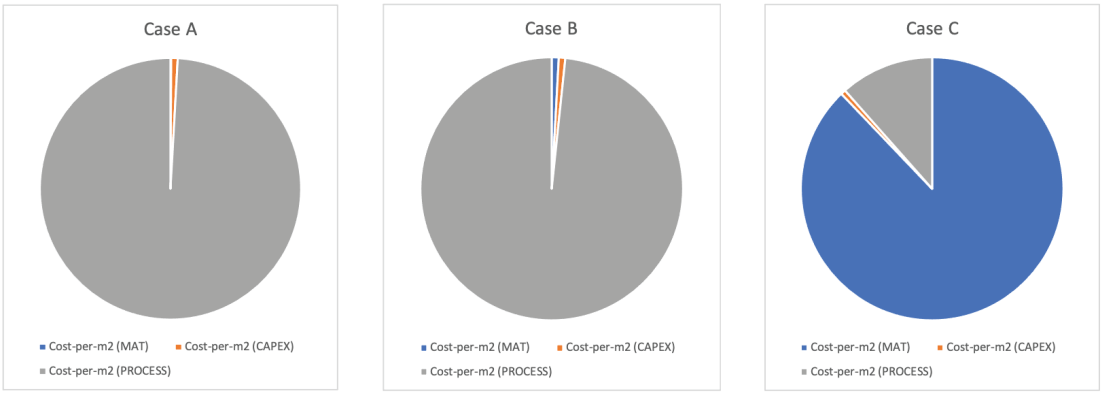

Figure 4-23: The cost distribution between materials, process, and capex

Case C is imperative to drive down the overall cost. Within the material cost for Case C, the cost of the reducing agent $NaBH_4$ and the cost of PLL accounts for 62% and 37%, respectively, while the PET, GO and AgNW cost accounts for less than 1% combined. (Table 4.5) Therefore, applying other cost-effective approaches to reduce GO, such as the use of a cheaper reducing agent, mild heat treatment and light illumination is needed. Also, expensive PLL may be substituted by a cheaper cationic polymer such as poly(diallyldimethyl-ammonium chloride) (PDDA). [53]

4.7 Conclusion

In summary, we have developed a novel process to realize a conformal protective coating on AgNW networks by using chemically reduced nanosized GO. Our all-solution-based process is facile, potentially scalable, and compatible with both glass and plastic substrates with arbitrary sizes. We have shown that R(nGO)$_n$/AgNW transparent electrodes fabricated through this process exhibit a tunable transmittance range (85∼92%) depending on the number of R(nGO) coating cycles (n) and a low sheet resistance value (17.5 Ω/sq) that is relevant for most practical applications. At the same time, our conformal R(nGO) coating process was demonstrated to be an efficient method to overcome one of the long-standing thermal and electrothermal stability issues concerning transparent electrodes based on metal nanowire networks. Combined with simultaneously increased long-term chemical and mechanical bend-

ing stabilities, our results suggest that the newly developed process improves the overall stability of the AgNW network by only using cost-effective materials and solution-based methods. We expect this method to be generally applicable towards encapsulating other less stable metallic nanowires such as copper nanowires or towards utilizing various classes of solution-processable 2-dimensional nanosheets such as MXenes. 2D/1D hybrid nanostructures fabricated in this manner will exhibit different stabilities and functionalities used in a diverse array of flexible electronic and optoelectronic devices.

Chapter 5

Conclusion and Future Outlook

The present thesis has successfully demonstrated solution-based and scalable methods to overcome some of the key failure modes regarding solution-processed Silver Nanowire Networks (AgNWs) used as transparent electrodes (TE). Specifically, two novel processes were developed to use Graphene Oxide (GO) and Reduced Graphene Oxide (RGO) as effective protective coatings for AgNW networks that can be used towards various optoelectronic devices such as organic solar cells and transparent film heaters.

In Chapter 2, an overview of failure modes associated with using MNW-based TEs was given, highlighting the fundamental aspects related to the mechanisms of degradation when exposing MNW networks to various external stresses of thermal, electrothermal, mechanical, and chemical origin. A review of some of the most relevant and economically feasible solutions by hybridizing MNWs with other materials to increase their stability, as well as their merits pertaining to specific device applications were semi-quantitatively assessed for the first time. This provides guidance on materials selection and perspective on framing MNW-encapsulant hybrids to benchmark applications for TEs. Based on this assessment, GO and RGO were chosen as materials compatible with solution-based MNW encapsulation with rich opportunities for materials-level engineering.

In Chapter 3, a process to fabricate TE where AgNW network is effectively 'sandwiched' between two GO layers was presented. The process involves electrophoretic

deposition (EPD) and solution dip treatment for the scalable fabrication of protective GO films with reliable thickness tunability, resulting in EPD-GO/AgNW/dip-GO TE. Its characterization revealed excellent conductivity and transparency, mitigating the need for high temperature treatment typically performed on AgNW networks. The defect-free EPD-GO film provides excellent chemical resilience by preventing sulfidation of Ag. We also observed a novel stabilization behavior of the AgNW network under voltage ramp, where the voltage at which failure occurs is delayed and resistance divergence typical for bare AgNWs is prevented. When applied to the back-electrode of semitransparent solar cells, the device yielded 40% overall transparency and 2.6% power conversion efficiency, while the lifetime of this solar cell was increased 5 times compared to unprotected devices under ambient conditions. The observed stability is attributed to improved protection against external moisture, oxygen and the underling acidic device layer.

In Chapter 4, I developed an cost-effective process to conformally encapsulate silver nanowire (AgNW)-based transparent conductive films with reduced nanosized graphene oxide (RnGO). Probe sonication was used to break GO into nanoscale sizes (nGO) and coated on the AgNW network by a layer-by-layer technique where positively charged polymer poly-L-lysine and negatively charged GO were alternately coated to desired thickness and chemically reduced. This coating process resulted in a simultaneous improvement in thermal stability, storage life, and bending fatigue resistance compared to uncoated AgNWs. The operation of RnGO-coated AgNW networks as a transparent film heater resulted in maximum temperature of 275°C. A more conformal coverage of the AgNW surface delays the kinetics of Ag surface atomic diffusion, the main mechanism leading to morphological change and break under elevated temperatures. Finally, the storage life was increased due to the small interspacing between stacked RnGO sheets which prevents the passage of water or oxygen. These achievements without the use of an expensive vacuum-based coating process typically required to produce AgNW-based electrodes offer possibilities for scalability in continuous roll-to-roll (R2R) manufacturing. A basic cost analysis assuming a R2R production demonstrated a competitive price-per-area against

commercial ITO.

Although the critical stability limitations of AgNW-based electrodes have been addressed in this work, other technical challenges still remain. For one, the roughness of as-coated MNW networks in general is quite high, with root-mean-square (RMS) roughness being on the order of tens of nanometers at least. For thin film-based optoelectronic devices, the high degree of roughness poses risk of device malfunctions by shunting or shorting. Therefore, a suitable coating process should not only stabilize the underlying MNWs but also efficiently planarize them. Another unaddressed realm of research with regards to solution-synthesized AgNWs is the role of the passivating ligand (PVP) which is inevitably introduced during the crystal growth step. Studies have pointed out that the removal of a hygroscopic PVP from the AgNW surface not only enhances interwire contact, but also improves the long-term chemical stability. [167] By extension, studying the role of PVP on the thermal and mechanical stability of AgNW would be an interesting topic of study. Going even further, designing new ligands altogether to divert away from using PVP during AgNW synthesis is another interesting direction of research that should require close collaboration between theoreticians and experimentalists.

It is my hope that the results presented in this thesis will continue to motivate researchers in the field of transparent electrodes to search for alternative and sustainable materials to substitute ITO in the near future. However, the application of MNW-based networks is not limited only to TEs for optoelectronic devices. The use of MNWs have also been reported in the emerging field of flexible electrochemical energy storage and harvesting devices, [168, 169] and these applications will continue to gain importance with the advent of flexible or stretchable electronics. Thus, a future direction may include in-depth investigations regarding the electrochemical properties of MNW-networks. Finally, while the present thesis only specifically demonstrated the use of AgNW, GO and RGO, other emerging 1-dimensional and 2-dimensional materials compatible with solution-based processing can also be used in principle. Therefore, from a broader perspective of economical processing of hybridized mixed-dimensional nanostructures, there are still plenty of opportunities and challenges that

need to be addressed. Investing research efforts in this direction is needed to take full advantage of the cutting-edge advances made thus far in the vast field of nanocomposite materials, and ultimately to bridge the gap between lab-scale demonstrations of new materials and their industrial-scale volume production.

Appendix A

Experimental Details for Chapter 3

A.1 Fabrication of EPD-GO/AgNW/GO Film

Prior to EPD, two 2.54 cm × 2.54 cm 316 stainless steel plates (McMaster Carr) are cleaned thoroughly by ultrasonication in acetone, followed by rinsing in ethanol and deionized water. One of the plates to be used for EPD deposition is then spin-coated with cellulose acetate (Sigma-Aldrich) solution in acetone (4 mg/mL) with a spin speed of 900 rpm for 1 min. The steel plates are then attached parallel to each other in an electrophoretic deposition (EPD) cell with a fixed distance of 5 mm. The deposition substrate with cellulose acetate coating is attached to the positive contact as an anode. The electrodes are then immersed in a diluted aqueous GO solution (Graphenea), and a constant voltage of 5 V is applied across the EPD cell for 4 min by using a Tektronix PS-282 DC power supply, leaving a thin film of EPD-GO on the anode. The electrodes are then slowly withdrawn from the GO solution. The EPD-GO on a stainless steel plate is spin-coated with the AgNW solution in isopropanol (2 mg/mL, ACS Materials) with a spin speed of 600 rpm for 40 s. The NW average diameter is 50 nm. The NW average length is in the range 100–200 μm. The resulting AgNW-based product on a stainless steel plate is then immersed in 1.5 mg/mL aqueous GO solution for 1 min before being rinsed by deionized water and blow-dried with nitrogen gas. Next, the entire film on the stainless steel plate is immersed in acetone for at least 6 h and then transferred to deionized water.

The transparent EPD-GO/AgNW/GO film is then liberated from the underlying steel substrate and is transferred to a transparent insulating substrate such as glass (Corning Eagle XG) or PET (DuPont Teijin Melinex ST505). Finally, the transferred film is dried on a hot plate at 40 °C and thoroughly rinsed with acetone and ethanol.

A.2 Optical, Electrical, Chemical, and Morphological Characterization

The optical characterization of electrodes was performed with a PerkinElmer Lambda 1050 UV–visible–near-IR spectrophotometer equipped with an integrating sphere. A Jandel cylindrical linear four-point probe with a tungsten probe separated by 1 mm with a probe radius of 40 μm was used to measure the sheet resistance of all the electrodes. Sheet resistance measurements were taken on five different spots for each sample and averaged. X-ray photoemission spectroscopy (XPS) measurements were performed on a Thermo Fisher Scientific K-Alpha system with a monochromatic Al Kα X-ray source (1486.6 eV). Surface charging effects due to the insulating nature of GO were compensated for by using a low-energy flood gun. Step sizes of 1 and 0.1 eV were used for survey scan and high-resolution spectra, respectively. Quantification and deconvolution of spectra were performed by using the data analysis software Avantage (associated with the K-Alpha system), after Shirley background correction. Scanning electron microscopy (SEM) images were obtained by using a Hitachi SU8100 high-resolution SEM with an accelerating voltage of 1–4 keV and a combination of upper (in-lens) and lower secondary electron detectors. Atomic force microscopy (AFM) measurements were performed on an Asylum Research Cypher AFM on standard AC-air tapping mode.

A.3 Chemical and Electrical Stability Studies

To perform chemical stability studies, the electrodes were stored on a Torrey Pines HP60A programmable hot plate set at 80 °C either in the lab environment or inside a

controlled humidity chamber (5533 environmental chamber by Electro-Tech Systems Inc.) and were only taken out once a day briefly to measure the sheet resistance. Relative humidity was recorded for the duration of the experiment with a VWR hygrometer. In situ electrical stability studies were performed with a Keithley 2401 sourcemeter unit (SMU) using two probes. Electrical contacts were made on opposite ends of 2.54 cm × 2.54 cm samples with a conductive silver paste (DuPont) and dried for 12 h in air. Voltage ramps were applied on the samples via a LabView program interfaced with the SMU. A FLIR A615 Infrared camera was used to record the temperature of our samples during voltage ramps.

A.4 ST-OSC Device Fabrication

A.4.1 Substrate and Bottom Electrode

150 nm-thick patterned ITO electrodes sputtered on 2.5 × 2.5 cm^2 large and 0.7 mm thick Eagle XG glass substrates were purchased from Thin Film Device Inc. ITO bottom electrodes had a sheet resistance of 20 Ω/sq, a total transmittance (at λ = 550 nm) of 88%, and a work function of ∼4.8 eV. Prior to device fabrication, ITO samples were successively ultrasonicated in Acetone, IPA, and deionized water for 10 min and further cleaned by UV–ozone treatment for 15 min.

A.4.2 Electron Transport Layer

A tin(IV) oxide (SnO_2) nanoparticle ink with the "Avantama Ltd. N-31" reference was purchased from Sigma-Aldrich. For each device, 0.35 mL of solution was deposited onto ITO samples by spin-coating with a spin speed of 3000 rotation per minute (rpm) for 1 min and annealed at 140 °C for 5 min, leading to a thickness of ≈35–38 nm.

A.4.3 Active Layer

10 mg of polymer donor "PV-D4610" purchased from Merck (Lisicon series) was mixed with 20 mg of a fullerene acceptor $PC_{60}BM$ purchased from American Dye Source Inc. in 1 mL of 1,2-dichlorobenzene, stirred vigorously for 30 min while heating at 70 °C. 0.2 mL of active layer solution was then deposited by spin-coating onto the SnO2 layer with a spin speed of 1000 rpm for 80 s and annealed at 70 °C for 2 min, leading to a thickness of ≈150 nm.

A.4.4 Hole Transport Layer

PEDOT:PSS (1:2.5 ratio) dispersed in water with the "Heraeus–HTL solar" reference was purchased from Ossila and mixed with 30 wt % (with respect to the PEDOT:PSS solid content) of GOPS (purchased from Sigma-Aldrich), corresponding to a GOPS volume ratio of 0.4%. The cross-linked HTL solution was deposited by spin-coating onto the active layer with a spin speed of 1500 rpm for 60 s and annealed at 120 °C for 2 min, leading to a thickness of ≈90 nm.

A.4.5 Back Electrode Fabrication

Evaporated Ag Electrode

100 nm-thick Ag film was thermally evaporated through a shadow mask at a rate of 1 Å/s, in a chamber with a base pressure of 10^{-6} Torr.

Bare AgNW Electrode

AgNWs with an average diameter and length of 50 nm and 10–100 μm, respectively, dispersed in IPA were purchased from ACS Materials. Prior to spray–deposition, the device's core-stack was positioned onto a hotplate at 100 °C. AgNW solution was spray-deposited onto the device core stack through a metal mask with same geometry as the thermal evaporation mask. The spray head and gas compressor were purchased from Iwata ("CN gravity feed dual action airbrush kit") and vertically mounted onto a

self-customized computer-controlled CNC mill, allowing for automated planar movements of the spray head. Note that the AgNW solution was significantly diluted (from 20 to 0.4 mg mL–1) to prevent clogging in the spray head and ensure uniform network. Similarly, the pressure, hotplate temperature, and speed of the movement spray head were carefully adjusted in order to minimize the so-called "coffee-ring" effect (47,48) and achieve an electrically uniform AgNW network. (49)

A.5 ST-OSC Device Characterization

J-V measurements were performed with a Keithley 6487 picoammeter, with (100 ± 10) mW cm^{-2} simulated solar illumination provided by a 150 W Newport 96000 Xe arc-lamp equipped with an AM1.5G filter and diffuser. The optical characterization of the reference AgNW samples and OPV devices was performed with a PerkinElmer Lambda 1050 UV–vis–near-IR spectrophotometer equipped with an integrating sphere. A Jandel cylindrical linear four-point probe with a tungsten probe separated by 1 mm with a probe radius of 40 μm was used to measure the sheet resistance of reference AgNW samples. Sheet resistance measurements were taken on five different spots for each sample and averaged. Areal mass density of the reference AgNW samples was measured by capturing SEM images at 10 different locations each, followed by performing image analysis (binarization) using a Python-based script. Work function measurement of back electrode materials was performed by XPS on a Thermo Fisher Scientific K-Alpha system with a monochromatic Al Kα X-ray source (1486.6 eV). SEM images were obtained by using a Hitachi SU8100 high-resolution SEM with an accelerating voltage of 1–4 keV and a combination of upper (inlens) and lower secondary electron detectors. Surface morphology analysis was performed with Asylum Research Cypher S AFM. Thickness measurements were performed with a Bruker DXT Stylus Profilometer. For all aging experiments, the storage temperature and RH were recorded every minute using a "Gateway SensorPush G1" sensor.

Appendix B

Experimental Details for Chapter 4

B.1 Transparent Electrode Fabrication

Prior to deposition, a glass substrate (Corning Eagle XG) or a polyethylene terephthalate (PET) film (DuPont Teijin Melinex ST505) is cleaned thoroughly by a 10-minute ultrasonication in acetone (only for glass), followed by rinsing in ethanol and deionized water (DIW). The blow-dried substrates are then treated with a UV-Ozone cleaner for 15 minutes. Then the substrates were incubated in poly-L-lysine solution (0.1 % w/v in H_2O, Sigma-Aldrich) for 10 minutes, rinsed in DIW and blow-dried. Then, 0.5 ml of 100 nm diameter AgNW dispersed in isopropanol (ACS Materials) with a diluted concentration of 1.7 mg/ml was spin coated on the substrates at a spin speed of 3000 rpm. This is followed by immersing the AgNW-coated substrate in a GO or nGO aqueous solution (0.5 mg/ml, Graphenea) for 1 minute. Note that nGO was prepared by probe sonicating the GO solution continuously for 2 hours with a QSonica Q55 sonicator. Additional GO or nGO deposition were done n times by alternating cycles of immersion in the poly-L-lysine solution for 5 minutes and immersion of the sample in GO/nGO solution for 1 minute. The obtained coated AgNW sample was finally treated in 150 mM $NaBH_4$ (Sigma-Aldrich) aqueous solution for 2 hours and thoroughly rinsed with DIW which resulted in R(GO)n/AgNW or R$(nGO)_n$/AgNW. Electrical contacts were made on opposite ends of 2.54 cm $\times$ 2.54 cm samples with a conductive silver paste (DuPont) and dried in air.

B.2 Characterization

The optical characterization of electrodes was performed with a PerkinElmer Lambda 1050 UV–visible–near-IR spectrophotometer equipped with an integrating sphere. A Jandel cylindrical linear four-point probe with a tungsten probe separated by 1 mm with a probe radius of 40 μm was used to measure the sheet resistance of all the electrodes. Sheet resistance measurements were taken on five different spots for each sample and averaged. X-ray photoemission spectroscopy (XPS) measurements were performed on a Thermo Fisher Scientific K-Alpha system with a monochromatic Al Kα X-ray source (1486.6 eV). Surface charging effects due to the insulating nature of GO were compensated for by using a low-energy flood gun. Step sizes of 1 and 0.1 eV were used for survey scan and high-resolution spectra, respectively. Quantification and deconvolution of spectra were performed by using the data analysis software Avantage (associated with the K-Alpha system), after Shirley background correction. X-ray diffraction (XRD) was carried out on a Rigaku SmartLab using Cu Kα source (1.5406 Å). Scanning electron microscopy (SEM) images were obtained by using a Hitachi SU8100 high-resolution SEM with an accelerating voltage of 1–4 keV and a combination of upper (in-lens) and lower secondary electron detectors. Atomic force microscopy (AFM) measurements were performed on an Asylum Research Cypher AFM on standard AC-air tapping mode, and the images were analyzed by Gwyddion software. Malvern Zetasizer was used to measure the zeta potential and DLS size distribution of GO and nGO dispersions in water.

B.3 Stability measurements

In situ thermal stability studies were performed by placing the samples in a tube furnace (Thermo Scientific HTF55122A Lindberg/Blue) and connecting the sample terminals to a Keithley 2401 sourcemeter unit (SMU) using two probes. The resistance across the sample was measured during a programmed thermal ramp of 6°C/min. In situ electrothermal stability studies were performed by applying voltage ramps and

plateaus on the samples suspended in air via a custom LabView program interfaced with a SMU. A FLIR A615 Infrared camera was used to record the temperature of our samples during the experiment. To perform chemical stability studies, the electrodes were stored on a Torrey Pines HP60A programmable hot plate set at 80 °C inside a controlled humidity chamber (5533 environmental chamber by Electro-Tech Systems Inc.) set to 80% relative humidity were only taken out once a day briefly to measure the resistance. Mechanical stability studies were performed by preparing the samples on a flexible PET substrate strip (1 cm by 5 cm) which was fixed on the motorized moving stage. Electrical contact to the SMU was made using copper tape and In-Ga Eutectic (Sigma-Aldrich).

Table B.1: Compilation of different AgNW-based transparent film heater performance reported in literature

Encapsulant for AgNW	Solution Processed?	%T	Max T (°C)	Voltage (V)	Test method	Ref
$R(nGO)_3$	Yes	85	275	14	2V-14V holds for 15 min	This work
None	Yes	80	80	9	9V hold for 2 min	[170]
None	Yes	82	145	6	6V hold for 90 sec	[164]
None	Yes	86	124	5.5	5.5V hold for 80 sec	[171]
None	Yes	65	128	7	7V hold for 150 sec	[172]
CNT	Yes	94.5	110	15	15V hold for 120 sec	[173]
CNT	Yes	83	186	12	12V hold for 100 sec	[174]
RGO-GO	Yes	85	148	-	10 mA-110 mA holds for 30 sec	[13]
MBI	Yes	88	130	12	12V hold for 10 min	[175]
PEDOT:PSS	Yes	87	200	20	20V hold for 5 min	[176]
PEDOT:PSS	Yes	74	100	40	40V hold for 90 sec	[177]
Gr/PEDOT:PSS	Yes	77	100	12	12V hold for 40 sec	[178]
ITO nanoparticle	Yes	89	94	6	6V hold for 150 sec	[179]
Graphene	No	87.5	231	8	8V hold; time not specified	[180]
RGO	No	80	225	15	15V hold for 360 sec	[163]
AlO_x	No	88	81	7	7V hold for 90 sec	[181]
PEDOT:PSS/ITO	No	95	115	11	11V hold for 5 min	[182]
TiO_2	No	87	235	7	2V increment after 50 min hold	[69]
NiO	No	77	200	7	7V hold for 5 min	[183]
GZO	No	79	176	6	1V increment after 85 sec hold	[184]
SnO_2	No	87.6	170	7	7V hold for 4 min	[185]
AZO	No	85.6	130	-	3V/cm hold for 120 sec	[186]

Bibliography

[1] D. B. Fraser and H. D. Cook. Highly Conductive, Transparent Films of Sputtered In2x Sn x O3y. *Journal of The Electrochemical Society*, 119(10):1368, oct 1972.

[2] G. Haacke. New figure of merit for transparent conductors. *Journal of Applied Physics*, 47(9):4086–4089, sep 1976.

[3] Martin Dressel and George Grüner. Electrodynamics of Solids: Optical Properties of Electrons in Matter. *Electrodynamics of Solids*, jan 2002.

[4] Sukanta De and Jonathan N. Coleman. The effects of percolation in nanostructured transparent conductors. *MRS Bulletin*, 36(10):774–781, oct 2011.

[5] Aman Anand, Md Moidul Islam, Rico Meitzner, Ulrich S Schubert, Harald Hoppe, A Anand, Md M Islam, R Meitzner, U S Schubert, and H Hoppe. Introduction of a Novel Figure of Merit for the Assessment of Transparent Conductive Electrodes in Photovoltaics: Exact and Approximate Form. *Advanced Energy Materials*, 11(26):2100875, jul 2021.

[6] H. Kim, C. M. Gilmore, A. Piqué, J. S. Horwitz, H. Mattoussi, H. Murata, Z. H. Kafafi, and D. B. Chrisey. Electrical, optical, and structural properties of indium–tin–oxide thin films for organic light-emitting devices. *Journal of Applied Physics*, 86(11):6451, nov 1999.

[7] Andreas Klein. Transparent Conducting Oxides: Electronic Structure–Property Relationship from Photoelectron Spectroscopy with in situ Sample Preparation. *Journal of the American Ceramic Society*, 96(2):331–345, feb 2013.

[8] Strain-dependent electrical resistance of tin-doped indium oxide on polymer substrates. *Applied Physics Letters*, 76(11):1425, mar 2000.

[9] Liu Yang, Liu Yang, Liu Yang, Xinan Xu, Yi Yuan, Zhihao Li, Sailing He, Sailing He, Sailing He, and Sailing He. Meter-scale transparent conductive circuits based on silver nanowire networks for rigid and flexible transparent light-emitting diode screens. *Optical Materials Express, Vol. 9, Issue 12, pp. 4483-4496*, 9(12):4483–4496, dec 2019.

[10] Daniel Langley, Gaël Giusti, Céline Mayousse, Caroline Celle, Daniel Bellet, and Jean-Pierre Simonato. Flexible transparent conductive materials based on silver nanowire networks: a review. *Nanotechnology*, 24(45):452001, nov 2013.

[11] Kyeongil Hwang, Yen-Sook Jung, Youn-Jung Heo, Fiona H Scholes, Scott E Watkins, Jegadesan Subbiah, David J Jones, Dong-Yu Kim, Doojin Vak, K Hwang, Y-s Jung, Y-j Heo, D-y Kim, F H Scholes, S E Watkins, D Vak, J Subbiah, and D J Jones. Toward Large Scale Roll-to-Roll Production of Fully Printed Perovskite Solar Cells. *Advanced Materials*, 27(7):1241–1247, feb 2015.

[12] Yen Sook Jung, Kyeongil Hwang, Youn Jung Heo, Jueng Eun Kim, Doojin Vak, and Dong Yu Kim. Progress in Scalable Coating and Roll-to-Roll Compatible Printing Processes of Perovskite Solar Cells toward Realization of Commercialization. *Advanced Optical Materials*, 6(9):1701182, may 2018.

[13] Shang Wang, Yanhong Tian, Chenxi Wang, Chunjin Hang, Yilong Huang, and Chao Liao. Chemical and thermal robust tri-layer rGO/Ag NWs/GO composite film for wearable heaters. *Composites Science and Technology*, 174:76–83, apr 2019.

[14] American Chemical Society: Periodic Table of Endangered Elements. https://www.acs.org/content/acs/en/greenchemistry/research-innovation/endangered-elements.html. Accessed: 2022-04-01.

[15] Christopher J. Traverse, Richa Pandey, Miles C. Barr, and Richard R. Lunt. Emergence of highly transparent photovoltaics for distributed applications. *Nature Energy*, page 1, oct 2017.

[16] Akshay Kumar and Chongwu Zhou. The Race To Replace Tin-Doped Indium Oxide: Which Material Will Win? *ACS Nano*, 4(1):11–14, jan 2010.

[17] Xuesong Li, Yanwu Zhu, Weiwei Cai, Mark Borysiak, Boyang Han, David Chen, Richard D. Piner, Luigi Colombo, and Rodney S. Ruoff. Transfer of Large-Area Graphene Films for High-Performance Transparent Conductive Electrodes. *Nano Letters*, 9(12):4359–4363, dec 2009.

[18] Jung-Yong Lee, Stephen T. Connor, Yi Cui, and Peter Peumans. Solution-Processed Metal Nanowire Mesh Transparent Electrodes. *Nano Letters*, 8(2):689–692, 2008.

[19] Yugang Sun, Brian Mayers, , Thurston Herricks, and Younan Xia*. Polyol Synthesis of Uniform Silver Nanowires: A Plausible Growth Mechanism and the Supporting Evidence. *Nano Letters*, 3(7):955–960, 2003.

[20] Yugang Sun, Yadong Yin, Brian T. Mayers, Thurston Herricks, and Younan Xia. Uniform Silver Nanowires Synthesis by Reducing AgNO3 with Ethylene Glycol in the Presence of Seeds and Poly(Vinyl Pyrrolidone). *Chemistry of Materials*, 14(11):4736–4745, 2002.

[21] Y. Sun and Y. Xia. Large-Scale Synthesis of Uniform Silver Nanowires Through a Soft, Self-Seeding, Polyol Process. *Advanced Materials*, 14(11):833, jun 2002.

[22] L D Marks. Experimental studies of small particle structures. *Reports on Progress in Physics*, 57(6):603–649, jun 1994.

[23] Y. Gao, P. Jiang, D. F. Liu, H. J. Yuan, X. Q. Yan, Z. P. Zhou, J. X. Wang, L. Song, L. F. Liu, W. Y. Zhou, G. Wang, , C. Y. Wang, S. S. Xie*, J. M. Zhang And, and D. Y. Shen. Evidence for the Monolayer Assembly of Poly(vinylpyrrolidone) on the Surfaces of Silver Nanowires. *Journal of Physical Chemistry B*, 108(34):12877–12881, 2004.

[24] Jin Hwan Lee, Phillip Lee, Dongjin Lee, Seung Seob Lee, and Seung Hwan Ko. Large-Scale Synthesis and Characterization of Very Long Silver Nanowires via Successive Multistep Growth. *Crystal Growth Design*, 12(11):5598–5605, nov 2012.

[25] Jung-Yong Lee, Steve T. Connor, Yi Cui, and Peter Peumans. Semitransparent Organic Photovoltaic Cells with Laminated Top Electrode. *Nano Letters*, 10(4):1276–1279, apr 2010.

[26] Whitney Gaynor, George F. Burkhard, Michael D. McGehee, and Peter Peumans. Smooth Nanowire/Polymer Composite Transparent Electrodes. *Advanced Materials*, 23(26):2905–2910, jul 2011.

[27] M. Lagrange, D. P. Langley, G. Giusti, C. Jiménez, Y. Bréchet, and D. Bellet. Optimization of silver nanowire-based transparent electrodes: effects of density, size and thermal annealing. *Nanoscale*, 7(41):17410–17423, oct 2015.

[28] Johannes Krantz, Moses Richter, Stefanie Spallek, Erdmann Spiecker, and Christoph J. Brabec. Solution-Processed Metallic Nanowire Electrodes as Indium Tin Oxide Replacement for Thin-Film Solar Cells. *Advanced Functional Materials*, 21(24):4784–4787, dec 2011.

[29] Liangbing Hu, Han Sun Kim, Jung-Yong Lee, Peter Peumans, and Yi Cui. Scalable Coating and Properties of Transparent, Flexible, Silver Nanowire Electrodes. *ACS Nano*, 4(5):2955–2963, may 2010.

[30] Vittorio Scardaci, Richard Coull, Philip E. Lyons, David Rickard, and Jonathan N. Coleman. Spray Deposition of Highly Transparent, Low-Resistance Networks of Silver Nanowires over Large Areas. *Small*, 7(18):2621–2628, sep 2011.

[31] Johannes Krantz, Tobias Stubhan, Moses Richter, Stefanie Spallek, Ivan Litzov, Gebhard J Matt, Erdmann Spiecker, and Christoph J Brabec. Spray-Coated Silver Nanowires as Top Electrode Layer in Semitransparent P3HT:PCBM-Based Organic Solar Cell Devices. *Advanced Functional Materials*, 23(13):1711–1717, 2013.

[32] David J. Finn, Mustafa Lotya, and Jonathan N. Coleman. Inkjet Printing of Silver Nanowire Networks. *ACS Applied Materials Interfaces*, 7(17):9254–9261, may 2015.

[33] Aveek Bid, Achyut Bora, and A. K. Raychaudhuri. Temperature dependence of the resistance of metallic nanowires of diameter 15 nm : Applicability of Bloch-Grüneisen theorem. *Physical Review B*, 74(3):035426, jul 2006.

[34] D. P. Langley, M. Lagrange, G. Giusti, C. Jiménez, Y. Bréchet, N. D. Nguyen, and D. Bellet. Metallic nanowire networks: effects of thermal annealing on electrical resistance. *Nanoscale*, 6(22):13535–13543, oct 2014.

[35] Hyungseok Kang, Yeontae Kim, Siuk Cheon, Gi-Ra Yi, and Jeong Ho Cho. Halide Welding for Silver Nanowire Network Electrode. *ACS Applied Materials Interfaces*, 9(36):30779–30785, sep 2017.

[36] Chihak Lee, Youngsu Oh, In Seon Yoon, Sun Hong Kim, Byeong-Kwon Ju, and Jae-Min Hong. Flash-induced nanowelding of silver nanowire networks for transparent stretchable electrochromic devices. *Scientific Reports*, 8(1):2763, dec 2018.

[37] Thomas Sannicolo, Mélanie Lagrange, Anthony Cabos, Caroline Celle, Jean-Pierre Simonato, and Daniel Bellet. Metallic Nanowire-Based Transparent Electrodes for Next Generation Flexible Devices: a Review. *Small*, 12(44):6052–6075, nov 2016.

[38] Jatin J. Patil, Woo Hyun Chae, Adam Trebach, Ki-Jana Carter, Eric Lee, Thomas Sannicolo, and Jeffrey C. Grossman. Failing Forward: Stability of Transparent Electrodes Based on Metal Nanowire Networks. *Advanced Materials*, 33(5):2004356, feb 2021.

[39] Paul Delahay, Marcel Pourbaix, and Pierre Van Rysselberghe. Potential-pH Diagram of Silver Construction of the Diagram—Its Applications to the Study of the Properties of the Metal, its Compounds, and its Corrosion. *Journal of The Electrochemical Society*, 98(2):65, feb 1951.

[40] Christofer Leygraf, Inger Odnevall Wallinder, Johan Tidblad, and Thomas Graedel. *Atmospheric Corrosion: Second Edition*. Wiley Blackwell, jun 2016.

[41] Jose Luis Elechiguerra, Leticia Larios-Lopez, Cui Liu, Domingo Garcia-Gutierrez, Alejandra Camacho-Bragado, and Miguel Jose Yacaman. Corrosion at the Nanoscale: The Case of Silver Nanowires and Nanoparticles. *Chemistry of Materials*, 17(24):6042–6052, 2005.

[42] Gabriele Saleh, Chen Xu, and Stefano Sanvito. Silver Tarnishing Mechanism Revealed by Molecular Dynamics Simulations. *Angewandte Chemie*, 131(18):6078–6082, apr 2019.

[43] J.P. Franey, G.W. Kammlott, and T.E. Graedel. The corrosion of silver by atmospheric sulfurous gases. *Corrosion Science*, 25(2):133–143, jan 1985.

[44] Seong Heon Kim, Woon Ih Choi, Kwang Hee Kim, Dae Jin Yang, Sung Heo, and Dong-Jin Yun. Nanoscale Chemical and Electrical Stabilities of Graphene-covered Silver Nanowire Networks for Transparent Conducting Electrodes. *Scientific Reports*, 6(1):33074, dec 2016.

[45] Woo Hyun Chae, Thomas Sannicolo, and Jeffrey C. Grossman. Double-Sided Graphene Oxide Encapsulated Silver Nanowire Transparent Electrode with Improved Chemical and Electrical Stability. *ACS Applied Materials and Interfaces*, 12(15):17909–17920, apr 2020.

[46] Yumi Ahn, Youngjun Jeong, and Youngu Lee. Improved Thermal Oxidation Stability of Solution-Processable Silver Nanowire Transparent Electrode by Reduced Graphene Oxide. *ACS Applied Materials Interfaces*, 4(12):6410–6414, dec 2012.

[47] S. Chen, L. Song, Z. Tao, X. Shao, Y. Huang, Q. Cui, and X. Guo. Neutral-pH PEDOT:PSS as over-coating layer for stable silver nanowire flexible transparent conductive films. *Organic Electronics*, 15(12):3654–3659, dec 2014.

[48] Céline Mayousse, Caroline Celle, Alexandra Fraczkiewicz, and Jean-Pierre Simonato. Stability of silver nanowire based electrodes under environmental and electrical stresses. *Nanoscale*, 7(5):2107–2115, jan 2015.

[49] M. E. Toimil Molares, A. G. Balogh, T. W. Cornelius, R. Neumann, and C. Trautmann. Fragmentation of nanowires driven by Rayleigh instability. *Applied Physics Letters*, 85(22):5337–5339, nov 2004.

[50] Robert W. Balluffi, Samuel M. Allen, and W. Craig Carter. *Kinetics of Materials*. John Wiley Sons, Ltd, Hoboken, 2005.

[51] Thomas Sannicolo, Nicolas Charvin, Lionel Flandin, Silas Kraus, Dorina T. Papanastasiou, Caroline Celle, Jean-Pierre Simonato, David Muñoz-Rojas, Carmen Jiménez, and Daniel Bellet. Electrical Mapping of Silver Nanowire Networks: A Versatile Tool for Imaging Network Homogeneity and Degradation Dynamics during Failure. *ACS Nano*, 12(5):4648–4659, may 2018.

[52] Ritu Gupta, K. D. M. Rao, S. Kiruthika, and Giridhar U. Kulkarni. Visibly Transparent Heaters. *ACS Applied Materials Interfaces*, 8(20):12559–12575, may 2016.

[53] Yang Li, Peng Cui, Luyang Wang, Hanleem Lee, Keunsik Lee, and Hyoyoung Lee. Highly Bendable, Conductive, and Transparent Film by an Enhanced Adhesion of Silver Nanowires. *ACS Applied Materials Interfaces*, 5(18):9155–9160, sep 2013.

[54] Failure criterion of silver nanowire electrodes on a polymer substrate for highly flexible devices. *Scientific Reports 2017 7:1*, 7(1):1–8, apr 2017.

[55] Sankar Narayanan, Guangming Cheng, Zhi Zeng, Yong Zhu, and Ting Zhu. Strain Hardening and Size Effect in Five-fold Twinned Ag Nanowires. *Nano Letters*, 15(6):4037–4044, jun 2015.

[56] Zhaoxuan Wu, Yong Wei Zhang, Mark H. Jhon, Huajian Gao, and David J. Srolovitz. Nanowire failure: Long = brittle and short = ductile. *Nano Letters*, 12(2):910–914, feb 2012.

[57] Joo Young Jung, Nadeem Qaiser, Gang Feng, Byung Il Hwang, Taegeon Kim, Jae Hyun Kim, and Seung Min Han. Size-dependent hardness of five-fold twin structured Ag nanowires. *Physical Chemistry Chemical Physics*, 19(2):1311–1319, jan 2017.

[58] Hye Young Kim, Jae Yeon Kim, Ki Tae Yoo, Won Jon Yang, and Jai Won Byeon. Failure mechanism of Ag nanowire-coated conductive transparent electrode for wearable devices under folding and torsional fatigue condition. *Microelectronics Reliability*, 88-90:345–349, sep 2018.

[59] Bin Wu, Andreas Heidelberg, John J. Boland, John E. Sader, Xiao Ming Sun, and Ya Dong Li. Microstructure-hardened silver nanowires. *Nano Letters*, 6(3):468–472, mar 2006.

[60] Changmin Lee, Hyoungsub Kim, and Byungil Hwang. Fracture behavior of metal oxide/silver nanowire composite electrodes under cyclic bending. *Journal of Alloys and Compounds*, 773:361–366, jan 2019.

[61] Neng Ye, Jielin Yan, Shuang Xie, Yuhan Kong, Tao Liang, Hongzheng Chen, and Mingsheng Xu. Silver nanowire–graphene hybrid transparent conductive electrodes for highly efficient inverted organic solar cells. *Nanotechnology*, 28(30):305402, jul 2017.

[62] Highly stable and flexible silver nanowire–graphene hybrid transparent conducting electrodes for emerging optoelectronic devices. *Nanoscale*, 5(17):7750, aug 2013.

[63] Yumi Ahn, Youngjun Jeong, Donghwa Lee, and Youngu Lee. Copper nanowire-graphene core-shell nanostructure for highly stable transparent conducting electrodes. *ACS Nano*, 9(3):3125–3133, mar 2015.

[64] Hyunwoo Kim, Yutaka Miura, and Christopher W. Macosko. Graphene/Polyurethane Nanocomposites for Improved Gas Barrier and Electrical Conductivity. *Chemistry of Materials*, 22(11):3441–3450, jun 2010.

[65] Changwook Jeong, Pradeep Nair, Mohammad Khan, Mark Lundstrom, and Muhammad A. Alam. Prospects for Nanowire-Doped Polycrystalline Graphene

Films for Ultratransparent, Highly Conductive Electrodes. *Nano Letters*, 11(11):5020–5025, nov 2011.

[66] Neng Ye, Tao Liang, Lingling Zhan, Yuhan Kong, Shuang Xie, Xiangyang Ma, Hongzheng Chen, Huanxing Su, and Mingsheng Xu. High-Performance Bendable Organic Solar Cells With Silver Nanowire-Graphene Hybrid Electrode. *IEEE Journal of Photovoltaics*, 9(1):214–219, 2019.

[67] Areum Kim, Yulim Won, Kyoohee Woo, Chul-Hong Kim, and Jooho Moon. Highly Transparent Low Resistance ZnO/Ag Nanowire/ZnO Composite Electrode for Thin Film Solar Cells. *ACS Nano*, 7(2):1081–1091, feb 2013.

[68] Afzal Khan, Viet Huong Nguyen, David Muñoz-Rojas, Sara Aghazadehchors, Carmen Jiménez, Ngoc Duy Nguyen, and Daniel Bellet. Stability Enhancement of Silver Nanowire Networks with Conformal ZnO Coatings Deposited by Atmospheric Pressure Spatial Atomic Layer Deposition. *ACS Applied Materials Interfaces*, 10(22):19208–19217, jun 2018.

[69] M Lagrange, T Sannicolo, D. Munoz-Rojas, B Guillo Lohan, A Khan, M Anikin, C Jiménez, F Bruckert, Y Bréchet, and D Bellet. Understanding the mechanisms leading to failure in metallic nanowire-based transparent heaters, and solution for stability enhancement. *Nanotechnology*, 28(5):055709, feb 2017.

[70] Josef Mock, Marco Bobinger, Christian Bogner, Paolo Lugli, and Markus Becherer. Aqueous Synthesis, Degradation, and Encapsulation of Copper Nanowires for Transparent Electrodes. *Nanomaterials*, 8(10):767, sep 2018.

[71] Manuela Göbelt, Ralf Keding, Sebastian W. Schmitt, Björn Hoffmann, Sara Jäckle, Michael Latzel, Vuk V. Radmilović, Velimir R. Radmilović, Erdmann Spiecker, and Silke Christiansen. Encapsulation of silver nanowire networks by atomic layer deposition for indium-free transparent electrodes. *Nano Energy*, 16:196–206, sep 2015.

[72] Sung Hyun Park, Sang Mok Lee, Eun Hye Ko, Tae Ho Kim, Yoon Chae Nah, Sang Jin Lee, Jae Heung Lee, and Han Ki Kim. Roll-to-Roll sputtered ITO/Cu/ITO multilayer electrode for flexible, transparent thin film heaters and electrochromic applications. *Scientific Reports*, 6, sep 2016.

[73] David Muñoz-Rojas, Viet Huong Nguyen, César Masse de la Huerta, Carmen Jiménez, and Daniel Bellet. Spatial Atomic Layer Deposition. In *Chemical Vapor Deposition for Nanotechnology*. IntechOpen, jan 2019.

[74] Jinwook Kim, Dan Ouyang, Haifei Lu, Fei Ye, Yuwei Guo, Ni Zhao, and Wallace C.H. Choy. High Performance Flexible Transparent Electrode via One-Step Multifunctional Treatment for Ag Nanonetwork Composites Semi-Embedded in Low-Temperature-Processed Substrate for Highly Performed Organic Photovoltaics. *Advanced Energy Materials*, 10(15):1903919, apr 2020.

[75] Communication Feng Xu, Yong Zhu, Y Zhu, and F Xu. Highly Conductive and Stretchable Silver Nanowire Conductors. *Advanced Materials*, 24(37):5117–5122, sep 2012.

[76] Haifei Lu, Di Zhang, Xingang Ren, Jian Liu, and Wallace C.H. Choy. Selective growth and integration of silver nanoparticles on silver nanowires at room conditions for transparent nano-network electrode. *ACS Nano*, 8(10):10980–10987, oct 2014.

[77] Philipp Maisch, Kai Cheong Tam, Luca Lucera, Hans Joachim Egelhaaf, Horst Scheiber, Eugen Maier, and Christoph J. Brabec. Inkjet printed silver nanowire percolation networks as electrodes for highly efficient semitransparent organic solar cells. *Organic Electronics*, 38:139–143, nov 2016.

[78] Zuofeng Chen, Shengrong Ye, Ian E. Stewart, and Benjamin J. Wiley. Copper nanowire networks with transparent oxide shells that prevent oxidation without reducing transmittance. *ACS Nano*, 8(9):9673–9679, sep 2014.

[79] Yang Zhao, Xijun Wang, Shize Yang, Elisabeth Kuttner, Aidan A. Taylor, Reza Salemmilani, Xin Liu, Martin Moskovits, Binghui Wu, Ahmad Dehestani, Jian-Feng Li, Matthew F. Chisholm, Zhong-Qun Tian, Feng-Ru Fan, Jun Jiang, and Galen D. Stucky. Protecting the Nanoscale Properties of Ag Nanowires with a Solution-Grown SnO 2 Monolayer as Corrosion Inhibitor. *Journal of the American Chemical Society*, 141(35):jacs.9b07172, sep 2019.

[80] Ian E Stewart, Aaron R Rathmell, Liang Yan, Shengrong Ye, Patrick F Flowers, Wei You, and Benjamin J Wiley. Solution-processed copper-nickel nanowire anodes for organic solar cells. *Nanoscale*, 6(11):5980–5988, 2014.

[81] William S. Hummers and Richard E. Offeman. Preparation of Graphitic Oxide. *Journal of the American Chemical Society*, 80(6):1339–1339, mar 1958.

[82] Anton Lerf, Heyong He, Michael Forster, and Jacek Klinowski. Structure of Graphite Oxide Revisited‖. *Journal of Physical Chemistry B*, 102(23):4477–4482, jun 1998.

[83] Songfeng Pei and Hui-Ming Cheng. The reduction of graphene oxide. *Carbon*, 50(9):3210–3228, aug 2012.

[84] L. G. Guex, B. Sacchi, K. F. Peuvot, R. L. Andersson, A. M. Pourrahimi, V. Ström, S. Farris, and R. T. Olsson. Experimental review: chemical reduction of graphene oxide (GO) to reduced graphene oxide (rGO) by aqueous chemistry. *Nanoscale*, 9(27):9562–9571, jul 2017.

[85] Jiajie Liang, Lu Li, Kwing Tong, Zhi Ren, Wei Hu, Xiaofan Niu, Yongsheng Chen, and Qibing Pei. Silver Nanowire Percolation Network Soldered with Graphene Oxide at Room Temperature and Its Application for Fully Stretchable Polymer Light-Emitting Diodes. *ACS Nano*, 8(2):1590–1600, feb 2014.

[86] In Kyu Moon, Jae Il Kim, Hanleem Lee, Kangheon Hur, Woon Chun Kim, and Hyoyoung Lee. 2D Graphene Oxide Nanosheets as an Adhesive Over-Coating Layer for Flexible Transparent Conductive Electrodes. *Scientific Reports*, 3(1):1112, dec 2013.

[87] Chunhui Wu, Jinting Jiu, Teppei Araki, Hirotaka Koga, Tsuyoshi Sekitani, Hao Wang, and Katsuaki Suganuma. Rapid self-assembly of ultrathin graphene oxide film and application to silver nanowire flexible transparent electrodes. *RSC Advances*, 6(19):15838–15845, feb 2016.

[88] Yang Li, Peng Cui, Luyang Wang, Hanleem Lee, Keunsik Lee, and Hyoyoung Lee. Highly Bendable, Conductive, and Transparent Film by an Enhanced Adhesion of Silver Nanowires. *ACS Applied Materials and Interfaces*, 5(18):9155–9160, sep 2013.

[89] B. Tugba Camic, Faruk Oytun, M. Hasan Aslan, Hee Jeong Shin, Hyosung Choi, and Fevzihan Basarir. Fabrication of a transparent conducting electrode based on graphene/silver nanowires via layer-by-layer method for organic photovoltaic devices. *Journal of Colloid and Interface Science*, 505:79–86, nov 2017.

[90] Iskandar N. Kholmanov, Meryl D. Stoller, Jonathan Edgeworth, Wi Hyoung Lee, Huifeng Li, Jongho Lee, Craig Barnhart, Jeffrey R. Potts, Richard Piner, Deji Akinwande, Jeffrey E. Barrick, and Rodney S. Ruoff. Nanostructured Hybrid Transparent Conductive Films with Antibacterial Properties. *ACS Nano*, 6(6):5157–5163, jun 2012.

[91] B.Hwang, M.Park, T.Kim, and S. M.Han. Effect of RGO deposition on chemical and mechanical reliability of Ag nanowire flexible transparent electrode. *RSC Advances*, 6(71):67389–67395, jul 2016.

[92] Alessandro Aliprandi, Tiago Moreira, Cosimo Anichini, Marc-Antoine Stoeckel, Matilde Eredia, Ugo Sassi, Matteo Bruna, Carlos Pinheiro, César A. T. Laia, Sara Bonacchi, and Paolo Samorì. Hybrid Copper-Nanowire-Reduced-Graphene-Oxide Coatings: A "Green Solution" Toward Highly Transparent, Highly Conductive, and Flexible Electrodes for (Opto)Electronics. *Advanced Materials*, 29(41):1703225, nov 2017.

[93] Letian Dou, Fan Cui, Yi Yu, Garo Khanarian, Samuel W. Eaton, Qin Yang, Joaquin Resasco, Christian Schildknecht, Kerstin Schierle-Arndt, and Peidong Yang. Solution-Processed Copper/Reduced-Graphene-Oxide Core/Shell Nanowire Transparent Conductors. *ACS Nano*, 10(2):2600–2606, feb 2016.

[94] Jihyeon Kim, Ju Won Lim, Filipe Marques Mota, Ji-Eun Lee, Ramireddy Boppella, Keun Yong Lim, Kyungkon Kim, Won Kook Choi, and Dong Ha Kim. Reduced graphene oxide wrapped core–shell metal nanowires as promising flexible transparent conductive electrodes with enhanced stability. *Nanoscale*, 8(45):18938–18944, nov 2016.

[95] Goki Eda, Giovanni Fanchini, and Manish Chhowalla. Large-area ultrathin films of reduced graphene oxide as a transparent and flexible electronic material. *Nature Nanotechnology*, 3(5):270–274, may 2008.

[96] Byung Min Yoo, Hye Jin Shin, Hee Wook Yoon, and Ho Bum Park. Graphene and graphene oxide and their uses in barrier polymers. *Journal of Applied Polymer Science*, 131(1):39628, jan 2014.

[97] Hadi Hosseinzadeh Khaligh and Irene A Goldthorpe. Failure of silver nanowire transparent electrodes under current flow. *Nanoscale Research Letters*, 8(1), 2013.

[98] Haifei Lu, Di Zhang, Jiaqi Cheng, Jian Liu, Jian Mao, and Wallace C.H. Choy. Locally Welded Silver Nano-Network Transparent Electrodes with High Operational Stability by a Simple Alcohol-Based Chemical Approach. *Advanced Functional Materials*, 25(27):4211–4218, jul 2015.

[99] Chih Hung Tsai, Sui Ying Hsu, Tsung Wei Huang, Yu Tang Tsai, Yan Fang Chen, Yuan Hsuan Jhang, Lun Hsieh, Chung Chih Wu, Yen Shan Chen, Chieh Wei Chen, and Chung Chun Li. Influences of textures in fluorine-doped tin oxide on characteristics of dye-sensitized solar cells. *Organic Electronics*, 12(12):2003–2011, dec 2011.

[100] Caroline Celle, Anthony Cabos, Thomas Fontecave, Bruno Laguitton, Anass Benayad, Laure Guettaz, Nathalie Pélissier, Viet Huong Nguyen, Daniel Bellet, David Muñoz-Rojas, and Jean-Pierre Simonato. Oxidation of copper nanowire based transparent electrodes in ambient conditions and their stabilization by encapsulation: application to transparent film heaters. *Nanotechnology*, 29(8):085701, feb 2018.

[101] Yulim Won, Areum Kim, Donggyu Lee, Wooseok Yang, Kyoohee Woo, Sunho Jeong, and Jooho Moon. Annealing-free fabrication of highly oxidation-resistive copper nanowire composite conductors for photovoltaics. *NPG Asia Materials*, 6(6):e105, jun 2014.

[102] H H Khaligh, L Xu, A Khosropour, A Madeira, M Romano, C Pradére, M Tréguer-Delapierre, L Servant, M A Pope, and I A Goldthorpe. The Joule heating problem in silver nanowire transparent electrodes. *Nanotechnology*, 28(42):425703, oct 2017.

[103] Yue Chau Garen Kwan, Quang Luan Le, and Cheng Hon Alfred Huan. Time to failure modeling of silver nanowire transparent conducting electrodes and effects of a reduced graphene oxide over layer. *Solar Energy Materials and Solar Cells*, 144:102–108, jan 2016.

[104] Yanzhe Zhu, Tao Wan, Peiyuan Guan, Yutao Wang, Tom Wu, Zhaojun Han, Genchu Tang, and Dewei Chu. Improving thermal and electrical stability of

silver nanowire network electrodes through integrating graphene oxide intermediate layers. *Journal of Colloid and Interface Science*, 566:375–382, apr 2020.

[105] A. Alhadhrami, S. Salgado, and V. Maheshwari. Thermal reduction to control the spacing in graphene oxide membranes: effect on ion diffusion and electrical conduction. *RSC Advances*, 6(74):70012–70017, jul 2016.

[106] Li Chiang Lin and Jeffrey C. Grossman. Atomistic understandings of reduced graphene oxide as an ultrathin-film nanoporous membrane for separations. *Nature Communications 2015 6:1*, 6(1):1–7, sep 2015.

[107] Thomas Sannicolo, Woo Hyun Chae, Jeremiah Mwaura, Vladimir Bulović, and Jeffrey C. Grossman. Silver Nanowire Back Electrode Stabilized with Graphene Oxide Encapsulation for Inverted Semitransparent Organic Solar Cells with Longer Lifetime. *ACS Applied Energy Materials*, 4(2):1431–1441, feb 2021.

[108] Yi-Ting Lai and Nyan-Hwa Tai. One-Step Process for High-Performance, Adhesive, Flexible Transparent Conductive Films Based on p-Type Reduced Graphene Oxides and Silver Nanowires. *ACS Applied Materials Interfaces*, 7(33):18553–18559, aug 2015.

[109] Faisal Alotaibi, Tran Thanh Tung, Md Julker Nine, Campbell J. Coghlan, and Dusan Losic. Silver Nanowires with Pristine Graphene Oxidation Barriers for Stable and High Performance Transparent Conductive Films. *ACS Applied Nano Materials*, 1(5):2249–2260, may 2018.

[110] Firuze Soltani-kordshuli, Fatemeh Zabihi, and Morteza Eslamian. Graphene-doped PEDOT:PSS nanocomposite thin films fabricated by conventional and substrate vibration-assisted spray coating (SVASC). *Engineering Science and Technology, an International Journal*, 19(3):1216–1223, sep 2016.

[111] Hee Jin Lee, Ye Seul Song, Tae Kyu An, Won Kook Choi, and Sung Ryong Kim. Ultrasmooth transparent conductive hybrid films of reduced graphene oxide and single-walled carbon nanotube by ultrasonic spraying. *Synthetic Metals*, 221:340–344, nov 2016.

[112] Hongcheng Lian, Lehua Qi, Jun Luo, and Kewen Hu. Experimental study and mechanism analysis on the effect of substrate wettability on graphene sheets distribution morphology within uniform printing droplets. *Journal of Physics: Condensed Matter*, 30(33):335001, aug 2018.

[113] Saad A. Hasan, John L. Rigueur, Robert R. Harl, Alex J. Krejci, Isabel Gonzalo-Juan, Bridget R. Rogers, and James H. Dickerson. Transferable Graphene Oxide Films with Tunable Microstructures. *ACS Nano*, 4(12):7367–7372, dec 2010.

[114] Mani Diba, Derrick W.H. Fam, Aldo R. Boccaccini, and Milo S.P. Shaffer. Electrophoretic deposition of graphene-related materials: A review of the fundamentals. *Progress in Materials Science*, 82:83–117, sep 2016.

[115] Saad A. Hasan, Dustin W. Kavich, and James H. Dickerson. Sacrificial layer electrophoretic deposition of free-standing multilayered nanoparticle films. *Chemical Communications*, 0(25):3723, jun 2009.

[116] Mani Diba, Ainara García-Gallastegui, Robin N. Klupp Taylor, Fatemeh Pishbin, Mary P. Ryan, Milo S.P. Shaffer, and Aldo R. Boccaccini. Quantitative evaluation of electrophoretic deposition kinetics of graphene oxide. *Carbon*, 67:656–661, feb 2014.

[117] H. C. Hamaker. Formation of a deposit by electrophoresis. *Transactions of the Faraday Society*, 35(0):279, jan 1940.

[118] Laxmidhar Besra and Meilin Liu. A review on fundamentals and applications of electrophoretic deposition (EPD). *Progress in Materials Science*, 52(1):1–61, jan 2007.

[119] Yi Jui Huang, Chun Han Lai, and Pu Wei Wu. Fabrication of large-area colloidal crystals by electrophoretic deposition in vertical arrangement. *Electrochemical and Solid-State Letters*, 11(12), 2008.

[120] Dong Kyu Lee, Seon Joon Kim, Yong-Jae Kim, Hyunji Choi, Dae Woo Kim, Hwan-Jin Jeon, Chi Won Ahn, Jae W. Lee, and Hee-Tae Jung. Graphene Oxide/Carbon Nanotube Bilayer Flexible Membrane for High-Performance Li–S Batteries with Superior Physical and Electrochemical Properties. *Advanced Materials Interfaces*, 6(7):1801992, apr 2019.

[121] Yuxiang Zhong, Xin Zhang, Yi He, Huifen Peng, Gongkai Wang, and Guoqing Xin. Simultaneously Armored and Active Graphene for Transparent and Flexible Supercapacitors. *Advanced Functional Materials*, page 1801998, may 2018.

[122] Pradip Kumar, Faisal Shahzad, Soon Man Hong, and Chong Min Koo. A flexible sandwich graphene/silver nanowires/graphene thin film for high-performance electromagnetic interference shielding. *RSC Advances*, 6(103):101283–101287, oct 2016.

[123] Owen C. Compton, Steven W. Cranford, Karl W. Putz, Zhi An, L. Catherine Brinson, Markus J. Buehler, and SonBinh T. Nguyen. Tuning the Mechanical Properties of Graphene Oxide Paper and Its Associated Polymer Nanocomposites by Controlling Cooperative Intersheet Hydrogen Bonding. *ACS Nano*, 6(3):2008–2019, mar 2012.

[124] Fei Guo, Hamed Azimi, Yi Hou, Thomas Przybilla, Mengyao Hu, Carina Bronnbauer, Stefan Langner, Erdmann Spiecker, Karen Forberich, and Christoph J. Brabec. High-performance semitransparent perovskite solar cells with solution-processed silver nanowires as top electrodes. *Nanoscale*, 7(5):1642–1649, feb 2015.

[125] Jiajie Liang, Lu Li, Xiaofan Niu, Zhibin Yu, and Qibing Pei. Elastomeric polymer light-emitting devices and displays. *Nature Photonics*, 7(10):817–824, oct 2013.

[126] Vijay Kumar Kaushik. XPS core level spectra and Auger parameters for some silver compounds. *Journal of Electron Spectroscopy and Related Phenomena*, 56(3):273–277, jun 1991.

[127] Qu Jiangying, Gao Feng, Zhou Quan, Wang Zhiyu, Hu Han, Li Beibei, Wan Wubo, Wang Xuzhen, and Qiu Jieshan. Highly atom-economic synthesis of graphene/Mn3O4 hybrid composites for electrochemical supercapacitors. *Nanoscale*, 5(7):2999, mar 2013.

[128] Y. Su, V. G. Kravets, S. L. Wong, J. Waters, A. K. Geim, and R. R. Nair. Impermeable barrier films and protective coatings based on reduced graphene oxide. *Nature Communications*, 5(1):4843, dec 2014.

[129] You-Hao Yang, Laura Bolling, Morgan A. Priolo, and Jaime C. Grunlan. Super Gas Barrier and Selectivity of Graphene Oxide-Polymer Multilayer Thin Films. *Advanced Materials*, 25(4):503–508, jan 2013.

[130] Xiang-Rong Yu, Fen Liu, Zhong-Yan Wang, and Ying Chen. Auger parameters for sulfur-containing compounds using a mixed aluminum-silver excitation source. *Journal of Electron Spectroscopy and Related Phenomena*, 50(2):159–166, jan 1990.

[131] Brian R. Strohmeier and David M. Hercules. Surface spectroscopic characterization of manganese/aluminum oxide catalysts. *The Journal of Physical Chemistry*, 88(21):4922–4929, oct 1984.

[132] Sophie Sorel, Daniel Bellet, and Jonathan N Coleman. Relationship between Material Properties and Transparent Heater Performance for Both Bulk-like and Percolative Nanostructured Networks. *ACS Nano*, 8(5):4805–4814, may 2014.

[133] Viet Huong Nguyen, Joao Resende, Dorina T. Papanastasiou, Nil Fontanals, Carmen Jiménez, David Muñoz-Rojas, and Daniel Bellet. Low-cost fabrication of flexible transparent electrodes based on Al doped ZnO and silver nanowire nanocomposites: impact of the network density. *Nanoscale*, 11(25):12097–12107, jun 2019.

[134] Changhong Cao, Matthew Daly, Brandon Chen, Jane Y. Howe, Chandra Veer Singh, Tobin Filleter, and Yu Sun. Strengthening in Graphene Oxide Nanosheets: Bridging the Gap between Interplanar and Intraplanar Fracture. *Nano Letters*, 15(10):6528–6534, oct 2015.

[135] Hadi Hosseinzadeh Khaligh and Irene A Goldthorpe. Hot-rolling nanowire transparent electrodes for surface roughness minimization. *Nanoscale Research Letters*, 9(1):310, dec 2014.

[136] Oleksandr M. Slobodian, Peter M. Lytvyn, Andrii S. Nikolenko, Victor M. Naseka, Oleg Yu. Khyzhun, Andrey V. Vasin, Stanislav V. Sevostianov, and Alexei N. Nazarov. Low-Temperature Reduction of Graphene Oxide: Electrical Conductance and Scanning Kelvin Probe Force Microscopy. *Nanoscale Research Letters*, 13(1):139, dec 2018.

[137] Alexey Lipatov, Maxime J.-F. Guinel, Dmitry S. Muratov, Vladislav O. Vanyushin, Peter M. Wilson, Andrei Kolmakov, and Alexander Sinitskii. Low-temperature thermal reduction of graphene oxide: In situ correlative structural, thermal desorption, and electrical transport measurements. *Applied Physics Letters*, 112(5):053103, jan 2018.

[138] Chun Kiang Chua and Martin Pumera. Renewal of sp2 bonds in graphene oxides via dehydrobromination. *Journal of Materials Chemistry*, 22(43):23227–23231, oct 2012.

[139] Wenxia Zhang, Wei Song, Jiaming Huang, Like Huang, Tingting Yan, Jinfeng Ge, Ruixiang Peng, and Ziyi Ge. Graphene:silver nanowire composite transparent electrode based flexible organic solar cells with 13.4 *J. Mater. Chem. A*, 7(38):22021–22028, 2019.

[140] Antonio Gaetano Ricciardulli, Sheng Yang, Gert-Jan A. H. Wetzelaer, Xinliang Feng, and Paul W. M. Blom. Hybrid Silver Nanowire and Graphene-Based Solution-Processed Transparent Electrode for Organic Optoelectronics. *Advanced Functional Materials*, 28(14):1706010, apr 2018.

[141] Anna Håkansson, Shaobo Han, Suhao Wang, Jun Lu, Slawomir Braun, Mats Fahlman, Magnus Berggren, Xavier Crispin, and Simone Fabiano. Effect of (3-glycidyloxypropyl)trimethoxysilane (GOPS) on the electrical properties of PEDOT:PSS films. *Journal of Polymer Science Part B: Polymer Physics*, 55(10):814–820, may 2017.

[142] Byung Yong Wang, Eung Seok Lee, Young Jei Oh, and Hyun Wook Kang. A silver nanowire mesh overcoated protection layer with graphene oxide as a transparent electrode for flexible organic solar cells. *RSC Advances*, 7(83):52914–52922, nov 2017.

[143] Fei Guo, Xiangdong Zhu, Karen Forberich, Johannes Krantz, Tobias Stubhan, Michael Salinas, Marcus Halik, Stefanie Spallek, Benjamin Butz, Erdmann Spiecker, Tayebeh Ameri, Ning Li, Peter Kubis, Dirk M. Guldi, Gebhard J. Matt, and Christoph J. Brabec. ITO-Free and Fully Solution-Processed Semitransparent Organic Solar Cells with High Fill Factors. *Advanced Energy Materials*, 3(8):1062–1067, aug 2013.

[144] George Y Margulis, M Greyson Christoforo, David Lam, Zach M Beiley, Andrea R Bowring, Colin D Bailie, Alberto Salleo, and Michael D McGehee. Spray Deposition of Silver Nanowire Electrodes for Semitransparent Solid-State Dye-Sensitized Solar Cells. *Advanced Energy Materials*, 3(12):1657–1663, 2013.

[145] Myungkwan Song, Dae Sung You, Kyounga Lim, Sujin Park, Sunghoon Jung, Chang Su Kim, Dong Ho Kim, Do Geun Kim, Jongk Kuk Kim, Juyun Park, Yong Cheol Kang, Jinhee Heo, Sung Ho Jin, Jong Hyun Park, and Jae Wook Kang. Highly Efficient and Bendable Organic Solar Cells with Solution-Processed Silver Nanowire Electrodes. *Advanced Functional Materials*, 23(34):4177–4184, sep 2013.

[146] Hisato Yamaguchi, Jimmy Granstrom, Wanyi Nie, Hossein Sojoudi, Takeshi Fujita, Damien Voiry, Mingwei Chen, Gautam Gupta, Aditya D. Mohite, Samuel Graham, and Manish Chhowalla. Reduced Graphene Oxide Thin Films as Ultrabarriers for Organic Electronics. *Advanced Energy Materials*, 4(4):1300986, mar 2014.

[147] T Kim, J H Kang, S J Yang, S J Sung, Y S Kim, and C R Park. Facile preparation of reduced graphene oxide-based gas barrier films for organic photovoltaic devices. *Energy Environmental Science*, 7(10):3403–3411, 2014.

[148] Saqib Rafique, Shahino Mah Abdullah, Khaulah Sulaiman, and Mitsumasa Iwamoto. Fundamentals of bulk heterojunction organic solar cells: An overview of stability/degradation issues and strategies for improvement. *Renewable and Sustainable Energy Reviews*, 84:43–53, 2018.

[149] Danfeng Pu, Weixin Zhou, Yi Li, Jun Chen, Jianyu Chen, Hongmei Zhang, Baoxiu Mi, Lianhui Wang, and Yanwen Ma. Order-enhanced silver nanowire networks fabricated by two-step dip-coating as polymer solar cell electrodes. *RSC Advances*, 5(122):100725–100729, nov 2015.

[150] Meng Hu and Baoxia Mi. Layer-by-layer assembly of graphene oxide membranes via electrostatic interaction. *Journal of Membrane Science*, 469:80–87, nov 2014.

[151] Gil Gonçalves, Mercedes Vila, Igor Bdikin, Alicia de Andrés, Nazanin Emami, Rute A. S. Ferreira, Luís D. Carlos, José Grácio, and Paula A. A. P. Marques. Breakdown into nanoscale of graphene oxide: Confined hot spot atomic reduction and fragmentation. *Scientific Reports 2014 4:1*, 4(1):1–8, oct 2014.

[152] Brian R. Coleman, Timothy Knight, Valerie Gies, Zygmunt J. Jakubek, and Shan Zou. Manipulation and Quantification of Graphene Oxide Flake Size: Photoluminescence and Cytotoxicity. *ACS Applied Materials and Interfaces*, 9(34):28911–28921, aug 2017.

[153] Kouji Fujimoto, Shiro Fujita, Bin Ding, and Seimei Shiratori. Fabrication of layer-by-layer self-Assembly films using roll-to-roll process. *Japanese Journal of Applied Physics, Part 2: Letters*, 44(1-7):L126, dec 2005.

[154] Hyeon-Jin Shin, Ki Kang Kim, Anass Benayad, Seon-Mi Yoon, Hyeon Ki Park, In-Sun Jung, Mei Hua Jin, Hae-Kyung Jeong, Jong Min Kim, Jae-Young Choi,

and Young Hee Lee. Efficient Reduction of Graphite Oxide by Sodium Borohydride and Its Effect on Electrical Conductance. *Advanced Functional Materials*, 19(12):1987–1992, jun 2009.

[155] A. R. Khoei and M. S. Khorrami. Mechanical properties of graphene oxide: A molecular dynamics study. *Fullerenes, Nanotubes and Carbon Nanostructures*, 24(9):594–603, sep 2016.

[156] Ruiyi Chen, Suprem R. Das, Changwook Jeong, Mohammad Ryyan Khan, David B. Janes, and Muhammad A. Alam. Co-Percolating Graphene-Wrapped Silver Nanowire Network for High Performance, Highly Stable, Transparent Conducting Electrodes. *Advanced Functional Materials*, 23(41):5150–5158, nov 2013.

[157] Zheng Cui, Felipe Robles Poblete, and Yong Zhu. Tailoring the Temperature Coefficient of Resistance of Silver Nanowire Nanocomposites and their Application as Stretchable Temperature Sensors. *ACS Applied Materials and Interfaces*, 11(19):17836–17842, may 2019.

[158] F. A. Nichols and W. W. Mullins. Morphological Changes of a Surface of Revolution due to Capillarity-Induced Surface Diffusion. *Journal of Applied Physics*, 36(6):1826, jul 1965.

[159] Simon Vigonski, Ville Jansson, Sergei Vlassov, Boris Polyakov, Ekaterina Baibuz, Sven Oras, Alvo Aabloo, Flyura Djurabekova, and Vahur Zadin. Au nanowire junction breakup through surface atom diffusion. *Nanotechnology*, 29(1):015704, dec 2017.

[160] Abhinav Roy, Arjun Varma R., and M. P. Gururajan. Phase-field study of surface diffusion enhanced break-ups of nanowire junctions. *Journal of Applied Physics*, 130(19):194301, nov 2021.

[161] Ganesh Ananthakrishnan, Mitisha Surana, Matthew Poss, Jad Jean Yaacoub, Kaihao Zhang, Nikhil Admal, Pascal Pochet, Sameh Tawfick, and Harley T. Johnson. Graphene-mediated stabilization of surface facets on metal substrates. *Journal of Applied Physics*, 130(16):165302, oct 2021.

[162] Dorina T. Papanastasiou, Amélie Schultheiss, David Muñoz-Rojas, Caroline Celle, Alexandre Carella, Jean-Pierre Simonato, and Daniel Bellet. Transparent Heaters: A Review. *Advanced Functional Materials*, 30(21):1910225, may 2020.

[163] Xu Zhang, Xingbin Yan, Jiangtao Chen, and Jinping Zhao. Large-size graphene microsheets as a protective layer for transparent conductive silver nanowire film heaters. *Carbon*, 69:437–443, apr 2014.

[164] Yilong Huang, Yanhong Tian, Chunjin Hang, Yubin Liu, Shang Wang, Miaomiao Qi, He Zhang, and Jie Zhao. Self-Limited Nanosoldering of Silver Nanowires for High-Performance Flexible Transparent Heaters. *ACS Applied Materials and Interfaces*, 11(24):21850–21858, jun 2019.

[165] Byungil Hwang, Hae A.Seul Shin, Taegeon Kim, Young Chang Joo, and Seung Min Han. Highly Reliable Ag Nanowire Flexible Transparent Electrode with Mechanically Welded Junctions. *Small*, 10(16):3397–3404, aug 2014.

[166] Andreas Sandström and Ludvig Edman. Towards High-Throughput Coating and Printing of Light-Emitting Electrochemical Cells: A Review and Cost Analysis of Current and Future Methods. *Energy Technology*, 3(4):329–339, apr 2015.

[167] Yongjie Ge, Xidong Duan, Meng Zhang, Lin Mei, Jiawen Hu, Wei Hu, and Xiangfeng Duan. Direct Room Temperature Welding and Chemical Protection of Silver Nanowire Thin Films for High Performance Transparent Conductors. *Journal of the American Chemical Society*, 140(1):193–199, jan 2017.

[168] Pan Xue, Shuiren Liu, Xinlei Shi, Chuang Sun, Chao Lai, Ying Zhou, Dong Sui, Yongsheng Chen, Jiajie Liang, P Xue, S Liu, X Shi, J Liang, C Sun, C Lai, Y Zhou, D Sui, and Y Chen. A Hierarchical Silver-Nanowire–Graphene Host Enabling Ultrahigh Rates and Superior Long-Term Cycling of Lithium-Metal Composite Anodes. *Advanced Materials*, 30(44):1804165, nov 2018.

[169] Jaewon Kim, Min-Seob Kim, Youngseok Lee, Shin-Yeong Kim, Yung-Eun Sung, and Seung Hwan Ko. Hierarchically Structured Conductive Polymer Binders with Silver Nanowires for High-Performance Silicon Anodes in Lithium-Ion Batteries. *ACS Applied Materials Interfaces*, page acsami.2c00844, apr 2022.

[170] Phillip Won, Jung Jae Park, Taemin Lee, Inho Ha, Seonggeun Han, Mansoo Choi, Jinhwan Lee, Sukjoon Hong, Kyu Jin Cho, and Seung Hwan Ko. Stretchable and Transparent Kirigami Conductor of Nanowire Percolation Network for Electronic Skin Applications. *Nano Letters*, 19(9):6087–6096, sep 2019.

[171] Xingzhen Yan, Xu Li, Lu Zhou, Xuefeng Chu, Fan Yang, Yaodan Chi, and Xiaotian Yang. Electrically sintered silver nanowire networks for use as transparent electrodes and heaters. *Materials Research Express*, 6(11):116316, oct 2019.

[172] Faruk Oytun, Onur Alpturk, and Fevzihan Basarir. Coupling layer-by-layer assembly and multilayer transfer to fabricate flexible transparent film heater. *Materials Research Bulletin*, 112:53–60, apr 2019.

[173] Duckjong Kim, Lijing Zhu, Da Jeong Jeong, Kiyoung Chun, Yun Young Bang, Seung Ryeol Kim, Jae Hyun Kim, and Sang Keun Oh. Transparent flexible heater based on hybrid of carbon nanotubes and silver nanowires. *Carbon*, 63:530–536, nov 2013.

[174] Su Jeong Lee, Jong Woo Kim, Jung Hyuk Park, Yoann Porte, Jin Hoon Kim, Jin Woo Park, Sunghee Kim, and Jae Min Myoung. SWCNT–Ag nanowire composite for transparent stretchable film heater with enhanced electrical stability. *Journal of Materials Science*, 53(17):12284–12294, sep 2018.

[175] Gui-Shi Liu, Yuwang Xu, Yifei Kong, Li Wang, Ji Wang, Xi Xie, Yunhan Luo, and Bo-Ru Yang. Comprehensive Stability Improvement of Silver Nanowire Networks via Self-Assembled Mercapto Inhibitors. *ACS Applied Materials Interfaces*, 10(43):37699–37708, oct 2018.

[176] Kyoung hee Pyo and Jong Woong Kim. Transparent and mechanically robust flexible heater based on compositing of Ag nanowires and conductive polymer. *Composites Science and Technology*, 133:7–14, sep 2016.

[177] Xin He, Ruihui He, Qiuming Lan, Weijie Wu, Feng Duan, Jundong Xiao, Mei Zhang, Qingguang Zeng, Jianhao Wu, and Junyan Liu. Screen-Printed Fabrication of PEDOT:PSS/Silver Nanowire Composite Films for Transparent Heaters. *Materials 2017, Vol. 10, Page 220*, 10(3):220, feb 2017.

[178] Minghui Cao, Minqiang Wang, Le Li, Hengwei Qiu, and Zhi Yang. Effect of Graphene-EC on Ag NW-Based Transparent Film Heaters: Optimizing the Stability and Heat Dispersion of Films. *ACS Applied Materials and Interfaces*, 10(1):1077–1083, jan 2018.

[179] Chaewon Kim, Mi Jung Lee, Sung Jei Hong, Young Sung Kim, and Jae Yong Lee. A flexible transparent heater with ultrahigh thermal efficiency and fast thermal response speed based on a simple solution-processed indium tin oxide nanoparticles-silver nanowires composite structure on photo-polymeric film. *Composites Science and Technology*, 157:107–118, mar 2018.

[180] Seung-Bok Yang, HongKyw Choi, Da Som Lee, Choon-Gi Choi, Sung-Yool Choi, and Il-Doo Kim. Improved Optical Sintering Efficiency at the Contacts of Silver Nanowires Encapsulated by a Graphene Layer. *Small*, 11(11):1293–1300, mar 2015.

[181] Joon Min Lee, Young Hoi Kim, Han Ki Kim, Hye Jin Kim, and Chan Hwa Hong. Effect of AlOx protection layer on AgNWs for flexible transparent heater. *Scientific Reports*, 10(1):1–8, mar 2020.

[182] Juhyung Park, Dongjun Han, Seunghwan Choi, Yunkyung Kim, and Jeonghun Kwak. Flexible transparent film heaters using a ternary composite of silver nanowire, conducting polymer, and conductive oxide. *RSC Advances*, 9(10):5731–5737, feb 2019.

[183] Malkeshkumar Patel, Khushbu R. Chauhan, Joondong Kim, Jong Woong Kim, and Donggun Lim. AgNWs networks for high-performing transparent heaters by using NiO window layer. *Sensors and Actuators A: Physical*, 267:8–13, nov 2017.

[184] Runfei Wang, Peizhi Cai, Wei Xu, Ruiqin Tan, Wenfeng Shen, Zhaozhao Wang, Guofei Chen, Jian Huang, Xingzhong Fang, and Weijie Song. Highly flexible and transparent film heaters based on colorless polyimide substrate with a

GZO/AgNW/GZO sandwich structure. *Journal of Materials Science: Materials in Electronics*, 31(6):4743–4751, mar 2020.

[185] Shihui Yu, Xiaoyu Liu, Helei Dong, Xiaohu Wang, and Lingxia Li. Flexible high-performance SnO2/AgNWs bilayer transparent conductors for flexible transparent heater applications. *Ceramics International*, 47(14):20379–20386, jul 2021.

[186] Hahn Gil Cheong, Jin Hoon Kim, Jun Hyuk Song, Unyong Jeong, and Jin Woo Park. Highly flexible transparent thin film heaters based on silver nanowires and aluminum zinc oxides. *Thin Solid Films*, 589:633–641, aug 2015.